UNIVERSITY OF CALIFORNIA SAN DIEGO

Leveraging Latent Models of Neural Population Dynamics for Efficient and Accurate Brain State Estimation

A Dissertation submitted in partial satisfaction of the requirements
for the degree Doctor of Philosophy

in

Electrical Engineering (Medical Devices & Systems)

by

Abdullah Alothman

Committee in charge:

Professor Vikash Gilja, Chair
Professor Nicholas Antipa
Professor Gert Cauwenberghs
Professor Duygu Kuzum
Professor Gal Mishne

2023

The Dissertation of Abdullah Alothman is approved, and it is acceptable in quality and form for publication on microfilm and electronically.

University of California San Diego

2023

DEDICATION

To Noorah, my eternal support.

TABLE OF CONTENTS

LIST OF FIGURES

LIST OF TABLES

ACKNOWLEDGEMENTS

These five years of my life have been a long journey, full of trials and tribulations. Many sleepless nights I have experienced, either because of overdue work or my fully awake daughter that we were blessed with in the middle of my PhD journey. Of course, not to mention the added challenge from the wide spread of COVID-19 that slowed things down right as my workflow picked up in my second year. I'll remember those days fondly, as the pain and anguish have already passed.

First and foremost, I would like to thank my mentor, my advisor, and my guide through this journey, Vikash Gilja. He picked me up when I visited his office for the first time in my first year of PhD with little knowledge in neuroscience and neural engineering of brain-machine interfaces. He showed me the ropes and presented me with many opportunities that turned into a significant part of my PhD thesis. Countless days we spent discussing on his office board seeds of ideas that turned into great ideas. For this I am grateful.

Secondly, I would like to thank the members of the TNEL lab members, Aashish Patel, Pablo Tostado, Sophia Huang, Lauren Stanwicks, Lo Ostrowski and Xavi Perez, with whom I shared this journey, spent days discussing ideas, venting, sharing PhD woes, and lifting each other's spirits. I would also like to thank our wonderful lab alumni who guided me when I first joined, Abdulwahab Alasfour, Daril Brown, Tejaswy Pailla and Paolo Gabriel.

Last but not least, my heartfelt appreciation to my wife Noorah, parents, and siblings, without whom this journey would have been impossible. Their continuous support and love have helped through really difficult times. My wife dropped her life and job back and came here to be with me and for that I am eternally grateful. My parents supported me from the beginning in every decision I made, especially when I was on the verge of quitting my PhD

during a time when I was stranded outside the US for half a year during prolonged and ambiguous visa processing.

Finally, I would like to thank all our collaborators and co-authors helped with datasets, feedback and fruitful discussions to make the following work a reality:

Chapter 2, in full, is a reprint of Abdullah Alothman, Chao-li Wei, Pablo M. Tostado, Eric Trautmann, Xulu Sun, Daniel J. O'Shea, Ezequiel Arneodo, Timothy Q. Gentner, Vikash Gilja**,** *"Unsupervised Channel Compression Methods in Neural Prostheses Design".*

Chapter 3, in part, a reprint of Mehrdad Ramezani, Jeong-Hoon Kim, Xin Liu, Chi Ren, Abdullah Alothman, Chawina De-Eknamkul, Madison N. Wilson, Ertugrul Cubukcu, Vikash Gilja, Takaki Komiyama, and Duygu Kuzum, *" Cellular Calcium Activity at Depth Predicted from Surface Potential Recordings using Ultra-high Density Transparent Graphene Arrays*". Nature Nanotechnology, 2023.

Chapter 4, in part is currently being prepared for submission for publication of the material. Abdullah Alothman**,** Mehrdad Ramezani, Jeong-Hoon Kim, Xin Liu, Chi Ren, Chawina De-Eknamkul, Madison N. Wilson, Ertugrul Cubukcu, Takaki Komiyama, Duygu Kuzum, and Vikash Gilja, *" Leveraging latent modeling in multimodal neural recording for accurate brain state estimation".*

VITA

2013 Bachelor of Science in Electrical Engineering, King Fahd University of Petroleum and Minerals, Dhahran, Saudi Arabia

2018 Master of Science in Electrical and Computer Engineering, University of Washington, Seattle, Washington, USA

2023 Doctor of Philosophy in Electrical Engineering (Medical Devices & Systems), University of California San Diego, USA

2023 Assistant Professor, King Fahd University of Petroleum and Minerals, Dhahran, Saudi Arabia

PUBLICATIONS

Abdullah Alothman, Chao-li Wei, Pablo M. Tostado, Eric Trautmann, Xulu Sun, Daniel J. O'Shea, Ezequiel Arneodo, Timothy Q. Gentner, Vikash Gilja, "*Unsupervised Channel Compression Methods in Neural Prostheses Design*", Nature Biomedical Engineering 2023, **Submitted.**

Mehrdad Ramezani, Jeong-Hoon Kim, Xin Liu, Chi Ren, **Abdullah Alothman**, Chawina De-Eknamkul, Madison N. Wilson, Ertugrul Cubukcu, Vikash Gilja, Takaki Komiyama, and Duygu Kuzum, " *Cellular Calcium Activity at Depth Predicted from Surface Potential Recordings using Ultra-high Density Transparent Graphene Arrays*", Nature Nanotechnology 2022. **Revised manuscript submitted.**

Abdullah Alothman, Mehrdad Ramezani, Jeong-Hoon Kim, Xin Liu, Chi Ren, Chawina De-Eknamkul, Madison N. Wilson, Ertugrul Cubukcu, Takaki Komiyama, Duygu Kuzum, and Vikash Gilja, " *Leveraging latent modeling in multimodal neural recording for accurate brain state estimation*", **In preparation.**

Pablo M. Tostado, Ezequiel M. Arneodo, Daril E. Brown II, Xavier A. Perez, Adam Kadwory, Lauren L. Stanwicks, **Abdullah Alothman**, Timothy Q. Gentner, and Vikash Gilja, "*Neural population dynamics of songbird RA and HVC during learned motor-vocal behavior",* eLife 2023. **Submitted.**

Abdullah Alothman & Vikash Gilja. Unsupervised Channel Compression Methods in Motor Prostheses Design. Annual International Conference of the IEEE Engineering in Medicine and Biology Society. IEEE Engineering in Medicine and Biology Society. Annual International Conference, 2021, 6581–6585.

Abdullah Alothman and Vikash Gilja, "*Unsupervised Channel Compression Methods in Motor Prostheses Design*," **Patent**. Provisional patent, October 2021. Full patent application filed October 2022

ABSTRACT OF THE DISSERTATION

Leveraging Latent Models of Neural Population Dynamics for Efficient and Accurate Brain State Estimation

by

Abdullah Alothman

Doctor of Philosophy in Electrical Engineering (Medical Devices & Systems)

University of California San Diego, 2023

Professor Vikash Gilja, Chair

It has been demonstrated that the neural population activity is often dominated by a few prominent latent neural modes in low-dimensional space that capture a significant fraction of the population covariance. Previous studies showed that those latent modes can be used as basic building blocks for brain-computer interfaces (BCI). In fact, it was demonstrated that through modeling those latent modes into variables, one can drive an online BCI with a performance surpassing traditional neural-observation-driven BCI. Additionally, it has been proposed that

these neural modes are stable over long periods of time with respect to the intended behavior. To that end, we propose in this thesis methods and techniques that aim to enhance the performance of these latent-variable-driven BCIs in a multitude of ways. In the first chapter, we propose an unsupervised compression technique for neural interfaces that aims to compress input neural features by minimizing the loss of information between observations and modeled latent modes. Our results suggest the potential of design neural interfaces with sublinear power scaling with number of input electrodes which could enable power-efficient large-scale neural recordings. In the second chapter, we utilize latent modeling in a multimodal study featuring Electrocorticography (ECoG) and calcium imaging to show that you can predict the activity of modality using the other. We predict the latent modes of the calcium response using spectral features of ECoG recording then project decoded modes into the observation space to reconstruct single-cell activity of calcium response. In the last chapter, we extend this work in multimodal analysis to propose a generalized framework that unifies multiple modalities. One can leverage the unique strength of each modality by projecting them into a common latent space, which can be utilized to drive a brain-computer interface more accurately.

Chapter 1

Introduction

Background

Advances in brain-machine interfaces (BMI) have allowed individuals with paralysis, due to spinal cord injuries or neurological diseases, to control assistive interfaces using commands from the brain. Notable clinical studies in BCIs have allowed subjects to control robotic arm [1,2] and a cursor [3,4,5,6], decode imagined speech [7], and predict the early onset of chronic pain state in patients [8]. All these achievements were made possible due to the technological advancement in recording methods of the brain and their associated computational analysis tools. These acquisition techniques only offer a partial view of how the brain responds to physiological or cognitive processes, also known as the brain state. Indeed, estimating brain state and understanding how the activity of population of neurons encode behavior is a basic building block in functional BMIs. Capturing the dynamics of these populations and how they evolve over time in the presence of stimuli has advanced our understanding of the brain.

Several studies, mainly in motor physiology, have demonstrated that the activity of these neural populations and their dynamics can be effectively described by set of low dimensional latent variables confined in a subspace called neural manifold [9-13]. Additionally, previous work in the motor region showed that low dimensional latent variables could encode behavioral features better compared to the dimensional neural observations. Importantly, when projections to neural manifolds are used by a BMI as input features, studies demonstrate better online motor control performance relative to BMIs that use smoothed firing rates as input features [14].

In this thesis, we argue that by modeling the latent modes of neural population activity, we can enhance our estimation of brain state during BCI experiments. We develop algorithm and frameworks in various number of studies to support that argument and postulate that with the emerging number of BCI studies that employ modeled latent variables as input features, such proof of concepts that we present here will be of importance in the future.

Thesis overview

In chapter 2, we demonstrate that by preserving the latent variables that we modeled from input features in neural interfaces, we can compress those features while controlling the impact on application specific evaluation metrics. We apply this compression method to various datasets spanning different species and behavior to demonstrate its efficacy. This chapter is a reprint of Abdullah Alothman, Chao-li Wei, Pablo M. Tostado, Eric Trautmann, Xulu Sun, Daniel J. O'Shea, Ezequiel Arneodo, Timothy Q. Gentner, Vikash Gilja**,** ″Unsupervised Channel Compression Methods in Neural Prostheses Design″.

In chapter 3, we investigate a multimodal study of surface electrophysiological recording and depth Calcium imaging and seek to study their correlation. We demonstrate that we could reconstruct single-cell activity of Calcium response at depth from spectral features of surface recording through decoding latent variables of Calcium signals. This chapter is, in part, a reprint of Mehrdad Ramezani, Jeong-Hoon Kim, Xin Liu, Chi Ren, Abdullah Alothman, Chawina De-Eknamkul, Madison N. Wilson, Ertugrul Cubukcu, Vikash Gilja, Takaki Komiyama, and Duygu Kuzum, ″ Cellular Calcium Activity at Depth Predicted from Surface Potential Recordings using Ultra-high Density Transparent Graphene Arrays″.

In chapter 4, we extended this study by trying to postulate a generalized framework to unify modalities in multimodal studies in one common subspace. By modeling the latent modes of each modality, we can combine their advantages to accurately estimate brain state. This chapter is a reprint of Abdullah Alothman**,** Mehrdad Ramezani, Jeong-Hoon Kim, Xin Liu, Chi Ren, Chawina De-Eknamkul, Madison N. Wilson, Ertugrul Cubukcu, Takaki Komiyama, Duygu Kuzum, and Vikash Gilja, ″ Leveraging latent modeling in multimodal neural recording for accurate brain state estimation″.

References

[1]Collinger JL, Wodlinger B, Downey JE, Wang W, Tyler-Kabara EC, Weber DJ, McMorland AJ, Velliste M, Boninger ML, Schwartz AB. High-performance neuroprosthetic control by an individual with tetraplegia. Lancet. 2013 Feb 16;381(9866):557-64. doi: 10.1016/S0140-6736(12)61816-9. Epub 2012 Dec 17. PMID: 23253623; PMCID: PMC3641862.

[2]Hochberg LR, Bacher D, Jarosiewicz B, Masse NY, Simeral JD, Vogel J, Haddadin S, Liu J, Cash SS, van der Smagt P, Donoghue JP. Reach and grasp by people with tetraplegia using a neurally controlled robotic arm. Nature. 2012 May 16;485(7398):372-5. doi: 10.1038/nature11076. PMID: 22596161; PMCID: PMC3640850.

[3]Jonathan C. Kao, Paul Nuyujukian, Stephen I. Ryu, Mark M. Churchland, John P. Cunningham, and Krishna V. Shenoy. Single-trial dynamics of motor cortex and their applications to brain-machine interfaces. Nature Communications, 6(1):7759, November 2015.

[4] Vikash Gilja, Chethan Pandarinath, Christine H. Blabe, Paul Nuyujukian, John D. Simeral, Anish A. Sarma, Brittany L. Sorice, J´anos A. Perge, Beata Jarosiewicz, Leigh R. Hochberg, Krishna V. Shenoy, and Jaimie M. Henderson. Clinical translation of a high-performance neural prosthesis. Nature Medicine, 21(10):1142–1145, October 2015. Number: 10 Publisher: Nature Publishing Group.

[5] Chethan Pandarinath, Paul Nuyujukian, Christine H Blabe, Brittany L Sorice, Jad Saab, Francis Willett, Leigh R Hochberg, Krishna V Shenoy, and Jaimie M Henderson. High performance communication by people with paralysis using an intracortical brain-computer interface. eLife, 6:e18554, February 2017. Publisher: eLife Sciences Publications, Ltd.

[6]Jonathan C. Kao, Stephen I. Ryu, and Krishna V. Shenoy. Leveraging neural dynamics to extend functional lifetime of brain-machine interfaces. Scientific Reports, 7(1):7395, August 2017. Number: 1 Publisher: Nature Publishing Group

[7]Willett FR, Kunz E, Fan C, Avansino D, Wilson G, Choi EY, Kamdar F, Hochberg LRH, Druckmann S, Shenoy K, Henderson J. A high-performance speech neuroprosthesis. bioRxiv [Preprint]. 2023 Apr 25:2023.01.21.524489. doi: 10.1101/2023.01.21.524489. PMID: 36711591; PMCID: PMC9882398.

[8]Shirvalkar P, Prosky J, Chin G, Ahmadipour P, Sani OG, Desai M, Schmitgen A, Dawes H, Shanechi MM, Starr PA, Chang EF. First-in-human prediction of chronic pain state using intracranial neural biomarkers. Nat Neurosci. 2023 Jun;26(6):1090-1099. doi: 10.1038/s41593-023-01338-z. Epub 2023 May 22. PMID: 37217725; PMCID: PMC10330878.

[9]Saurabh Vyas, Matthew D. Golub, David Sussillo, and Krishna V. Shenoy. Computation Through Neural Population Dynamics. Annual Review of Neuroscience, 43(1):249–275, July 2020.

[10]Juan A. Gallego, Matthew G. Perich, Stephanie N. Naufel, Christian Ethier, Sara A. Solla, and Lee E. Miller. Cortical population activity within a preserved neural manifold underlies multiple motor behaviors. Nature Communications, 9(1):4233, October 2018. Number: 1 Publisher: Nature Publishing Group.

[11]Barbara Feulner and Claudia Clopath. Neural manifold under plasticity in a goal driven learning behaviour. PLOS Computational Biology, 17(2):e1008621, February 2021. Publisher: Public Library of Science.

[12]MM Churchland, JP Cunningham, MT Kaufman, JD Foster, P Nuyujukian, SI Ryu, and KV Shenoy. Neural population dynamics during reaching. Nature, 487(7405):51–56, July 2012.

[13]Patrick T. Sadtler, Kristin M. Quick, Matthew D. Golub, Steven M. Chase, Stephen I. Ryu, Elizabeth C. Tyler-Kabara, Byron M. Yu, and Aaron P. Batista. Neural constraints on learning. Nature, 512(7515):423–426, August 2014.

[14]Jonathan C. Kao, Paul Nuyujukian, Stephen I. Ryu, Mark M. Churchland, John P. Cunningham, and Krishna V. Shenoy. Single-trial dynamics of motor cortex and their applications to brainmachine interfaces. *Nature Communications*, 6(1):7759, November 2015.

Chapter 2

Unsupervised Channel Compression Methods in Neural Prostheses Design

Abstract

Large-scale simultaneous recording of neural populations can enable the development of high-performance brain-machine interfaces (BMIs). Unfortunately, proposed implantable neural interfaces have power requirements that scale linearly with electrode count. To facilitate the design of interfaces with reduced power requirements, we propose and evaluate a compressed sensing strategy that is based on unsupervised learning. This strategy suggests novel neural interface architectures which compress neural data by methodically combining neural features extracted from recording electrodes. We develop an entropy-based compression strategy that models the population of neurons as being generated from a lower dimensional set of latent variables and aims to minimize the loss of information in the latent variables due to compression. By minimizing this loss, we preserve the modeled trajectories of behavior in the latent variable space. To evaluate compressed features, we inferred the latent variables from these features and measured the accuracy through estimating activity of held-out features and decoding behavioral variables. As many studies in recent years of large-scale neural recording rely on latent variable modeling, whether it is for exploring population dynamics or driving BMIs, we postulate that this proof of concept will become relevant for efficient brain state estimation through accurate inference of latent variable trajectories.

Introduction

Advances in neural recording systems and associated computational methods have enabled the development of brain-machine interfaces (BMI) with the potential to restore lost function in individuals with impairments, such as loss of speech or motor control, due to spinal cord injuries or neurological diseases. Proof of concept BMI studies have demonstrated that these systems can synthesize aspects of speech from a given corpus [1, 2], control a prosthetic arm for reaching and grasping [3, 4, 5], type full sentences on a computer [6, 7, 8], and control a computer mouse like cursor [9, 10, 11, 12]. One aspect of BMI design that continues to advance is the scale with which neural interfaces record neuronal ensembles, particularly at singular neuron resolution [13, 14, 15, 16, 17]. Recording and monitoring larger ensembles of neurons allows for improved modeling of the relationship between neural activity and behavior and, consequently, more accurate inference of intended behavior from neural activity. Several studies have suggested a loglinear relationship between BMI performance and electrode count, as illustrated in Figure 2.1a. [4, 11, 7]. Thus, advances in neuroscience and neural engineering are often driven by an increase in the number of simultaneously recorded electrodes, motivating the development of neural interfaces with increased electrode count. Two recent examples of large-scale recording systems are the Neuropixels 2.0 [18] and the Argo [19]. Neuropixels 2.0, with its implantable two 4-shank probes, has 10,240 electrodes and can record from 784 of its electrodes simultaneously. The Argo, designed with 65,536 simultaneously recorded electrodes, has been applied to record spiking activity from 791 neurons and cortical surface LFP activity from over 30,000 channels. As these systems illustrate, advances in device fabrication techniques enable the development of devices with 1000s of electrodes. However, recording from all electrodes simultaneously also requires scaling the circuits that measure neurophysiology. Recording and sampling relevant regions of the

brain to detect action potentials (spiking) and local field potentials (LFPs) is power intensive, as it requires filtering, amplification, digitization and telemetry. This requirement introduces a power and heat bottleneck in current neural recording systems due to the challenges of power delivery and negative impact of heating on brain tissue [20]. The Argo system is not implantable, due to the volume and weight of the supporting electronics and heat dissipation elements that enable recording from 65,535 electrodes simultaneously. The Neuropixels, in contrast, limits the number of electrodes that can be recorded, and therefore facilitates clinical implantation.

In an effort to develop high-density neural interfaces that are more power efficient, prior design studies have focused on reducing the power required to record each individual electrode site. Nason et al. demonstrated that BMIs that infer motor behavior from spectral features of spike band power (SBP) can achieve similar online motor control performance to BMIs that infer behavior from traditional threshold crossing based spike event features. In an experiment of multi-finger flexion and extension, they achieved successful BMI control using SBP features that integrate spectral power between 300-1000 Hz. By using SBP features as input, power consumption per electrode can be reduced by multiple orders of magnitude [21]. In another study, Even-chen et al. showed that power requirements can be reduced by relaxing the design requirements typically applied to neural interface architectures. Their proposed neural interface architecture permitted errors in neural spike detection and were designed with lower signal to noise ratio requirements. They studied the effect of spike error rates on online BMI performance and evaluated the impact on motor decoding performance. They concluded that the rate at which a neural interface introduces spike errors could be increased substantially with negligible impact on BMI decoding performance. The resulting relaxation of signal to noise requirement allows for parameters of current neural interface architectures to be modified and, consequently, for power

requirements to be reduced. The designs suggested by these studies reduce the power required per electrode and, therefore, facilitate the development of BMI systems with higher electrode count. Although these strategies enable higher electrode counts, power requirements will still scale linearly with electrode count. As such a new system design bottleneck will exist but at a higher number of recorded electrodes [22].

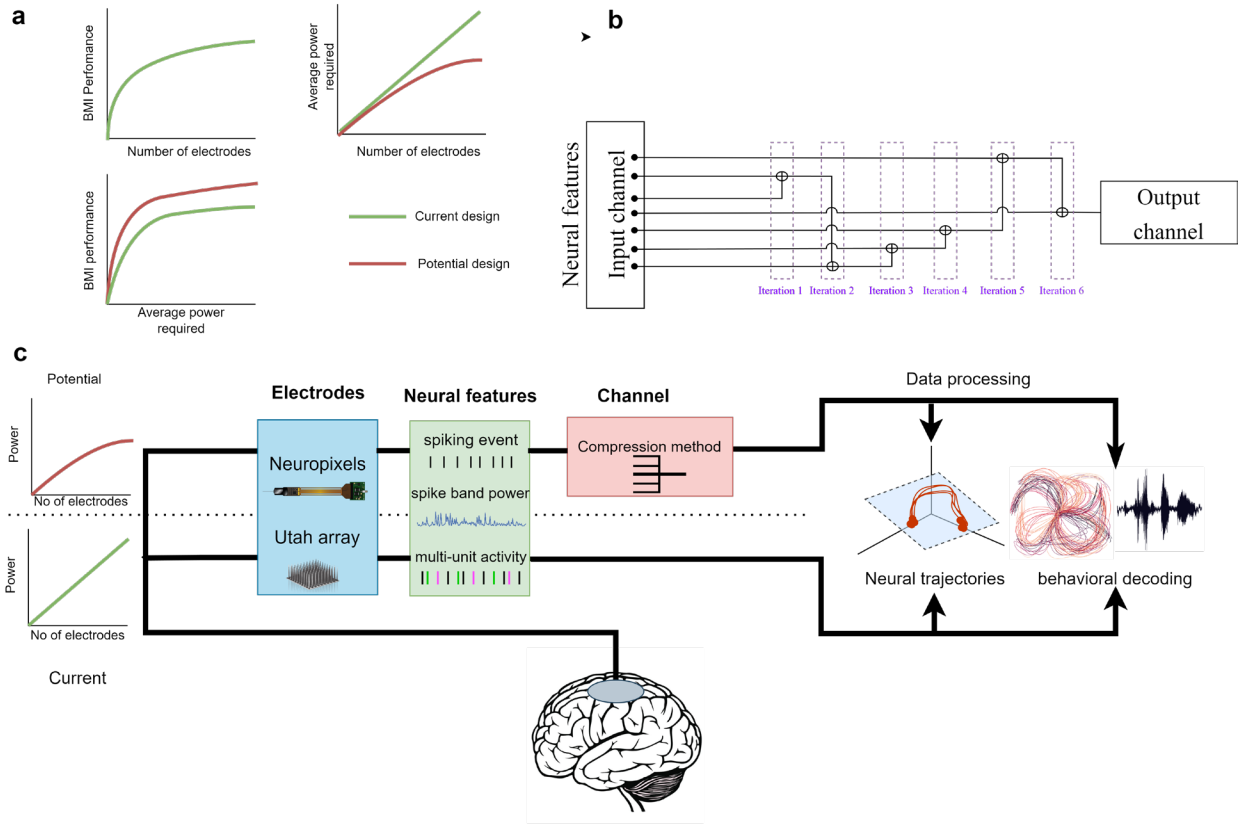

Figure 2.1 **A brief summary of the compression algorithm and its advantages.**

a) shows the relationship between average power required, BMI performance, and number of channels in conventional and potential BMI design when applying the proposed compression method. b) shows how the proposed compression method is performed on neural features. c) shows the potential vs. conventional architecture in BMI.

In addition to improving BMI performance and advancing prosthetic design, increases in the number of simultaneously recorded electrodes have implications for basic neurophysiology studies. Simultaneous measurement enables single trial inference of neural state and its dynamics from populations of neurons and more detailed interrogation of how the activity of these populations relate to stimuli, behavior, and other neural populations. A common strategy for inferring neural state, particularly in motor physiology studies, is to assume that neural state can be described by a set of latent variables confined to a low dimensional space that effectively describes the activity of the higher dimensional population of neurons. This lower dimensional space is often described as neural manifold in the neural measurement space that can capture patterns of variation that are shared across the dimensions of neural measurement (i.e., shared variation across neurons). A potential theoretical motivation for the existence of such a manifold is the high degree of recurrent connectivity amongst neurons within a spatially constrain cortical region, which could lead to a high degree of co-modulation across those neurons [23, 24, 25, 26, 27, 28, 29, 30, 31]. Previous studies employing a range of algorithmic techniques have demonstrated a high degree of correlation between structured behavior over time and the trajectory of neural state defined by projection onto this neural manifold [17, 32, 33, 34, 35, 36, 37, 38]. Previous studies in the motor region demonstrate that low dimensional latent variables can capture neural variability effectively and relate better to behavioral features compared to the dimensional neural observations. Importantly, when projections to neural manifolds are used by a BMI as input features, studies demonstrate better online motor control performance relative to BMIs that use smoothed firing rates as input features [8, 39]. It has been proposed that neural manifolds are stable over periods of days and weeks with respect to intended behavior. Specifically, changes in recorded neurons, due to instability in multi-day recording, give different empirical estimates of

the neural manifolds, and those estimates can be aligned in one subspace [40, 41]. Previous work has shown that the geometry of a low-dimensional manifold can be estimated from a small set of random mixtures of higher dimensional features [42]. Trautmann et al. connected this theory of random projections to unsorted multi-units. As such, they were able to accurately estimate neural population dynamics, as described by low dimensional latent variables, using unsorted multi-units and simulated multi-units, where they randomly mixed single units [43]. Additionally, multiple studies have shown that in prosthetic BMIs, performance difference between spike-sorted features and unsorted features (multi-unit activity, MUA) is often small [44, 45]. This provides motivation for us to study whether informed mixtures of neural features, based on designed compression methods, can yield high accuracy estimates of low dimensional manifold with even lower numbers of input channels. We posit that through an informed mixing of higher dimensional neural observations, we require a smaller set of those mixtures to estimate the low-dimensional manifold when compared to random mixtures.

In the studies proposed by Even-chin et al. and Nason et al., the neural features from each electrode were relaxed to lower power requirement. In this study, we present and evaluate a complimentary strategy to relax the requirement of processing all of the recorded electrodes. Neural features from recorded electrodes are inputted into the channels of our developed compression method 1c. Features in those channels can be combined or dropped in a principled and unsupervised manner to reduce the number of output channels with controlled reduction, based on desired compression ratio, in application specific BMI performance as a tradeoff. This is predicated by the theory that low-dimensional manifold, and trajectories within, can be estimated using a mixture of higher dimensional observations. Such a strategy suggests opportunities for the redesign of invasive neural interfaces which could enable higher neural feature electrode count

recording with potential power savings through sub-linear scaling of power requirements. We develop and apply methods to single-unit spike count features, which form a set of initial sensing channels, then extend it to other neural features such as SBP and unsorted multi-unit. Specifically, the goal is to apply unsupervised-learning based channel compression methods to combine these channels while minimizing loss of information. By simply adding neural features to simulate combined channels (Figure 2.1), we reduce the channel count while maintaining good scoring on multiple evaluation metrics that estimate information in the original and compressed channels. This would allow neural features to be compressed to a fewer number of channels, enabling the design of neural prostheses that utilize such compression to potentially reduce power requirements, without compromising the application specific performance requirements. To quantify the loss of information due to compression, we introduce two evaluation metrics to assess the latent variables inferred from compressed features. The first metric measures how well the latent variables can represent the original neural features by predicting the activity of a neuron left out during the variables' inference. The second metric evaluates how accurately the latent variables can explain and relate to behavioral features.

Methods

The core idea of this technique is to methodically compress neural features while maintaining the estimated single-trial neural trajectories in the low-dimensional latent space. Using neural features as input to the compression algorithm, we utilize a generative model to estimate latent trajectories and model parameters. To methodically compress neural input features, we impose a compression criterion on the features and model parameters to determine the features that satisfy this criterion the most. Latents are extracted from the compressed features and using a set of evaluation metrics relevant to BMI performance; we estimate the loss of relevant information due to compression. The Methods Section will discuss each component of the compression algorithm in full detail.

Channel-wise compression by combination

Compression of input neural feature channels is achieved by summing these features from multiple channels. We define the uncompressed neural features by Y such that N is the number of initially sorted neurons and T is the number of timepoints within the dataset. We also define Y_M as the compressed feature set, with D representing the number of channels after compression. Therefore, we define the M matrix such that:

$$Y_M = MY$$

The M matrix formulation is the primary goal of this work. The compression mapping matrix M compresses the original dataset by combining input features and is formulated by different strategies. The goal is to develop strategies that maintain information about the

observations in the original population in Y while reducing the input feature dimensionality (Figure 2.1b). We impose several constraints on the design of the M matrix:

- The M matrix is applied to combine spike counts in channels; thus M must be binary.
- Channels from the N neurons in Y can be mapped to only one of the D channels in Y_M.
- All channels must be mapped to an output channel. No channels are dropped in the compression; thus, the column sum of the M matrix has to be 1. Note: we consider dropping channels later in the Discussion.

Greedy dimensionality reduction

Solving for M as a binary matrix is NP-hard problem and requires complex solving computational capabilities. As such, with an initial examination of compression strategies, we consider taking a greedy approach in which channel count is iteratively reduced. Channels are initialized as single channels of neural features, and at each iteration, one pair of channels is combined to reduce the channel count by 1. The pair is selected by evaluating a metric defined by a designed compression method. Channels are combined iteratively until a desired number of channels remain (Figure 2.1b).

Latent neural trajectory estimation

Trajectories are estimated by applying Gaussian Process Factor Analysis (GPFA). GPFA is a generative probabilistic model developed by Yu et al. [4] for application to neural spiking data that unifies learning temporal smoothing and dimensionality reduction parameters to extract latent variable trajectories that describe shared variability in the original high-dimensional data. The latent variables in GPFA are defined here as $Z \in R^{(Q\ x\ T)}$, where $Q < N$. Q is determined based

on the given behavior and species as followed historically. Therefore, the relationship between the observations and the latent variable at time $t \in T$ is given by:

$$y_{:}^{t} | z_{:}^{t} \sim N(Cz_{:}^{t} + \mu, R)$$

where represents all the latent variables at timepoint t, $C \in \Re^{N \times Q}$ is the factor loading matrix, $d \in \Re^{N \times 1}$ is the mean of the neural observations, and $R \in \Re^{N \times N}$ is the covariance. Each latent variables are correlated with itself across time through a Gaussian process (GP):

$$z_{i}^{:} \sim N(0, K_i)$$

where $K_i \in \Re^{T \times T}$ is the covariance matrix of the ith Gaussian process. The smoothing properties are determined by the choice of the form of the GP covariance. The form of K chosen is a squared exponential covariance function. The neural states can be inferred by:

$$E[\bar{z} | \bar{y}] = \bar{K}\bar{C}'\left(\bar{C}\bar{K}\bar{C}' + \bar{R}\right)^{-1} * \left(\bar{y} - \bar{d}\right)$$

In this equation, $\bar{y}$ and $\bar{z}$ are concatenations of features of neural observations and neural states, respectively, across all timepoints T. $\bar{C}$ and $\bar{R}$ are T blocks of C and R, and $\bar{K}$ is composed of Q sub-matrices where each sub-matrix along the diagonal is the covariance between two timepoints in the neural state $i, \bar{K}_{i,(t_m,t_n)}$ (more details in [33]). Using GPFA, we infer the low dimensional trajectory (i.e., the latent variables across time) based upon Y and the compressed Y_M. Because GPFA is a probabilistic framework with latent variables, the Expectation Maximization (EM) algorithm is employed for parameter estimation. The parameters are not guaranteed to converge to the same deterministic values each time. Therefore, if the model is learned separately for each compressed feature set, there is no guarantee that the set of learned models will map to

the same latent space Z. To avoid this problem and to facilitate direct comparison of models, GPFA parameters are learned once from the original uncompressed dataset Y, and the compression matrix M is applied to the learned parameters to find the parameters of the reduced dataset Y_M:

$$y = Cz + d + \epsilon \rightarrow y_M = My = MCz + Md + M\epsilon$$

Therefore, the parameters of the GPFA model of the reduced dataset are given by: $C_M = MC$ and $d_M = Md$. The covariance $R_M = cov(M\epsilon) = MRM'$. The M matrix compresses neural observations only, while the latent space is unchanged, thus the compression does not change K. We employ 4-fold cross-validation to the dataset and train four separate GPFA models (supp Figure 2.7). The parameters for each model are used in the compression methods, described below, to learn 4 different sets of M matrices.

Compression criterion

Finally, we discuss the compression methods used to combine channels. These methods vary between operating on the neural observations alone or both the latent variables and observations. In the current work, our compression is based on the relationship between the neural population and the latent variables without considering correlations across time. The current method focuses more on latent trajectory estimation to establish a basis for compression applications. Future opportunities for modeling temporal correlation in compression might exist by incorporating GPs. The joint distribution between the observations and the latent states is given in equation:

$$\begin{bmatrix} y \\ z \end{bmatrix} \sim N\left(\begin{bmatrix} d \\ 0 \end{bmatrix}, \begin{bmatrix} 1 & C' \\ C & CC' + R \end{bmatrix}\right)$$

Conditional entropy

Entropy is the measurement of uncertainty in a random variable. We utilize conditional entropy to evaluate how much of the latent variable entropy is affected by the choice of compression for the observation channels. That is, we measure the conditional entropy, given in equation 7, of the latent variable given the current channel set. In each greedy iteration, we evaluate which combination of channels has the lowest conditional entropy.

$$H(Z \mid Y) = H(Z, Y) - H(Y)$$

We know that by combining channels, we lose mutual information, and thus the conditional entropy is expected to increase monotonically. At each iteration, we select the channel pair that minimizes this increase in entropy. This criterion allows us to reduce the channel count at each iteration while minimizing loss in mutual information as defined by the GPFA model.

Evaluation Metrics

After extracting the trajectories of the latent variables for the compressed dataset $E[z \mid y_M]$ and the original dataset $E[z \mid y]$, we assess the impact of compression by evaluating two performance metrics as a function of the number of compressed channels. The metrics evaluate how well the latent variables can represent the high dimensional neural features (original channels) and the behavioral features (supp Figure 2.9).

Leave-out neuron goodness-of-fit (prediction error): This evaluation metric is adapted from Yu et al. [33]. This metric evaluates how much the low dimensional latent variables represent and predict the neural observations. Being able to reconstruct original observations as accurately

as possible after compression is important for exploratory work in neuroscience. The metric estimates the activity of neuron j from the latent variables inferred from all other neurons in the testing set. That is, neuron j is dropped, then the remaining neurons are used to infer the latent variables, which are then used to predict the activity of neuron j. Both inference and prediction of the test set are performed with the model parameters learned from the training set. The prediction error is computed by measuring the sum of the squared error between the original neuron and its prediction (supp Figure 2.10). We expect this error metric to increase monotonically as we iteratively reduce the number of channels. If $\hat{y}_i$ is the predicted neural activity of channel i, then prediction error is given by:

$$\sum_{i=1}^{N} ||\hat{y}_i - y_i||^2$$

Behavioral estimation error: Behavioral estimation is a vital evaluation metric for neural prostheses design. We seek to evaluate how well the low-dimensional population encodes the behavior. The behavior in this work ranges from arm reaching tasks in various experimental setups to songbirds engaging in free vocal behavior. We use the trajectories of the latent variables inferred from either the original or compressed channels to build a model to reconstruct the behavioral information in all datasets. For reaching tasks in motor control, we evaluate behavioral estimation error by building a neural dynamical filter (NDF) using extracted latents to reconstruct the hand kinematics [8]. The error, in this case, is the root mean squared error between true and reconstructed kinematics.

$$x_t = L_z z_t + b$$

Where x_t is the kinematics at time t, L_z is the term that minimizes the mean squared error for $\| X - L_z[Z;1] \|^2$ where b is the baseline. For vocal behavior in songbirds, we apply PCA to the spectrogram of the vocal behavior then build a linear regression model between the extracted latents and the spectrogram PCAs. We evaluate how well the latents can predict the spectrograms of held-out motifs.

Method Workflow

Given the neural features Y as an input to the compression algorithm, multiple steps are taken to compress and evaluate. M_k is the compression mapping matrix that reduces channel count by k.

Step 1: Extract latents and GPFA parameters (supp Figure 2.7):

- Neural features are inputted into GPFA to train the model through expectation maximization algorithm.
- GPFA parameters are extracted from the model C, R, d, K.

Step 2: Training compression model (supp Figure 2.8):

- Using model parameters, we train a compression algorithm by measuring conditional entropy of combined channels.
- Pair of channels with the lowest conditional entropy are selected and the compression mapping M_1.
- The compression mapping matrix is fed into the compression training model to compute M_2.
- This is done iteratively until a stopping criterion is met.

Step 3: Inferring latent trajectories (supp Figure 2.9):

- Given the testing neural features and the compression mapping matrices M_i where $i = 1,2,3,4,5,..N-D$, we infer two sets of latent trajectories.
- We use two sets to assess the set of evaluation metrics.
- We compare metrics values from compressed latents to uncompressed ones.
- This is done iteratively for all generated M matrices.

Dataset

The feature compression methods described were empirically evaluated using four primary datasets that span different species, behaviors and recording interfaces. The goal is to assess how well the developed compression method generalizes with different datasets. A summary of all datasets in (Table 1) with visualization in Figure 2.2. In all datasets, trials were split 80% for training the model utilized in this study and 20% for testing and measuring the evaluation metrics.

Table 1 summary of all the datasets used to test the compression algorithm.

Datasets	Device	Behavior	Region	Channel count	Animal	Keyword
D1	Neuropixels probe	Reaching	M1	263	Macaque	Radial
D2	Utah array	Reaching	Pmd/M1	93⁄67	Macaque	Pseudo
D3	Utah array	Reaching	Pmd/M1	182	Macaque	Maze
D4	Neuropixels probe	Vocal	RA	102	Zebra finch	Birdsong

Dataset 1

This dataset was collected in a rhesus macaque monkey doing a center-out reaching task. The experiment had 24 different reaching targets distributed evenly. Neural activity was recorded on a Neuropixels probe implanted in the brain's primary motor cortex (M1) region. During this task, the monkey is performing a center-out reaching task with variable delay from the target onset to the go cue. The task is deemed successful when the monkey reaches the target and holds 300 ms.

Dataset 2

This is a publicly available "pmd-1" dataset from the Collaborative Research in Computational Neuroscience [46, 47]. This dataset includes extracellular recordings from two Utah Multi-electrode Arrays (MEAs) implanted in the dorsal premotor cortex (PMd) and primary motor cortex (M1) of a monkey engaged in an upper limb reaching task. During the task, the monkey controlled a cursor on screen to acquire sequentially appearing targets. Targets appeared at random locations within a 5.15 cm radius of the previous target. The workspace was 20 cm x 20 cm with 2 cm square targets. There are 496 sequential reach trials in the dataset, and from the MEAs, 93 neurons from PMd and 67 from M1 were manually sorted.

Dataset 3

This dataset is collected in a rhesus macaque monkey performing a delayed-reaching task in a maze setup [48, 49]. In this virtual maze, the monkey was instructed to reach a color target in different maze designs that involved reaches of various complexities. Type 0 trials mean no maze setup and the reaches were straight lines. Type 1 trials mean a maze design involves a more

complex reach with curves to reach the target. This dataset had 697 type 0 trials and 716 type 1 trials, and each type involved 36 different target positions.

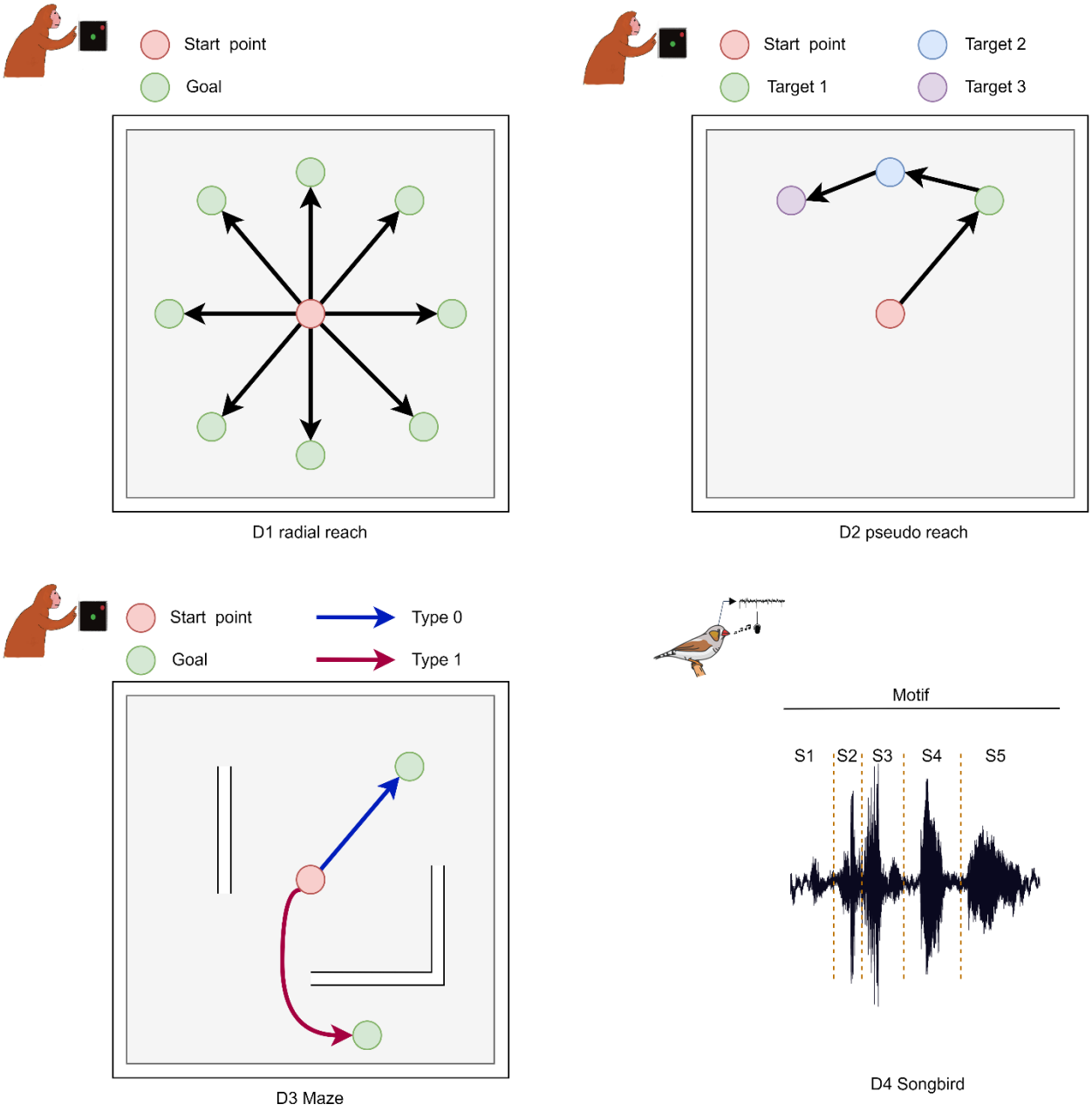

Figure 2.2 **Datasets used in testing the compression algorithm.**

D1 is a center-out reaching task with 24 conditions. D2 is a pseudo structured reaching task with no defined conditions. The targets appear sequentially after another at various angles and reach lengths. D3 is a reaching task in a virtual maze environment. Reaches consisted of two types, straight reaches (type 0) and curved reaches (type 1). D4 is a recorded vocal behavior in a freely singing zebra finch. Ten motifs were recorded, and each motif consists of 60 ms syllables.

Dataset 4

This dataset was collected in the robust nucleus of the archistriatum (RA) of a free singing zebra finch. During this vocal behavior, the zebra finch sings a stereotyped rendition of structured motifs, which are collections of ~60 ms syllables. In this dataset, we have a collection of 10 motifs; each motif consists of 4-6 main syllables and some intramotif syllables. Neural data was collected using a Neuropixel with 102 sorted single units observed in the RA region. More single units were observed in other regions of the zebra finch brain but were not considered in this study.

Results

Based on the complexity of the task, we chose the latent dimension $Q = 20$ as previous studies with similar recordings suggest that it is sufficient to capture sufficient neural variance from the population in the upper limb reaching [33, 8], and $Q = 8$ for the vocal behavior. The primary goal during compression is to show that we can compress neural input features while maintaining the structure of the latent trajectories. Additionally, because Trautmann et al. [43] showed that latent trajectories could be accurately estimated from random mixtures of single units, we aim to show that our method can estimate the trajectories with similar accuracy but at a higher compression rate, i.e., using fewer channels, assessed by the set of evaluation metrics proposed in methods (a sample of inferred trajectories in supp Figure 2.11). We simulated a random projections approach as a control. This control analysis generated 100 randomized M matrices at all compression rates for all datasets. These randomized M matrices are assessed through all of the trained models in the 4-fold cross-validation. Lastly, we introduce a metric called compression factor to evaluate compression rate. A compression factor 0 means that the data is uncompressed, i.e., the original input neural features. The compression factor increases with compression and

approaches the value 1, but it does not reach because there will always be one channel left after compression.

$$Compression\ factor = 1 - \frac{compressed\ dimension}{unccompressed\ dimension}$$

In addition to demonstrating how well our compression method compares to random projection-based compression, we report several findings that were based on the type of behavior and species.

Compression method and prediction error

Figure 2.3(a,b,c,d) shows the prediction error for all datasets. The plots show conditional entropy as the average of the cross-validation folds, while the random plot is the average per reduced dimension across all random M matrices. The plots compare the two methods across the range of compression ratios. For example, at compression factor = 0.4, we compress 40% of the neural features twice, randomly, and informatively using our compression method. Then we extract the single-trial latent trajectories from both compressed datasets. Finally, we evaluate the efficacy of compression by projecting the extracted latents into the uncompressed observation space and predicting the activity of the original features, evaluating prediction error for both methods. The plots suggest that the conditional-entropy-based method outperforms random compression ($P > 0.00001$ for all datasets, paired P-test). The dotted line marks the 1% increase in prediction error in all datasets we selected as our tolerable tradeoff in performance. At this level, our method achieves $3.7, 2.2, 1.96$, and 2.36 more compression than random combinations in $D1, D2, D3$, and $D4$ respectively.

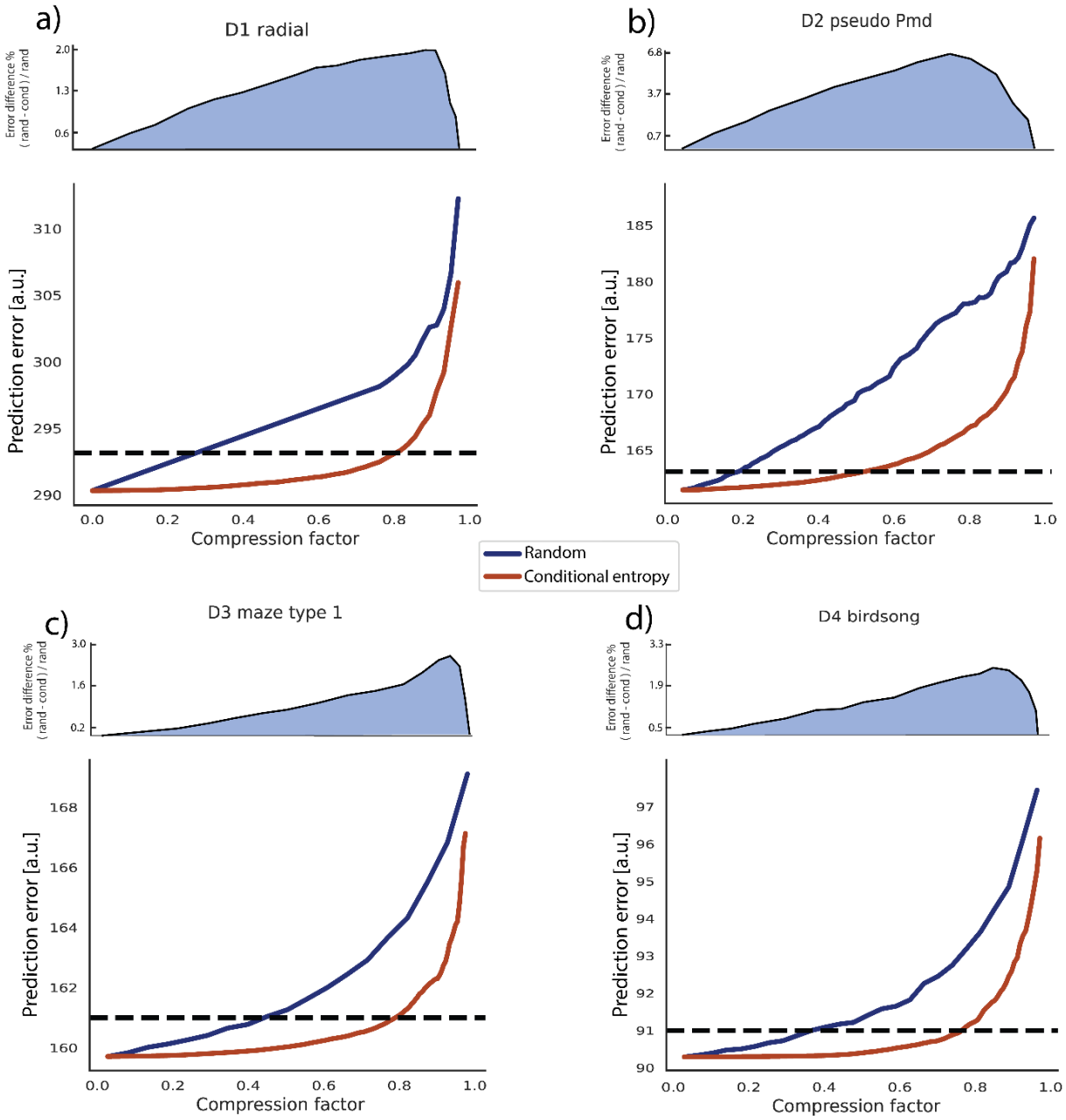

Figure 2.3 **Error in predicting activity of left-out neuron vs compression factor.**

shows the prediction error during compression normalized to the prediction error of the uncompressed original observations. All datasets show that our compression method has better performance (less error) than randomly compressing input channels ($P > 0.00001$, paired t-test). The dotted line shows the 1% increase in relative prediction error.

Compression method in motor reach behavior

Figure 2.4c shows the kinematic reconstruction error in type 1 reaching trials of the maze dataset. Since the trials are conditioned based on the target position, we opted to hold out certain conditions when training GPFA and the compression model to test how well the method generalizes over unobserved conditions. The subfigure shows that the kinematic reconstruction error behaves similarly in held-in and held-out conditions across all compression factors, and both perform better than random projection-based compression (a sample of reconstruction comparsion in Figure 2.12). To further evaluate the efficacy of compression, we compare its performance to that of more traditional feature-dropping approaches (Figure 2.4a). We apply the novel conditional entropy approach to iteratively drop the least informative neurons (retaining the subset of neurons with the lowest conditional entropy at each iteration without forming multiunit channels). This approach aims to retain the most informative single unit features at each iteration and compare it randomly dropping channels without any prior information. In Figure 2.4b, we compare this unsupervised channel combination approach to a channel-dropping approach that utilizes a supervised regression model; by applying a regression model between the hand position and the neural observations, we drop the least significant neural features (based upon p-values from the regression model). This approach resembles supervised feature selection methods often employed for BMI applications.

Compression method in vocal behavior

Similar to kinematics reconstruction error, we evaluate how well the extracted latents from compressed neural features can relate to vocal behavior in Figure 2.5. We calculated the spectrogram for each motif to extract behavioral variables from the recorded vocal output.

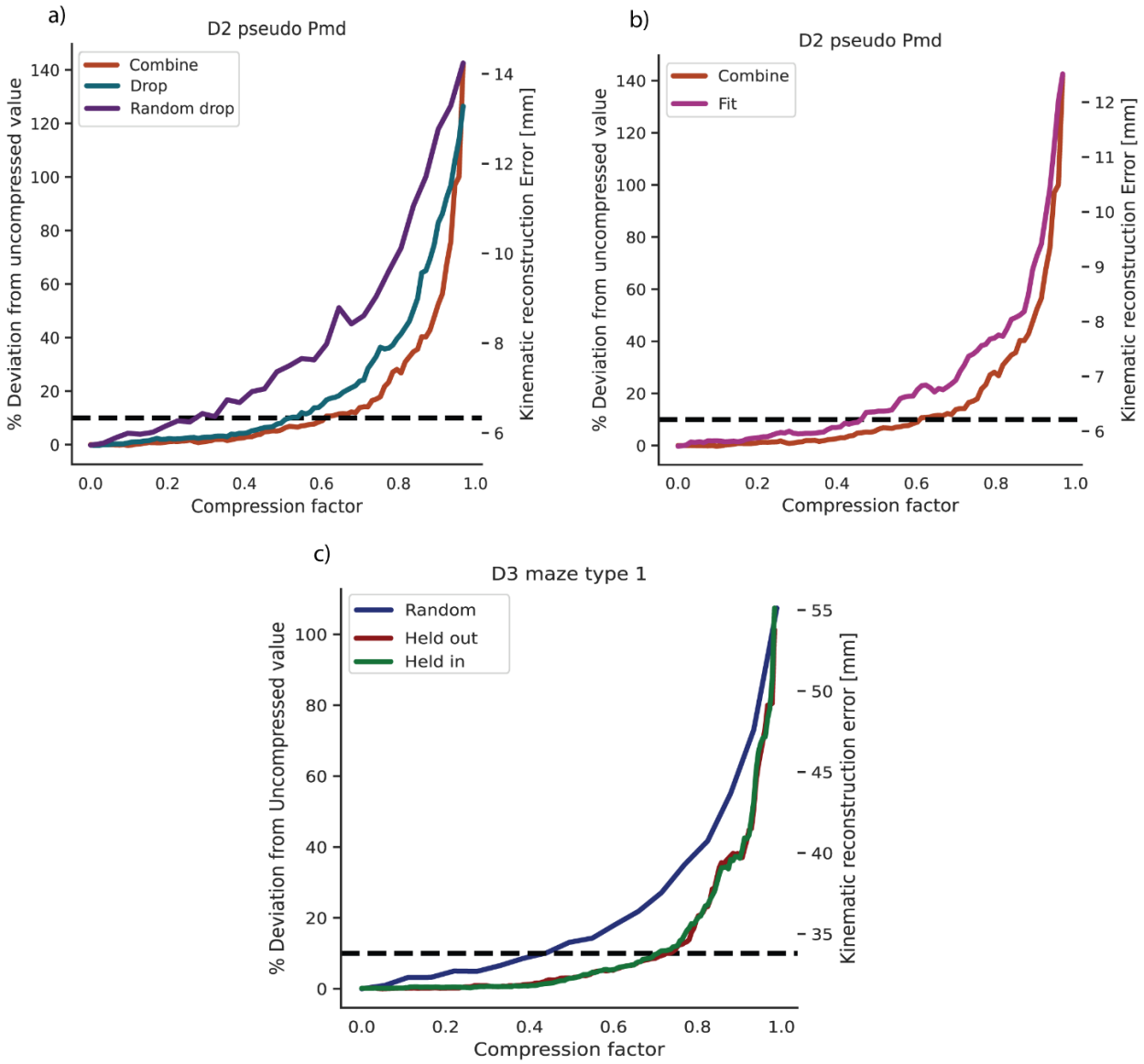

Figure 2.4 **Compression algorithm in motor control of arm reaching.**

Figure shows the kinematic reconstruction error (behavior evaluation) for the D2 and D3. Similar to prediction error, our compression method shows better behavioral evaluation than random compression of data. a) compares compression through combination "combine" and dropping "drop" using our unsupervised method. It also compares both to dropping channels randomly. b) compares compression through combination using our supervised method to supervised channel dropping. Channels were ranked based on their importance in kinematic reconstruction and removed starting from the least informative channel. c) shows the results of compression when tested on held-out conditions.

Then we projected the frequency bands of the spectrogram into a lower-dimensional space using Principal Component Analysis (PCA). The behavioral evaluation in this context is to reconstruct the PCA scores of the audio spectrogram. Additionally, we apply our compression method to other neural features than sorted single units like spike band power features [21] and unsorted multiunits. Both these new neural features were applied to songbird data.

Spatially constrained compression

Previously, we applied the compression method solely by combining pairs of channels that satisfy the compression criterion the most. However, this could lead to channels at different probe regions being assigned together for compression. Since this may not be physically realizable (or it can be possible, but it will create difficulty in the physical implementation of compression mapping), we retrain our compression algorithm with spatial constraints in Figure 2.6. This constraint restricts the pair of neurons that can be combined to the same predetermined region along the probe design to simulate a physically realizable compression strategy.

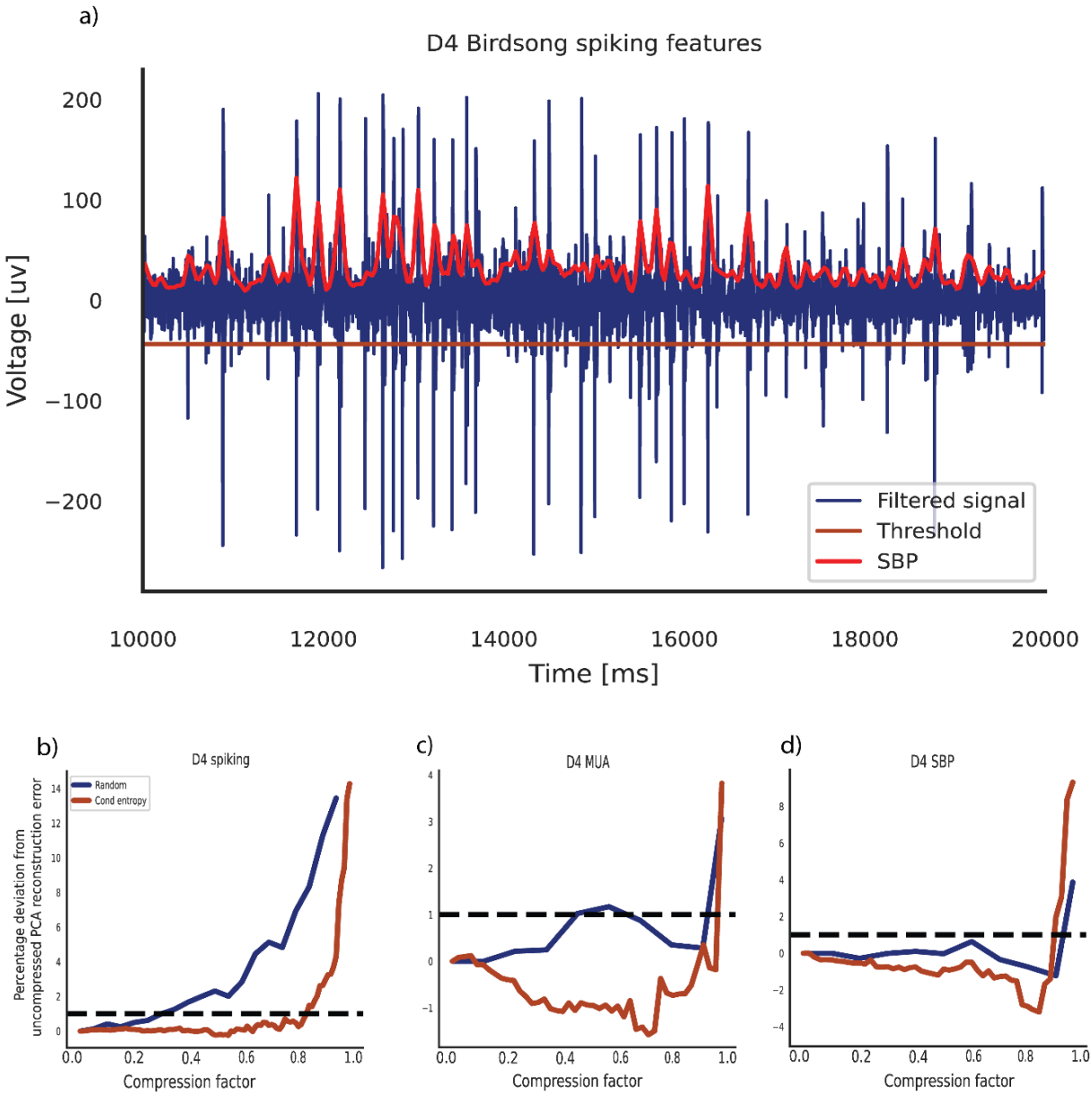

Figure 2.5 **Compression algorithm in vocal behavior and various spiking features.**

This figure shows the different spiking features we used in evaluating our compression method and how they relate to each other. Spiking band power (SBP) is the envelope of the spiking signal at 300-1000 Hz. Multiunits (MUA) are threshold crossing at -4 standard deviation for each channel. b,c,d is the reconstruction of the PCAs of the spectrogram of the birdsong motifs using different spiking features. The y-axis shows the deviation of that reconstruction error relative to the reconstruction error of the uncompressed original observation.

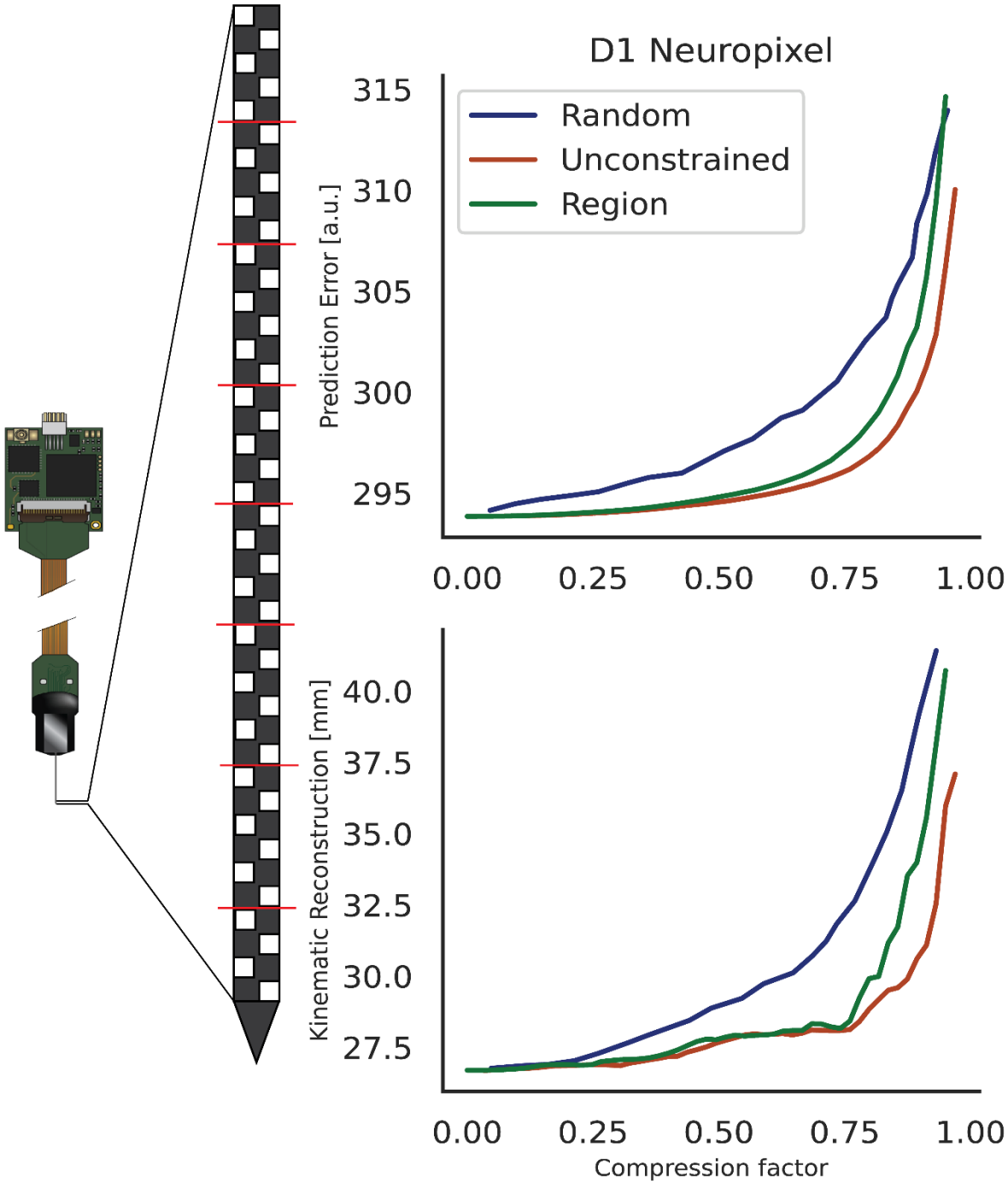

Figure 2.6 **Spatially constrained compression loses some performance for the convenience of physical design.**

This figure shows how the evaluation metrics in spatially constrained compression compare to unconstrained compression. The similarity in results suggests that spatial constraints may be a viable strategy in compression algorithm training.

Discussion

This work describes a strategy for compressing the number of recorded neural features based on summing groups of single input channels and combining them. By applying this strategy to neurophysiological data, we demonstrate that output channel count can be reduced with an unsupervised approach by choosing channel combinations that minimize the loss of information in an inferred low-dimensional latent variable space. By relaxing the requirement to transmit neural feature counts, our strategy suggests neural interface system designs with the potential to achieve sub-linear power scaling with respect to recording channel count. Such power-efficiency gains can enable the development of clinically viable, fully implantable neural interfaces with increased application-specific performance, such as more accurate and robust functional motor restoration [4].

We used an entropy-based unsupervised strategy to compress the data and evaluate how well the latent variables can be inferred after compression. These inferred variables are assessed through evaluation metrics that measure their ability to 1) represent the original neural observations and 2) encode behavioral features. Overall, the conditional entropy method optimizes compression using an iterative greedy approach and achieves good results compared to a random projections-based approach.

In order to thoroughly evaluate our developed method, we assessed the compression algorithm using two main evaluation metrics highly relevant to high-performance BMIs across several datasets spanning multiple species, prediction error of left-out neurons, and reconstruction of behavioral information. Figure 2.3 shows that our method achieves the same prediction error at compression factor magnitudes more significantly than the random projection-based compression in all four datasets. We conclude that through this compression method, we can retain more information in the latent variable about the observation space than through random compression.

Furthermore, we assess how well this method compares against traditional dropping of channels; we compare it to supervised dropping (Figure 2.4b) and unsupervised dropping (Figure 2.4a) using our compression criterion. Surprisingly, with respect to kinematic reconstruction error, the unsupervised method yields similar performance to the supervised method. Critically, unlike the supervised approach, the unsupervised approach operates without any knowledge of the behavioral features. Finally, in Figure 2.4c, we show that our method generalizes over held-out and held-out conditions used to train the compression model. In Figure 2.5, we further test the generalization of this compression method by extending it to a new species and behavior and testing two new neural features, SBP and MUA. We observe similar results in this analysis to previous ones where our method performs better than random projection. In Figure 2.5 {c,d}, the behavioral reconstruction error decreases as we compress the input channels. We speculate that this results from overfitting at the uncompressed level due to the limited number of trials. Therefore, when reducing the dimensionality of the inserted observation space, we reduce the effect of overfitting. Finally, in Figure 2.6, we spatially constrain the pair of input channels you can combine to simulate physical limitations in actual implementation. The result shows that even with the spatial constraints, the evaluation metrics have similar results to the unconstrained evaluation metrics, which could suggest that spatially constraining is a viable strategy to improve physical implementation while not suffering in relative metrics.

Physical implementation

To design this compression method in a physical implementation, two core parts of the model training to be fully realized: extraction of neural features and conditional entropy iterative

calculations to choose the best channel pair to compress. In order to achieve that, two methods are proposed:

- Neural input features or feature statistics can be transferred as subsets outside computing systems where compression parameters can be calculated.
- Neural input features can be stored on the readout system, sent in small steps to maintain limited bandwidth, and stored again on the computing system to train the compression algorithm. Once the compression mapping is derived, it is transferred back to the readout unit for implementation. Since this mapping is realizable in the digital domain, basic physical mapping design can consist of multiplexers and adders.

Moving to the analog domain

Studies have shown power consumption in the analog domain per channel, especially considering high-bandwidth threshold crossing. A considerable part of the power estimation comes from the amplification of the analog signal in order to achieve a high SNR [21]. Implementing this compression method in the analog domain can potentially result in far more power savings than in the digital counterpart. Reducing the number of channels through compression can lower the number of amplifiers used before the analog to-digital conversion and can lead to potentially lower power consumption. However, two important design aspects must be taken into consideration. Since the primary method of compression is to add channels based on the compression criterion, this process can have more ramifications in the analog domain due to phase misalignment between combined channels. For this reason, it is essential to consider using spiking features that allow for zero phase shift, like spike band power. Combining channels in the analog domain will require another set of summing amplifiers to perform the addition process.

The additional amplifiers can lead to an increase in power consumption initially. However, it is crucial to study, through power calculation simulations, the minimum compression ratio that needs to be achieved to offset this added power from the summing amplifiers, if any.

Compression in motor cortex vs other brain region

This compression method was mainly implemented on data recorded from motor regions in several animals across different species. This implementation was possible because we assumed the existence of the neural manifold within the low-dimensional subspace. There are a large number of studies that support this subspace hypothesis in the motor region [40, 30, 8, 43]. When considering other brain regions, this subspace hypothesis still needs to be consolidated as it is in the motor region. Several studies could not observe this low-dimensional subspace in sensory regions such as the visual cortex. One possible explanation for this disparity is that the complexity of the motor control task is low. Thus, the neural population variability can be confined to a low-dimensional subspace. This is challenged in the visual cortex as the complexity of the task scales with the number of stimuli presented, so when an N number of images are presented, the neural response lies in an N-dimensional subspace [50].

This study is proof that we can leverage latent neural dynamics for efficient estimation of brain state. We can compress neural input features by aiming to maintain the estimated single-trial neural trajectories in the low-dimensional latent space, potentially leading to power-efficient neural interfaces. Primarily in the motor cortex, more studies are emerging in which the latent variables are used to drive an online BMI [8, 11, 39]. Therefore, we emphasize in this study the importance of preserving these latent trajectories during the compression of the observations. We postulate that compression in neural interfaces is becoming relevant as the simultaneous recording

of the population of neurons increases in scale and expect more efficient compression techniques to emerge in the field in the near future.

Acknowledgments

Chapter 2, in full, is a reprint of Abdullah Alothman, Chao-li Wei, Pablo M. Tostado, Eric Trautmann, Xulu Sun, Daniel J. O'Shea, Ezequiel Arneodo, Timothy Q. Gentner, Vikash Gilja**,** *"Unsupervised Channel Compression Methods in Neural Prostheses Design"*.

We would like to thank Krishna Shenoy for conversations that helped shape the initial direction of this work. We thank members of the Gilja lab for the continuous feedback to refine the results for the manuscript. We especially thank Aashish Patel for his invaluable help providing compute assistance for this project.

Author Contribution

A.O. and V.G. conceptualized the project and built the algorithm. A.O. C.W, and V.G. performed the data analysis. E.T., X.S, and D.J.O provided the D1 neuropixel data. P.M.T., E.M.A., and T.Q.G Provided the D4 birdsong dataset. P.M.T. assisted with analyzing D4 dataset and determining optimal latent dimensionality. A.O. generated the figures. A.O. and V.G. wrote the manuscript. All authors discussed and edited the manuscript. V.G. supervised the work.

Competing Interest

V.G. holds shares in Neuralink, Corp., and Paradromics, Inc. and currently consults for Paradromics, Inc. These organizations had no role in study design, data collection and analysis, decision to publish, or preparation of the manuscript.

References

[1]Gopala K. Anumanchipalli, Josh Chartier, and Edward F. Chang. Speech synthesis from neural decoding of spoken sentences. *Nature*, 568(7753):493–498, April 2019. Number: 7753 Publisher: Nature Publishing Group.

[2]Sean L. Metzger, Jessie R. Liu, David A. Moses, Maximilian E. Dougherty, Margaret P. Seaton, Kaylo T. Littlejohn, Josh Chartier, Gopala K. Anumanchipalli, Adelyn Tu-Chan, Karunesh Ganguly, and Edward F. Chang. Generalizable spelling using a speech neuroprosthesis in an individual with severe limb and vocal paralysis. *Nature Communications*, 13(1):6510, November 2022. Number: 1 Publisher: Nature Publishing Group.

[3]Leigh R. Hochberg, Daniel Bacher, Beata Jarosiewicz, Nicolas Y. Masse, John D. Simeral, Joern Vogel, Sami Haddadin, Jie Liu, Sydney S. Cash, Patrick van der Smagt, and John P. Donoghue. Reach and grasp by people with tetraplegia using a neurally controlled robotic arm. *Nature*, 485(7398):372–375, May 2012. Number: 7398 Publisher: Nature Publishing Group.

[4]Jose M Carmena, Mikhail A Lebedev, Roy E Crist, Joseph E O'Doherty, David M Santucci, Dragan F Dimitrov, Parag G Patil, Craig S Henriquez, and Miguel A. L Nicolelis. Learning to Control a Brain–Machine Interface for Reaching and Grasping by Primates. *PLoS Biology*, 1(2):e42, October 2003.

[5]Aneesha K Suresh, James M Goodman, Elizaveta V Okorokova, Matthew Kaufman, Nicholas G Hatsopoulos, and Sliman J Bensmaia. Neural population dynamics in motor cortex are different for reach and grasp. *eLife*, 9:e58848, November 2020. Publisher: eLife Sciences Publications, Ltd.

[6]Francis R. Willett, Donald T. Avansino, Leigh R. Hochberg, Jaimie M. Henderson, and Krishna V. Shenoy. High-performance brain-to-text communication via handwriting. *Nature*, 593(7858):249–254, May 2021.

[7]Francis Willett, Erin Kunz, Chaofei Fan, Donald Avansino, Guy Wilson, Eun Young Choi, Foram Kamdar, Leigh R. Hochberg, Shaul Druckmann, Krishna V. Shenoy, and Jaimie M. Henderson. A high-performance speech neuroprosthesis, January 2023. Pages: 2023.01.21.524489 Section: New Results.

[8]Jonathan C. Kao, Paul Nuyujukian, Stephen I. Ryu, Mark M. Churchland, John P. Cunningham, and Krishna V. Shenoy. Single-trial dynamics of motor cortex and their applications to brainmachine interfaces. *Nature Communications*, 6(1):7759, November 2015.

[9]Vikash Gilja, Chethan Pandarinath, Christine H. Blabe, Paul Nuyujukian, John D. Simeral, Anish A. Sarma, Brittany L. Sorice, J´anos A. Perge, Beata Jarosiewicz, Leigh R. Hochberg, Krishna V. Shenoy, and Jaimie M. Henderson. Clinical translation of a high-performance neural prosthesis. *Nature Medicine*, 21(10):1142–1145, October 2015. Number: 10 Publisher: Nature Publishing Group.

[10]Chethan Pandarinath, Paul Nuyujukian, Christine H Blabe, Brittany L Sorice, Jad Saab, Francis R Willett, Leigh R Hochberg, Krishna V Shenoy, and Jaimie M Henderson. High performance communication by people with paralysis using an intracortical brain-computer interface. *eLife*, 6:e18554, February 2017. Publisher: eLife Sciences Publications, Ltd.

[11]Jonathan C. Kao, Stephen I. Ryu, and Krishna V. Shenoy. Leveraging neural dynamics to extend functional lifetime of brain-machine interfaces. *Scientific Reports*, 7(1):7395, August 2017. Number: 1 Publisher: Nature Publishing Group.

[12]John P. Cunningham, Paul Nuyujukian, Vikash Gilja, Cindy A. Chestek, Stephen I. Ryu, and Krishna V. Shenoy. A closed-loop human simulator for investigating the role of feedback control in brain-machine interfaces. *Journal of Neurophysiology*, 105(4):1932–1949, October 2010. Publisher: American Physiological Society.

[13]Ian H. Stevenson and Konrad P. Kording. How advances in neural recording affect data analysis. *Nature Neuroscience*, 14(2):139–142, February 2011. Number: 2 Publisher: Nature Publishing Grouup.

[14]Eric M. Trautmann, Janis K. Hesse, Gabriel M. Stine, Ruobing Xia, Shude Zhu, Daniel J. O'Shea, Bill Karsh, Jennifer Colonell, Frank F. Lanfranchi, Saurabh Vyas, Andrew Zimnik, Natalie A. Steinmann, Daniel A. Wagenaar, Alexandru Andrei, Carolina Mora Lopez, John O'Callaghan, Jan Putzeys, Bogdan C. Raducanu, Marleen Welkenhuysen, Mark Churchland, Tirin Moore, Michael Shadlen, Krishna Shenoy, Doris Tsao, Barundeb Dutta, and Timothy Harris. Large-scale brain-wide neural recording in nonhuman primates, February 2023. Pages: 2023.02.01.526664 Section: New Results.

[15]Angelique C. Paulk, Yoav Kfir, Arjun Khanna, Martina Mustroph, Eric M. Trautmann, Dan J. Soper, Sergey D. Stavisky, Marleen Welkenhuysen, Barundeb Dutta, Krishna V. Shenoy, Leigh R. Hochberg, Mark Richardson, Ziv M. Williams, and Sydney S. Cash. Large-scale neural recordings with single-cell resolution in human cortex using high-density Neuropixels probes. *bioRxiv*, page 2021.06.20.449152, June 2021. Publisher: Cold Spring Harbor Laboratory Section: New Results.

[16]Marius Pachitariu, Carsen Stringer, Mario Dipoppa, Sylvia Schr¨oder, L. Federico Rossi, Henry Dalgleish, Matteo Carandini, and Kenneth D. Harris. Suite2p: beyond 10,000 neurons with standard two-photon microscopy, July 2017. Pages: 061507 Section: New Results.

[17]John P. Cunningham and Byron M. Yu. Dimensionality reduction for large-scale neural recordings. *Nature Neuroscience*, 17(11):1500–1509, November 2014. Number: 11 Publisher: Nature Publishing Group.

[18]Nicholas A. Steinmetz, Cagatay Aydin, Anna Lebedeva, Michael Okun, Marius Pachitariu, Marius Bauza, Maxime Beau, Jai Bhagat, Claudia B¨ohm, Martijn Broux, Susu Chen, Jennifer Colonell, Richard J. Gardner, Bill Karsh, Fabian Kloosterman, Dimitar Kostadinov, Carolina Mora-Lopez, John O'Callaghan, Junchol Park, Jan Putzeys, Britton Sauerbrei, Rik J. J. van Daal, Abraham Z. Vollan, Shiwei Wang, Marleen Welkenhuysen, Zhiwen Ye, Joshua T. Dudman, Barundeb Dutta, Adam W. Hantman, Kenneth D. Harris, Albert K. Lee, Edvard I. Moser, John O'Keefe, Alfonso Renart, Karel Svoboda, Michael H¨ausser, Sebastian Haesler, Matteo Carandini, and Timothy D. Harris. Neuropixels 2.0: A miniaturized high-density probe for stable, long-term brain recordings. *Science*, 372(6539):eabf4588, April 2021. Publisher: American Association for the Advancement of Science.

[19]Kunal Sahasrabuddhe, Aamir A. Khan, Aditya P. Singh, Tyler M. Stern, Yeena Ng, Aleksandar Tadi´c, Peter Orel, Chris LaReau, Daniel Pouzzner, Kurtis Nishimura, Kevin M. Boergens, Sashank Shivakumar, Matthew S. Hopper, Bryan Kerr, Mina-Elraheb S. Hanna, Robert J. Edgington, Ingrid McNamara, Devin Fell, Peng Gao, Amir Babaie-Fishani, Sampsa Veijalainen, Alexander V. Klekachev, Alison M. Stuckey, Bert Luyssaert, Takashi D. Y. Kozai, Chong Xie, Vikash Gilja, Bart Dierickx, Yifan Kong, Malgorzata Straka, Harbaljit S. Sohal, and Matthew R. Angle. The Argo: a high channel count recording system for neural recording in vivo. *Journal of Neural Engineering*, 18(1):015002, February 2021. Publisher: IOP Publishing.

[20]Patrick D. Wolf. Thermal Considerations for the Design of an Implanted Cortical Brain–Machine Interface (BMI). In William M. Reichert, editor, *Indwelling Neural Implants: Strategies for Contending with the In Vivo Environment*, Frontiers in Neuroengineering. CRC Press/Taylor & Francis, Boca Raton (FL), 2008.

[21]Samuel R. Nason, Alex K. Vaskov, Matthew S. Willsey, Elissa J. Welle, Hyochan An, Philip P. Vu, Autumn J. Bullard, Chrono S. Nu, Jonathan C. Kao, Krishna V. Shenoy, Taekwang Jang, Hun-Seok Kim, David Blaauw, Parag G. Patil, and Cynthia A. Chestek. A low-power band of neuronal spiking activity dominated by local single units improves the performance of brain–machine interfaces. *Nature Biomedical Engineering*, 4(10):973–983, October 2020.

[22]Nir Even-Chen, Dante G. Muratore, Sergey D. Stavisky, Leigh R. Hochberg, Jaimie M. Henderson, Boris Murmann, and Krishna V. Shenoy. Power-saving design opportunities for wireless intracortical brain–computer interfaces. *Nature Biomedical Engineering*, August 2020.

[23]Saurabh Vyas, Matthew D. Golub, David Sussillo, and Krishna V. Shenoy. Computation Through Neural Population Dynamics. *Annual Review of Neuroscience*, 43(1):249–275, July 2020.

[24]Juan A. Gallego, Matthew G. Perich, Stephanie N. Naufel, Christian Ethier, Sara A. Solla, and Lee E. Miller. Cortical population activity within a preserved neural manifold underlies multiple motor behaviors. *Nature Communications*, 9(1):4233, October 2018. Number: 1 Publisher: Nature Publishing Group.

[25]Barbara Feulner and Claudia Clopath. Neural manifold under plasticity in a goal driven learning behaviour. *PLOS Computational Biology*, 17(2):e1008621, February 2021. Publisher: Public Library of Science.

[26]MM Churchland, JP Cunningham, MT Kaufman, JD Foster, P Nuyujukian, SI Ryu, and KV Shenoy. Neural population dynamics during reaching. *Nature*, 487(7405):51–56, July 2012.

[27]Patrick T. Sadtler, Kristin M. Quick, Matthew D. Golub, Steven M. Chase, Stephen I. Ryu, Elizabeth C. Tyler-Kabara, Byron M. Yu, and Aaron P. Batista. Neural constraints on learning. *Nature*, 512(7515):423–426, August 2014.

[28]Juan A. Gallego, Matthew G. Perich, Lee E. Miller, and Sara A. Solla. Neural Manifolds for the Control of Movement. *Neuron*, 94(5):978–984, June 2017.

[29]Krishna V. Shenoy, Maneesh Sahani, and Mark M. Churchland. Cortical Control of Arm Movements: A Dynamical Systems Perspective. *Annual Review of Neuroscience*, 36(1):337–359, 2013. eprint: https://doi.org/10.1146/annurev-neuro-062111-150509.

[30]Barbara Feulner, Matthew G. Perich, Raeed H. Chowdhury, Lee E. Miller, Juan A. Gallego, and Claudia Clopath. Small, correlated changes in synaptic connectivity may facilitate rapid motor learning. *Nature Communications*, 13(1):5163, September 2022. Number: 1 Publisher: Nature Publishing Group.

[31]Peiran Gao, Eric Trautmann, Byron Yu, Gopal Santhanam, Stephen Ryu, Krishna Shenoy, and Surya Ganguli. A theory of multineuronal dimensionality, dynamics and measurement. preprint, Neuroscience, November 2017.

[32]Chethan Pandarinath, Daniel J. O'Shea, Jasmine Collins, Rafal Jozefowicz, Sergey D. Stavisky, Jonathan C. Kao, Eric M. Trautmann, Matthew T. Kaufman, Stephen I. Ryu, Leigh R. Hochberg, Jaimie M. Henderson, Krishna V. Shenoy, L. F. Abbott, and David Sussillo. Inferring single-trial neural population dynamics using sequential auto-encoders. *Nature Methods*, 15(10):805–815, October 2018. Number: 10 Publisher: Nature Publishing Group.

[33]Byron M. Yu, John P. Cunningham, Gopal Santhanam, Stephen I. Ryu, Krishna V. Shenoy, and Maneesh Sahani. Gaussian-Process Factor Analysis for Low-Dimensional Single-Trial Analysis of Neural Population Activity. *Journal of Neurophysiology*, 102(1):614–635, July 2009.

[34]Yuan Zhao and Il Memming Park. Variational Latent Gaussian Process for Recovering Single-Trial Dynamics from Population Spike Trains. *Neural Computation*, 29(5):1293–1316, May 2017.

[35]Omid G. Sani, Hamidreza Abbaspourazad, Yan T. Wong, Bijan Pesaran, and Maryam M. Shanechi. Modeling behaviorally relevant neural dynamics enabled by preferential subspace identification. *Nature Neuroscience*, 24(1):140–149, January 2021. Number: 1 Publisher: Nature Publishing Group.

[36]Tze Hui Koh, William E. Bishop, Takashi Kawashima, Brian B. Jeon, Ranjani Srinivasan, Yu Mu, Ziqiang Wei, Sandra J. Kuhlman, Misha B. Ahrens, Steven M. Chase, and Byron M. Yu. Dimensionality reduction of calcium-imaged neuronal population activity. *Nature Computational Science*, 3(1):71–85, January 2023. Number: 1 Publisher: Nature Publishing Group.

[37]Feng Zhu, Harrison A. Grier, Raghav Tandon, Changjia Cai, Anjali Agarwal, Andrea Giovannucci, Matthew T. Kaufman, and Chethan Pandarinath. A deep learning framework for inference of single-trial neural population dynamics from calcium imaging with subframe temporal resolution. *Nature Neuroscience*, 25(12):1724–1734, December 2022. Number: 12 Publisher: Nature Publishing Group.

[38]Sean M. Perkins, John P. Cunningham, Qi Wang, and Mark M. Churchland. Simple decoding of behavior from a complicated neural manifold, April 2023. Pages: 2023.04.05.535396 Section: New Results.

[39]Andres Agudelo-Toro, Jonathan A. Michaels, Wei-An Sheng, and Hansj¨org Scherberger. Accurate neuroprosthetic control through latent state transition training, June 2023. Pages: 2023.06.02.543242 Section: New Results.

[40]Juan A. Gallego, Matthew G. Perich, Raeed H. Chowdhury, Sara A. Solla, and Lee E. Miller. Long-term stability of cortical population dynamics underlying consistent behavior. *Nature Neuroscience*, 23(2):260–270, February 2020. Number: 2 Publisher: Nature Publishing Group.

[41]Alan D. Degenhart, William E. Bishop, Emily R. Oby, Elizabeth C. Tyler-Kabara, Steven M. Chase, Aaron P. Batista, and Byron M. Yu. Stabilization of a brain–computer interface via the alignment of low-dimensional spaces of neural activity. *Nature Biomedical Engineering*, 4(7):672–685, July 2020. Number: 7 Publisher: Nature Publishing Group.

[42]Surya Ganguli and Haim Sompolinsky. Compressed Sensing, Sparsity, and Dimensionality in Neuronal Information Processing and Data Analysis. *Annual Review of Neuroscience*, 35(1):485– 508, 2012. eprint: https://doi.org/10.1146/annurev-neuro-062111-150410.

[43]Eric M. Trautmann, Sergey D. Stavisky, Subhaneil Lahiri, Katherine C. Ames, Matthew T. Kaufman, Daniel J. O'Shea, Saurabh Vyas, Xulu Sun, Stephen I. Ryu, Surya Ganguli, and Krishna V. Shenoy. Accurate Estimation of Neural Population Dynamics without Spike Sorting. *Neuron*, 103(2):292–308.e4, July 2019. Publisher: Elsevier.

[44]Breanne P Christie, Derek M Tat, Zachary T Irwin, Vikash Gilja, Paul Nuyujukian, Justin D Foster, Stephen I Ryu, Krishna V Shenoy, David E Thompson, and Cynthia A Chestek. Comparison of spike sorting and thresholding of voltage waveforms for intracortical brain–machine interface performance. *Journal of Neural Engineering*, 12(1):016009, February 2015.

[45]Cynthia A. Chestek, Vikash Gilja, Paul Nuyujukian, Justin D. Foster, Joline M. Fan, Matthew T. Kaufman, Mark M. Churchland, Zuley Rivera-Alvidrez, John P. Cunningham, Stephen I. Ryu, and Krishna V. Shenoy. Long-term stability of neural prosthetic control signals from silicon cortical arrays in rhesus macaque motor cortex. *Journal of Neural Engineering*, 8(4):045005, July 2011.

[46]Patrick N. Lawlor, Matthew G. Perich, Lee E. Miller, and Konrad P. Kording. Linear-nonlineartime-warp-poisson models of neural activity. *Journal of Computational Neuroscience*, 45(3):173– 191, December 2018.

[47]Matthew G. Perich, Patrick N. Lawlor, Konrad P. Kording, and Lee E. Miller. Extracellular neural recordings from macaque primary and dorsal premotor motor cortex during a sequential reaching task, 2018. Artwork Size: 400 MB Medium: application/matlab Pages: 400 MB.

[48]Felix Pei, Joel Ye, David Zoltowski, Anqi Wu, Raeed H. Chowdhury, Hansem Sohn, Joseph E. O'Doherty, Krishna V. Shenoy, Matthew T. Kaufman, Mark Churchland, Mehrdad Jazayeri, Lee E. Miller, Jonathan Pillow, Il Memming Park, Eva L. Dyer, and Chethan Pandarinath. Neural Latents Benchmark '21: Evaluating latent variable models of neural population activity, January 2022. arXiv:2109.04463 [cs, q-bio].

[49]Mark Churchland and Matthew Kaufman. MC maze large: macaque primary motor and dorsal premotor cortex spiking activity during delayed reaching.

[50]Carsen Stringer, Marius Pachitariu, Nicholas Steinmetz, Matteo Carandini, and Kenneth D. Harris. High-dimensional geometry of population responses in visual cortex. *Nature*, 571(7765):361–365, July 2019. Number: 7765 Publisher: Nature Publishing Group.

Supplementary Figures

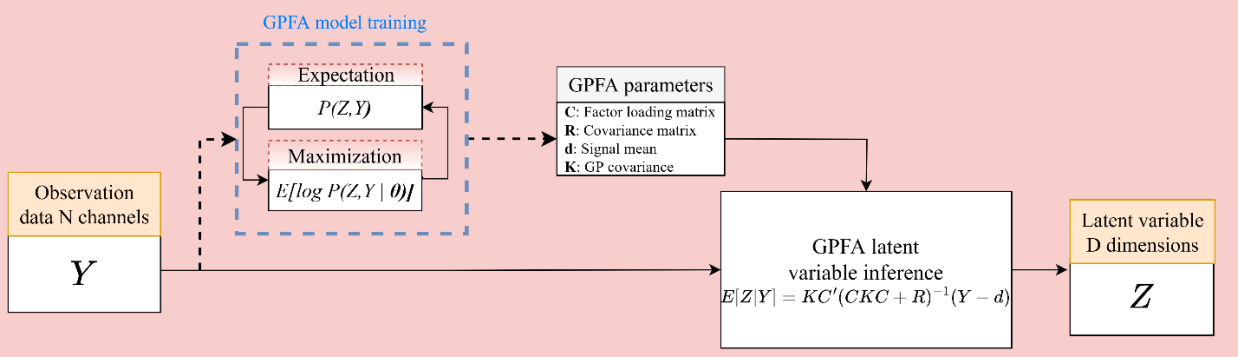

Figure 2.7 **Extracting latents and GPFA parameters.**

GPFA extracts the latent trajectories of single trials through EM iterative process. In the E-step, the conditional probability for all trajectories X given the observations $Y, P(Z|Y)$ is estimated through the jointly Gaussian distribution $P(Z,Y)$. The M-step maximizes $E[logP(Z,Y|\theta)]$ with respect to GPFA parameters which in turn, used to infer the trajectory of the latent variable with respect to the observations.

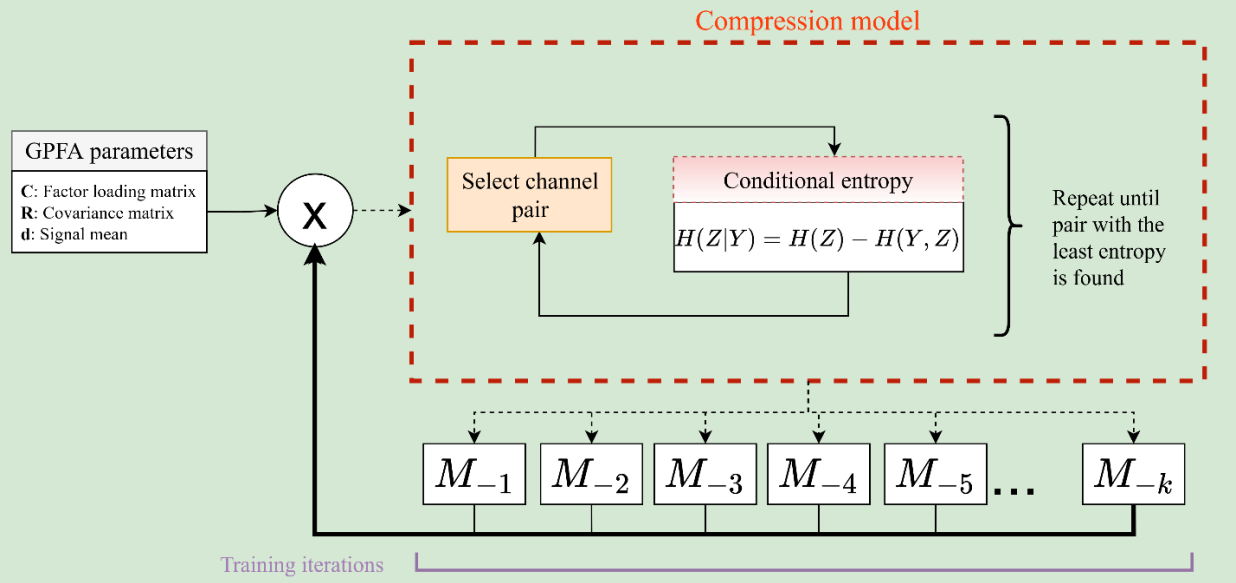

Figure 2.8 **Training compression model.**

When GPFA parameters are trained, they are used to find the best two channels to compress by combining. This is done in iterative loop by measuring the conditional entropy in all possible channel pairs, and the pair with the least amount of entropy (least decrease in mutual information) is selected. Then a compression mapping matrix M_{-1} is output into the GPFA parameters to apply the newly trained compression. This process is repeated with new compression mapping matrix M_{-k} is output at the end of every training iteration until a stopping criterion is met (certain value of conditional, certain compressed dimensionality...etc).

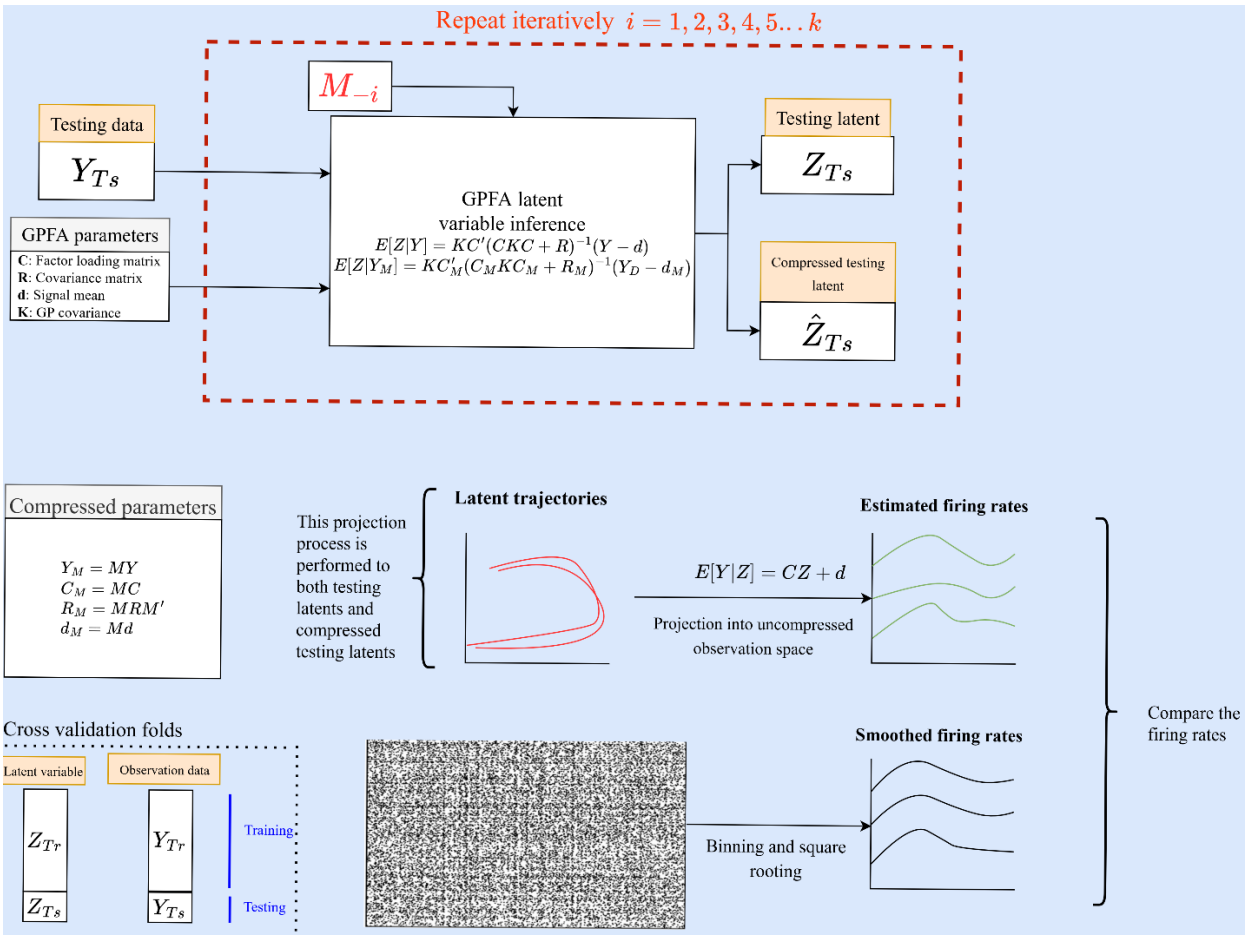

Figure 2.9 **Inferring latent trajectories and projecting into higher dimensional space.**

When the compression model is trained and a list of mapping matrices are output, they are evaluated through testing how preserved the inferred latent trajectories are, which is the core of this compression method. These trajectories are inferred at every compression matrix $M-1, M-2, M-3 \ldots M-k$ to evaluate how they gradually change during the compression process. One evaluation metric is to project these latent trajectories into the observation space to reconstruct the observation data Y_{Ts} and compare to the original neural data through error measurement.

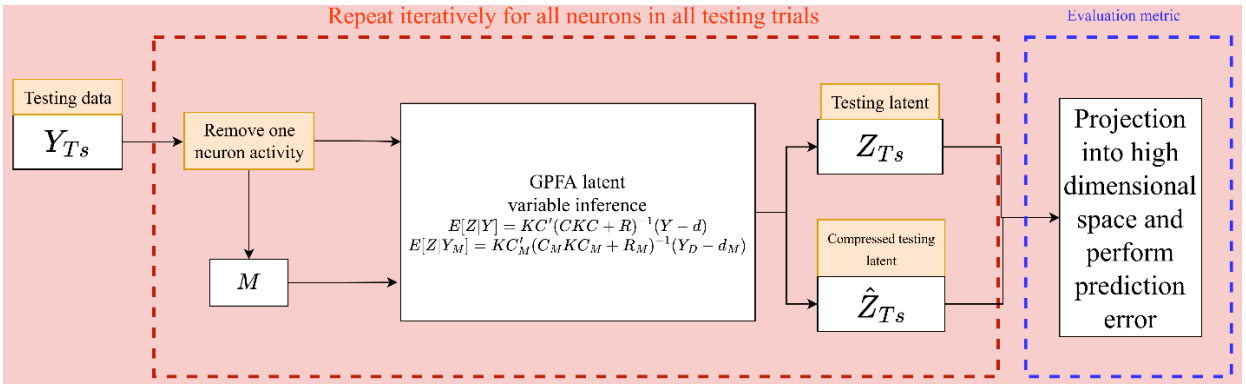

Figure 2.10 **Leave-out neuron prediction test.**

One of the main evaluation metrics is prediction error, which tests how well the inferred trajectories can predict the activity of a left-out neuron. Initially the latent trajectories are inferred after removing one neuron (GPFA parameters are scaled down [33]). Those trajectories are then projected into the observation space where they predict the activity of all neurons including the left-out one. Prediction error metric is calculated through measuring the mean squared error between left-out neuron and its predicted activity. This is performed for all neurons in the testing set.

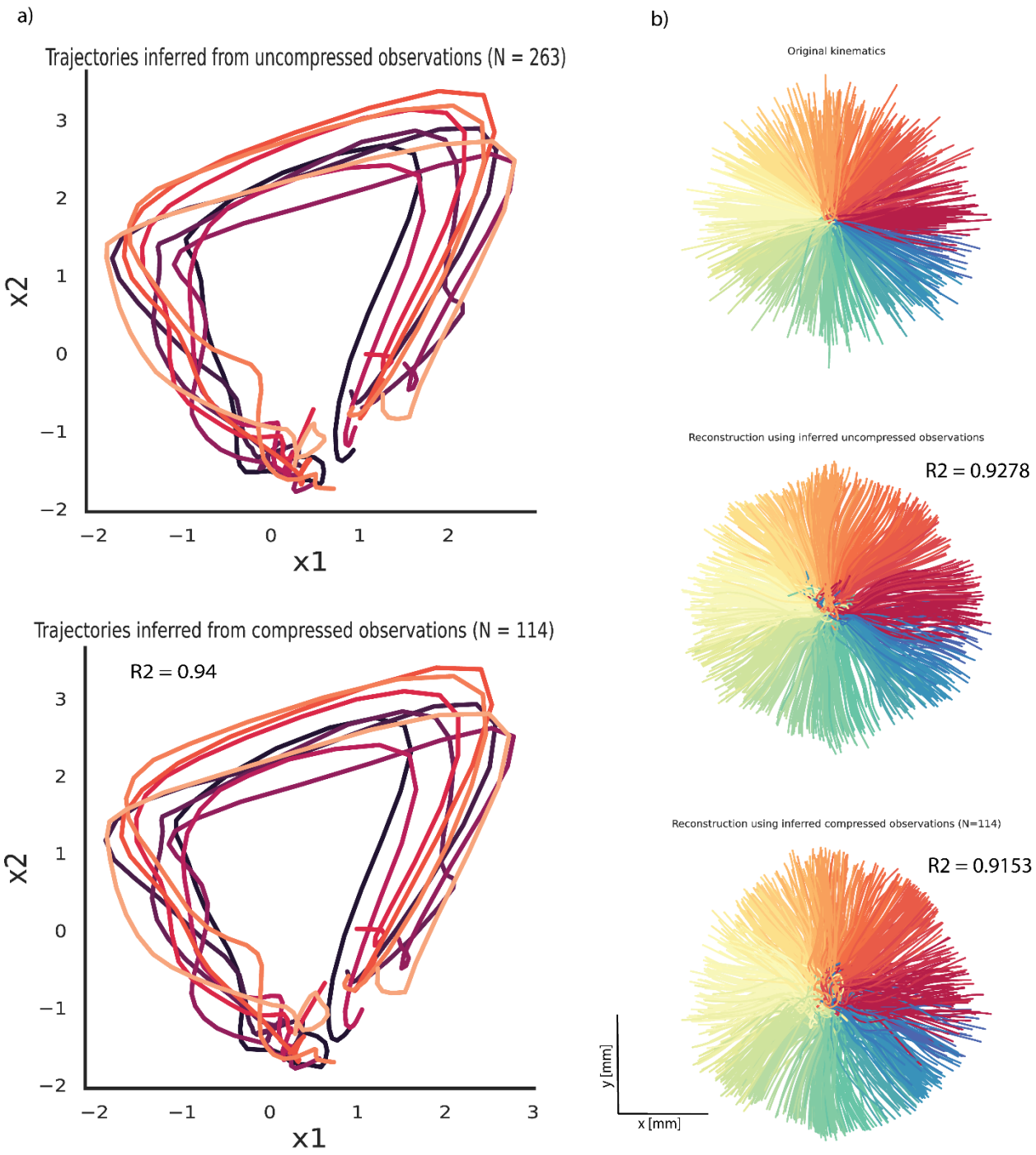

Figure 2.11 **Latent trajectories inferred in D1 dataset.**

a) an example of inferred latent trajectories of 10 different trials of the same condition in D1 dataset. The figure compares the trajectories obtained from the uncompressed dataset and after compressing by more than 50 percent. b) shows the kinematic Reconstruction using inferred firing rates estimated using Latent Factor Analysis via Dyanmical Systems (LFADS) [32]. It compares the original kinematics to the Reconstruction using uncompressed dataset and after compressing by more than 50 percent.

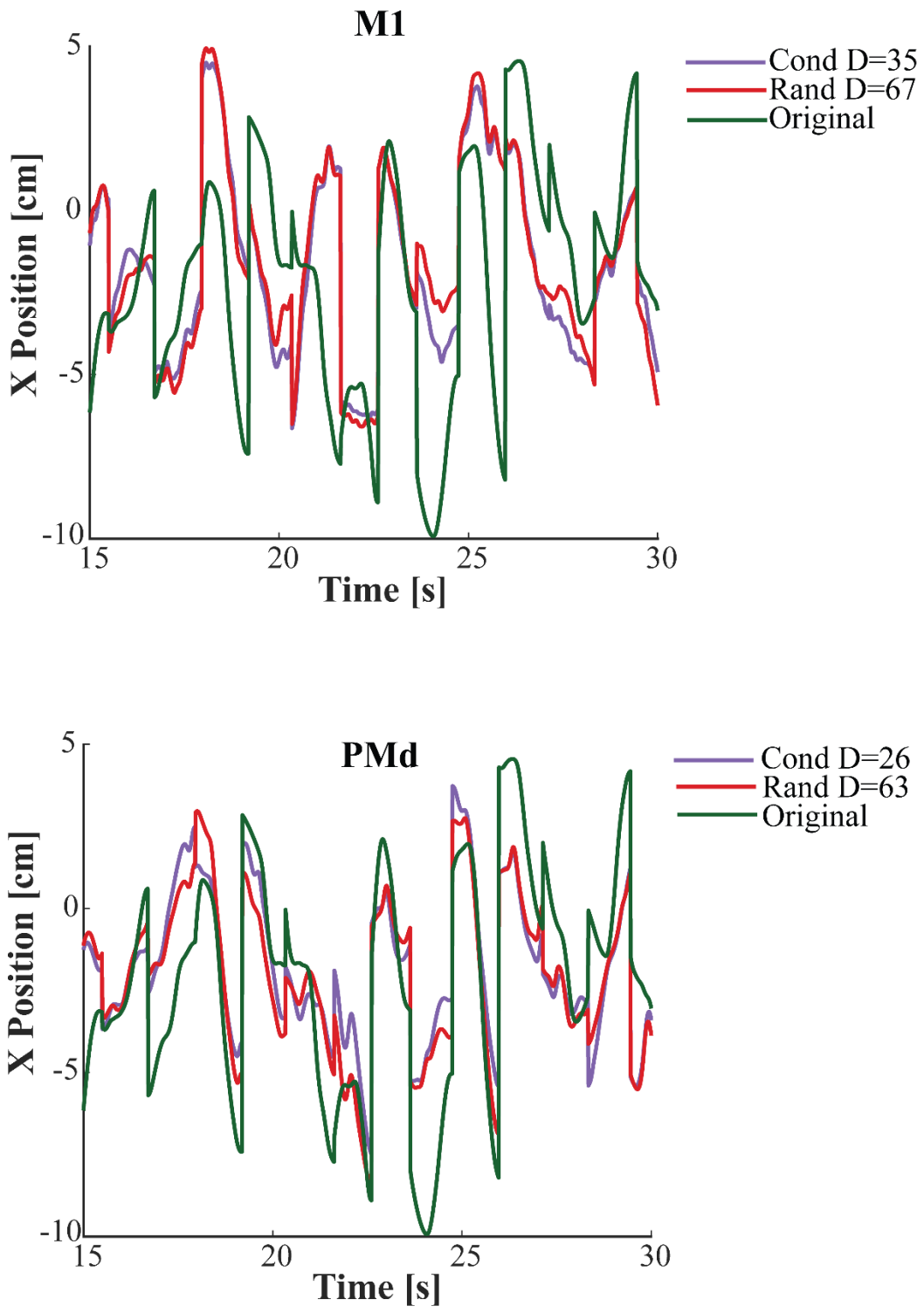

Figure 2.12 **Kinematic reconstruction of arm x-position in D2 dataset.**

This figure compares the kinematic reconstruction in two different regions using two different compression methods with the original kinematics as a reference. The figure shows that our compression method achieves similar reconstruction to the random-projection-based compression method at half the feature dimensionality.

Chapter 3

Cellular Calcium Activity at Depth Predicted from Surface Potential Recordings using Ultra-high Density Transparent Graphene Arrays

Overview

Advances in neural recording technology and fabrication have made it possible to record neural modalities simultaneously from the same brain region. This, in turn, allows to combine different temporal and spatial scales provided by the recorded modalities. Specifically, through the development of transparent graphene arrays, one can record surface electrophysiological activity and image Calcium response at depth. We study the correlation between these recordings and show that we can predict the activity of one modality using features of the other modality through decoding its neural modes.

Introduction

The brain is a high dimensional system that evolves over time with complex dynamics that require a wide set of spatial and temporal scales [1-3]. For the temporal scale, modalities span a wide range of time resolution, from microseconds, such as change in potential in the neuron, to several hours or days, in case of learning new behavior. While spatially, responses can range from synapses to cells, circuits, and whole brain monitoring. Examining population dynamics across such a diverse range of spatial and temporal scales is impossible with one neural recording technology. For that reason, numerous studies sought to combine technologies and recording interfaces to simultaneously record multiple modalities during experimental procedures. Such studies aimed to investigate the dynamics of neural populations in various applications [4-21].

One of the prominent multimodal approaches is to combine electrophysiological and optical recording as the modality-specific information we can learn compliments each other. Namely, the fine temporal resolution of electrophysiology made it possible to investigate fast spiking activity in the brain. On other the hand, imaging Calcium dynamics in neurons provides a complimentary view of the neuronal population activity with dense spatial resolution. Between these two modalities and what they provide, there is a large amount of information which can be obtained that help us understand neuronal activity better [22] and have more accurate detection of cell-specificity in response to cognitive processes [23,24]. This integration of optical and electrical modalities was made possible using transparent graphene electrodes with artifact-free recording capability [25-29].

In this chapter, we present the results of a Collaboratory work with Kuzum group (Neuroelectronics Lab, UCSD) and Komiyama group to investigate and understand the correlation between two modalities recorded simultaneously in mice responding to visual stimuli. The primary visual cortex (V1) was targeted because the neural populations in this region exhibit diverse responses and selectivity to various attributes of the visual stimuli [75-80]. We show that there is a high correlation between the high frequencies of surface potential and calcium recordings at layer L2/L3. We extract latent representative trajectories from the calcium response using Gaussian Process Factor Analysis (GPFA) and decode those latent variables from a trained recurrent neural network using spectral features of surface recordings. We project those decoded latents to the original population space to reconstruct single activity in the calcium response. Additionally, we look into the difference between stimuli-evoked and spontaneous activity, how can it can affect neuronal population coupling and the decoding accuracy of latent modes, which consequently translates to accuracy of single-cell projections in the high dimensional space. In this Collaboratory work, Kuzum group designed and fabricated the transparent graphene technology that enabled such multimodal recording and Komiyama group implanted and performed the experiment.

Results

In-vivo multimodal experiments with transgenic mice

Mehrdad et al. performed the experiment with transparent graphene arrays to record electrophysiological signals from cortical surface. Simultaneously, they conducted calcium imaging using two-photon microscopy from the visual cortex in transgenic mice which was expressing GCaMP6s in most cortical excitatory neurons [83,84]. The animal is responding to

visual stimulation using drifting gratings (Figure 3.1). The two-photon imaging was performed at two different depths, layer 1 at 50 μm and layers 2/3 at 225 μm in a field of view of

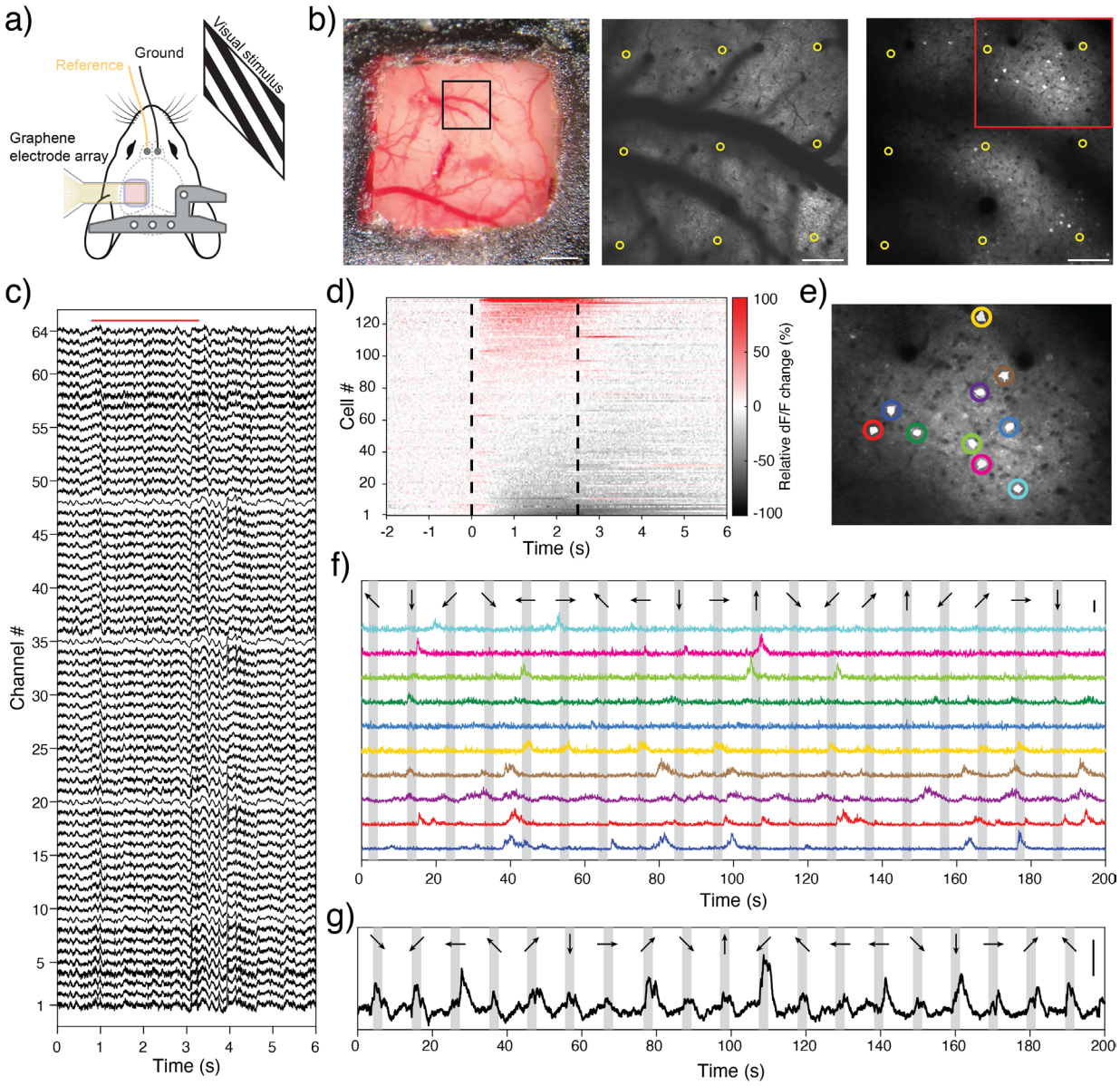

Figure 3.1 **Multimodal experiment combing surface recording and optical imaging at depth in transgenic mice.**

In this figure, a) shows the experimental setup. b) exposed visual cortex (black box depict the optical field of view). c) sample of surface potential recorded from 64 channels. d) Trial averaged population activity (relative to the 2-second baseline before stimulus onset) of neurons detected in L2/L3. Dashed lines show stimulus onset/offset respectively. e) and f) show 10 highlighted neurons and their $\Delta F/F$ signals. g) shows averaged calcium signal in layer 1.

$960\ \mu m\ \times\ 960\ \mu m$ that span over nine channels. A sample of the 64 channels recorded at the cortical surface during one trial of the stimulus. The calcium response was estimated by extracting fluorescence tracing and calculating the relative change in intensity $\Delta F/F$. The imaging quality was not distorted by the transparent graphene array and allowed for recordings at single-cell resolutions. In Figure 3.1e) and f), a sample of ten recorded neurons and their calcium response is shown.

Predicting Neural Activity in Layer 1 and Layer 2-3 from Surface Recordings

Mehrdad et al. asked whether it is possible to predict brain activity at deeper layers using spectral neural features of surface recordings in order to investigate the correlations surface recordings and calcium imaging. They implemented a neural network model consisting of a single layer LSTM network [22,59]. The purpose of this neural network is to learn the nonlinear relationship between the two modalities. The network was fed the power of signals at different frequency bands (δ: 1–4 Hz, θ: 4–7 Hz, α: 8–15 Hz, β: 15–30 Hz, γ: 31–59 Hz, H-γ: 61–200 Hz, MUA: 0.5–4 kHz) in order to predict the average calcium activity at both layer 1 and layer 2/3 (Figure 3.2a). The 40-minute were split into eight-minute sections to perform five-fold cross validations. Examples of decoded and ground truth activities in L1 and L2/3 are shown in Figure 3.2b and the results show high decoding accuracy of the average activity in both layers. Additionally, the decoding accuracy was measured as a function of the number of channels from which spectral features were extracted and fed to the neural network model (figure 3.2c). The decoding performance increased with the inclusion of more channels in order of their proximity to the FoV. The performance saturates when using the 20 channels overlapping the FoV (Figure 3.3), suggesting that further channels add little to no benefit. Lastly, by fixing the number of

channels used at 20 channels, Mehrdad et al. investigated the contribution of different frequency bands to the decoding performance. They used the low (δ, θ, α, and β) and high (γ, H-γ, MUA) frequency

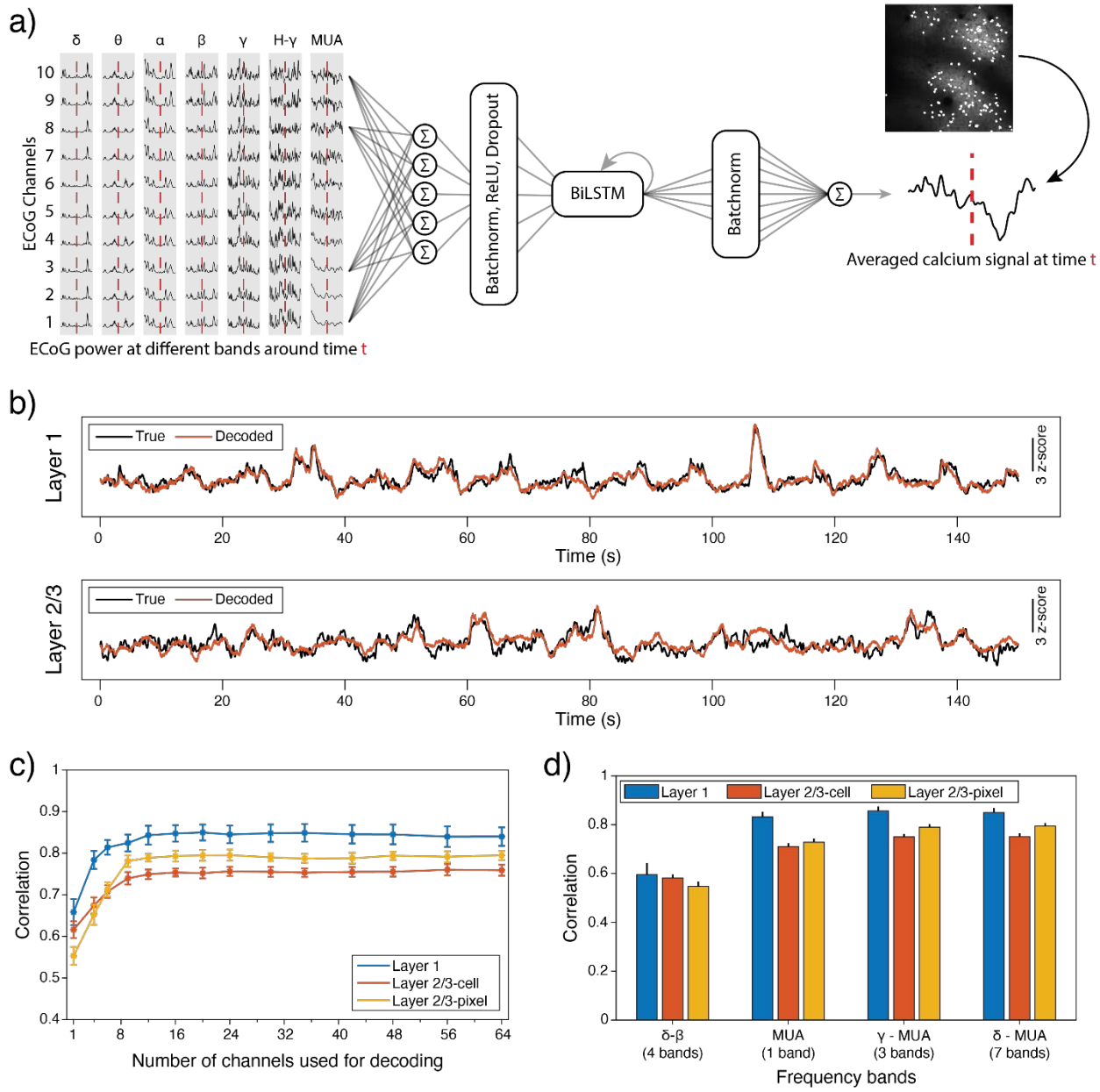

Figure 3.2 **Decoding the average calcium activity from recorded surface potentials.**

(**a**) Schematic of the decoding model. Signal powers at different frequency bands (ten channels are shown as example) around time t are used as inputs to the model to decode the calcium activity at time t. The model consists of a linear hidden layer, a single-layer LSTM network, and a linear readout layer. (**b**) Decoded (orange) vs ground truth (black) ΔF/F of layer 1 and layer 2/3 (cell-averaged). (**c**) Decoding performance for layer 1 and layer 2/3 (cell and pixel-level averaged) using all seven frequency bands but different numbers of channels. (**d**) Decoding performance for layer 1 and layer 2/3 (cell and pixel-level averaged) using different frequency bands of the 20 channels closest to the FoV.

components to decode the average calcium activity in layer 1 and layers 2/3. Figure 3.2d shows higher frequency components have higher decoding accuracy compared to using low frequency components only. Additionally, the figure shows that adding low frequency components provides no additional information to the model when the high frequency components are used.

48	35	20	9	2	3	10	21
47	34	19	8	1	4	11	22
46	33	18	7	6	5	12	23
45	32	17	16	15	14	13	24
44	31	30	29	28	27	26	25
43	42	41	40	39	38	37	36
56	55	54	53	52	51	50	49
64	63	62	61	60	59	58	57

Figure 3.3 **Schematics for surface array channel diagram with emphasis on Calcium imaging FoV**.
Red area shows the imaging FoV, and blue box indicates the closest 20 surface ECoG channels to the FoV.

Predicting Single-cell Activity from Surface Recordings

Given how average calcium activity at depth can be decoded using spectral features of surface recordings, we asked whether we could predict the calcium activity at single-cell level using cortical potentials. One approach was to develop a single neural network model for all the

136 neurons recorded in the FoV, but that would be inefficient and excessively complex. Another approach is to decode a latent dimensionality that is very representative of the high dimensional population activity. Previous studies showed that most of the covariance in neural population activity is confined within a neural manifold in the latent space [88,89]. Therefore we extract the latent trajectories in the low dimensional space using Gaussian Process Factor Analysis (GPFA), a generative model that unifies dimensionality reduction and smoothing in one framework to extract latent representations that describe the shared variability of high-dimensional data [90]. We trained GPFA to find and extract the low-dimensional trajectories of the calcium activity. We used eight distinct latent modes that can explain most of the shared variance in the high dimensional data (Figure 3.6). Next, Mehrdad et al. built a network architecture for each one of these latent modes to be decoded using the spectral feature of the surface recording. To reconstruct the single-cell calcium fluorescence, we projected the decoded latent variables to high dimensional space using the GPFA parameters. The schematic in Figure 3.4a shows the three main steps in single-cell decoding which are dimensionality reduction using GPFA, prediction using neural network, and projection to high dimensional space. Figure 3.4b shows a sample of a decoded vs ground truth of single cell activities which demonstrate the possibility of inferring population activity at depth using surface recordings. Additionally, the reconstruction accuracy can be seen in Figure 3.4c for all 136 neurons captured by calcium imaging while we compare the reconstruction using true latents and decoded latents as a function of number of variables in Figure 3.9. Lastly, we used reduced GPFA to plot the latent trajectories of all the trials to demonstrate condition separability in the low dimensional space (Figure 3.11).

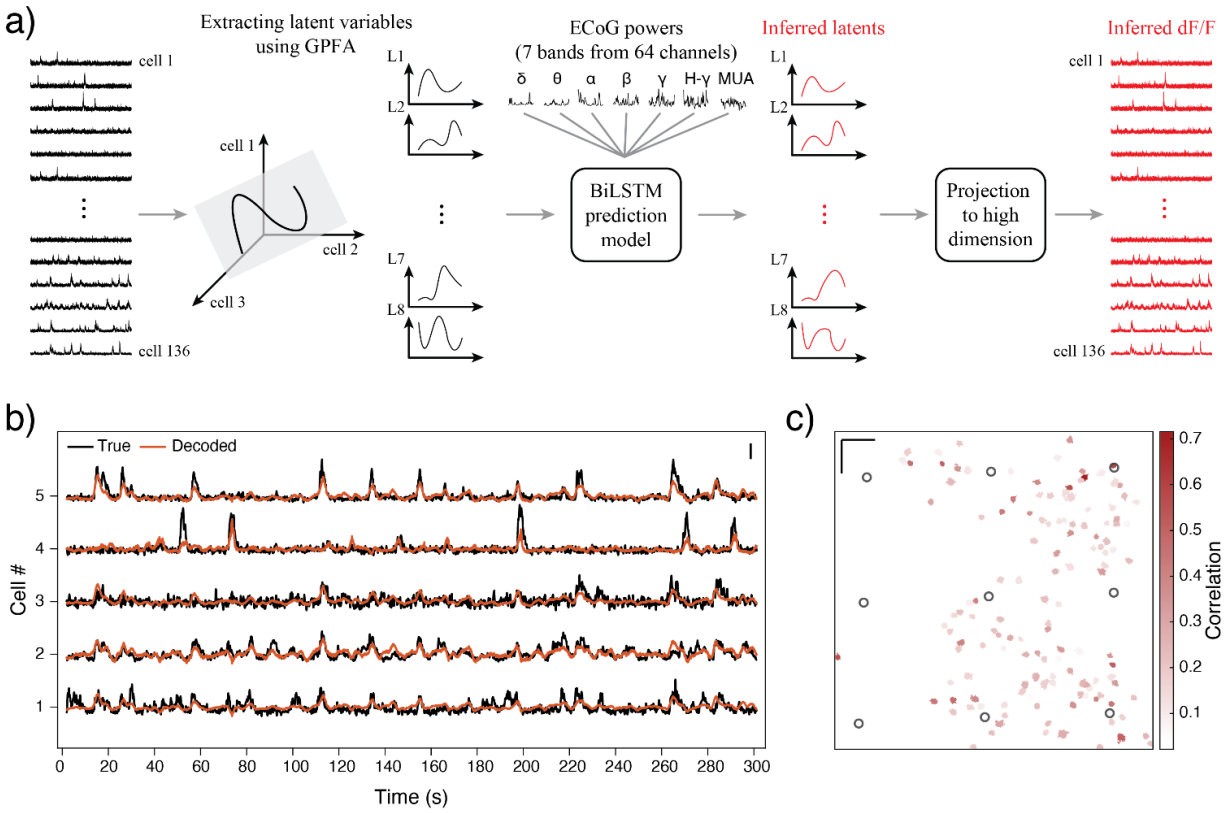

Figure 3.4 **Decoding single-cell calcium activity from surface potentials using latent variables.**

a) Diagram of single-cell decoding model. Eight latent variables are extracted using GPFA are used to train BiLSTM models. Inferred and decoded latent variables are projected to high-dimensional space to reconstruct single-cell ΔF/F signals. (**b**) Examples for decoded (orange) vs ground truth (black) ΔF/F of layer 2/3 cells. (**c**) Decoding performance for all 136 cells with their locations outlined in the FoV. Black circles are the 9 channels inside the FoV.

Effect of population coupling on decoding accuracy

Next, we investigated whether the high accuracy of our decoding model is a result of the low variance of drifting gratings and the population coupling of neurons in response to the visual stimulus. Previous studies showed that spontaneous activity in the visual cortex is more complex than evoked responses [91], as it has similar population coupling to more complex visual task like presenting natural images [92, 93]. Therefore, to further assess the performance of our decoding model, we applied our decoding strategy to a separate dataset acquired from sessions without any visual stimulus (spontaneous activity). We repeated the single-cell calcium decoding and

successfully inferred the calcium activity of single neurons in the spontaneous sessions. In Figure 3.7d/e, we compare the decoding of spontaneous activity vs evoked activity (using drifting grating) by using only the neurons present in both sessions.

In order to investigate the effect of the population coupling on decoding performance, we calculated the coupling in both the spontaneous and evoked sessions using two distinct methods. We found there is a wide diversity in the neuronal coupling between the two sessions, and neurons that are highly coupled in one session can display low coupling in the other session (Figure 3.5a/b). Further investigation into relationship between coupling and decoding results show that there are little correlation as highly coupled neurons can have low decoding results and vice versa, neurons with low coupling can have high decoding results (Figure 3.5c/d). Lastly, we investigated whether the cells with high decoding performance had different population coupling. By calculating the coupling for the top N neurons in both evoked and spontaneous datasets, we found out that evoked has better decoding accuracy while having lower population coupling (Figure 3.5e-h). This suggests that the decoding accuracy is not entirely dependent on the population coupling and can be a combination of multiple factors.

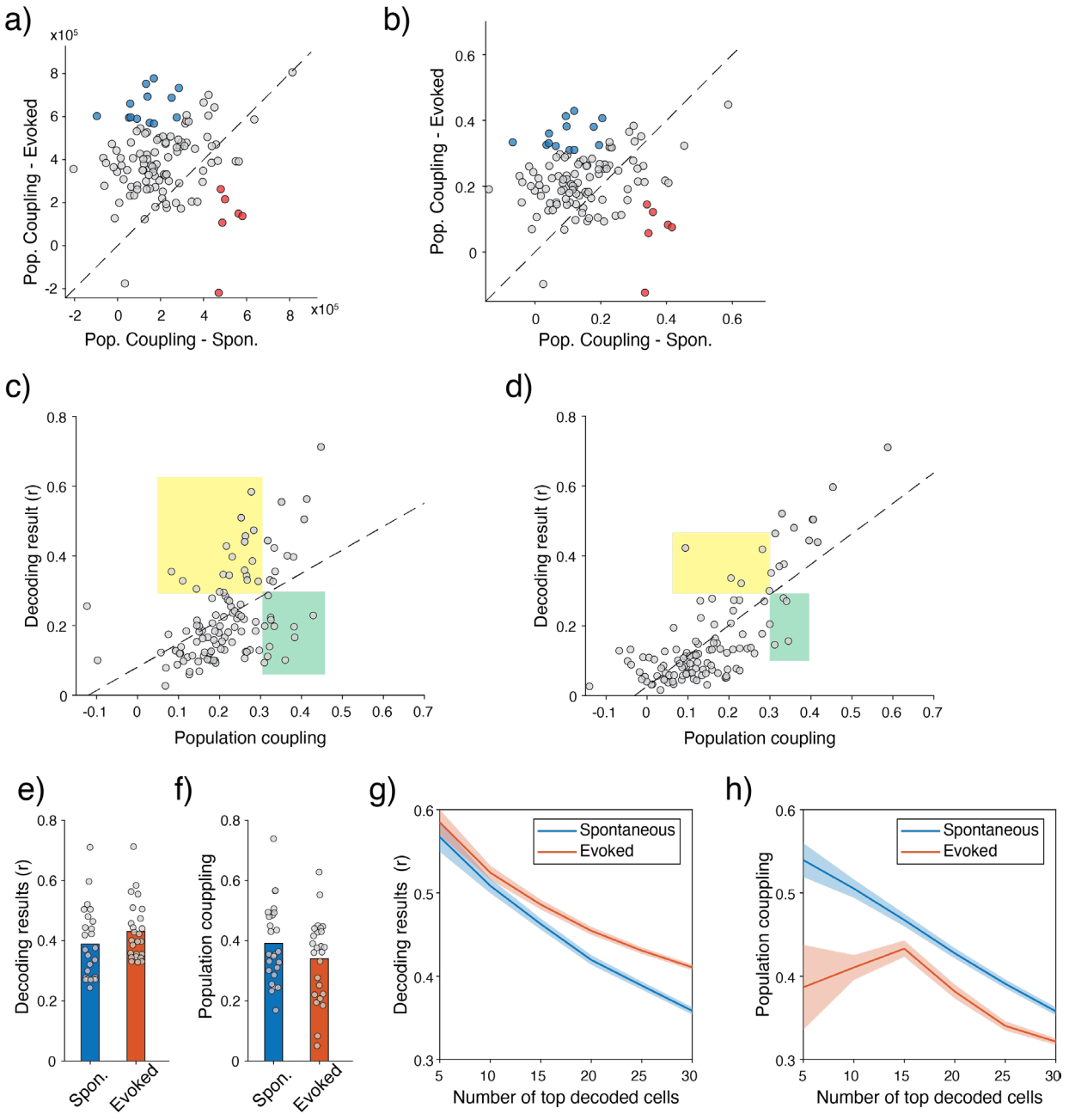

Figure 3.5 **The relationship between population coupling and single-cell calcium decoding**.

(**a, b**) Comparison of population coupling across cells in the spontaneous and evoked sessions using method 1, and (**b**) method 2. (**c, d**) Decoding results as a function of population coupling for the (**c**) spontaneous and (**d**) evoked sessions using method 2 (equation 3). The green boxes circle highlight highly coupled cells with poor decodign results. Yellow boxes highlight cells with high decoding performance, but low population couplings. Method 1 and method 2 refer to equations 3 and 4, respectively. (**e**) Decoding results and (**f**) population couplings of the top 10 decoded cells in the evoked and spontaneous sessions. (**g**) Decoding results and (**h**) population couplings of the top N decoded cells (N = 5 to 30) in the in the evoked and spontaneous sessions. Solid lines and shaded regions indicate the mean and s.e.m., respectively. Population couplings are calculated among the top N decoded cells.

Discussion

In this chapter, we investigated, in collaboration with Kuzum group, the neural dynamics of the visual cortex in transgenic mice through utilizing multiple modalities, surface electrophysiological recordings and Calcium Imaging at various depths of the brain. This was made possible through the transparent graphene arrays developed by our collaborators. The complete transparency allowed for both modalities to be recorded simultaneously during the same experiment. This opens questions to be asked about the correlation between surface recording and depth calcium response.

First, Mehrdad et al. focused on decoding the average calcium activity in L1 and L2/3 using the spectral features of the surface electrophysiological recordings. They developed single RNNs and fed them of 7 different frequency bands ($\delta, \theta, \alpha, \beta, \gamma, H\gamma$, and MUA) to infer the average calcium signal. RNNs were mainly used to learn the nonlinear relationship between surface potential and depth calcium response. The decoded signal in both layers closely matched the ground truth with minimal error.

Next, to further improve the spatial resolution of the decoded network, we used GPFA to extract low-dimensional latent representation of the high dimensional population's calcium response. Mehrdad et al. trained a separate RNN configuration for each of the extracted latent modes. We then used the true and decoded latents and projected both back to high dimensional observation space. We compared the reconstruction error of the true latents vs the decoded ones and show that we can predict the activity of several neurons with high correlations, which indicates surface recordings can be used to explore the activity of neurons at depth. Lastly, we investigated the effect of population coupling on decoding performance. While coupling can play a factor in

decoding calcium activity at layer 2/3, our analysis suggests that it is not the only determining factor.

These results demonstrate that there is a huge potential in multimodal recording to be utilized to understand the dynamics of the brain more accurately. When combining different modalities that span various spatial and temporal resolutions, each modality can provide unique information that can be used to further enhance BCI technology, which could pave the way for improved clinical experiments.

Methods

Visual Stimulation

Square wave drifting grating stimuli (100% contrast, 0.04 cycles/degree, 3 cycles/sec, covering entire contralateral receptive field) were presented on an LCD monitor (30 × 38 cm) positioned 15 cm away from the right eye using Psychtoolbox (http://psychtoolbox.org/). One of 8 orientations (45° apart) was presented for 2 or 2.5 sec on each trial in pseudorandom order. Inter-stimulus-interval was 8 seconds. We presented each orientation at least 30 times in a session.

Population coupling

Two methods were used to calculate the population coupling in layers 2/3 in the spontaneous and evoked sessions [92,108]:

$$c_i = \frac{1}{\|f_i\|} \int f_i(t) \sum_{j \neq i} \left(f_j(t) - \mu_j\right) dt$$

$$c_i = corr(f_i, \frac{1}{N-1} \sum_{j \neq i}^{N} f_j)$$

In these equations, $f_i(t)$ is the calcium fluorescence change (ΔF/F) of individual cell i at timepoint t, μ_j is the average ΔF/F of cell j over time, $\|f_i\|$ is the standard deviation of ΔF/F for cell i over time, and N is the number of cells.

Electrophysiology Data Analysis

To process the electrophysiological data, Mehrdad et al. started by removing common artifacts (imaging and power line) by applying a bank of notch filters to the raw surface recordings (the filters are optimized for each channel separately). The multi-unit activity (MUA) is extracted by applying a 6th order bandpass filter from 0.5 to 4 kHz followed by common average referencing. The signals are lowpass filtered below 250 Hz using a 4th order Butterworth filter to achieve the local field potential (LFP). To further filter the signals into common low frequency bands (δ: 1–4 Hz, θ: 4–7 Hz, α: 8–15 Hz, β: 15–30 Hz, γ: 31–59 Hz, H-γ: 61–200 Hz), 6th order Butterworth bandpass signals are applied with corresponding frequency ranges.

The powers at different bands (δ, θ, α, β, γ, H-γ, MUA) were calculated by taking the square of the bandpass filtered signals and applying a 100ms Gaussian filter to reduce the noise. The power changes due to the visual stimulus were calculated by trial averaging the powers at different bands and subtracting the baseline activity (2 seconds before the stimulus onset) and the results were demonstrated using 2D spatial maps to visualize the localization of different bands. The MUA events for each channel were extracted by using the threshold crossing method (-4*std).

Low Dimensional Latent Space of Population Activity

GPFA models observations as a Gaussian model that is related to the latent variable through equation (3).

$$y_{:,t}|x_{:,t} \sim N\left(Cx_{:,t} + d, R\right)$$

Where $x_{:,t}$ represents the latent variable at timepoint t, d is the signal mean, C is the factor loading matrix, and R represents the covariance matrix. The ith latent variable x is modeled as a Gaussian process (GP) with a covariance matrix K that correlates latent variables across time points:

$$x_i \sim N(0, K_i)$$

Using the training data of calcium signal Y, we train a GPFA model that learn the parameters and infer the trajectory of the latent variable x.

$$E[X|Y] = KC'(CKC + R)^{-1}(Y - d)$$

We use the latent variables x and the inferred latent variable $\hat{x}$ from the BiLSTM model to project into calcium signal space.

$$E\left[\hat{Y}\right] = CX + d$$

$$E\left[\hat{\hat{Y}}\right] = C\hat{X} + d$$

where $\hat{Y}$ is the projected calcium signal using the originally inferred latents and $\hat{\hat{Y}}$ is the projected calcium signal using the predicted latents from the BiLSTM model. The projected calcium signals are then compared to the true calcium signals.

Reduced GPFA

To generate latent factors with distinct spatial structure, we apply orthnormalization procedure as described in [90]. We assume that the observation data is given as $Y \in \Re^{M\times T}$, while the latent variable is given as $x \in \Re^{N\times T}$. We decompose the factor loading matrix C using singular value decomposition:

$$C = UDV'$$

where $U \in \Re^{M\times N}$, $V \in \Re^{N\times N}$ each have orthonormal columns and $D \in \Re^{N\times N}$ is diagonal. Thus, we can orthonormalize the latent variable x using:

$$Cx_{:,t} = U(DV')x_{:,t} = U\,\tilde{x}_{:,t}$$

In this case, $\tilde{x}_{:,t}$ is linearly rotated version of $x_{:,t}$ and orthonormalized. This is done to intuitively visualize the trajectories extracted by GPFA (figure 3.10).

Acknowledgments

Chapter 3, in part, a reprint of Mehrdad Ramezani, Jeong-Hoon Kim, Xin Liu, Chi Ren, Abdullah Alothman, Chawina De-Eknamkul, Madison N. Wilson, Ertugrul Cubukcu, Vikash Gilja, Takaki Komiyama, and Duygu Kuzum, *" Cellular Calcium Activity at Depth Predicted from Surface Potential Recordings using Ultra-high Density Transparent Graphene Arrays*". Nature Nanotechnology, 2023.

We thank members of the Kuzum, Komiyama, and Cubukcu labs for helpful discussions. This research was supported by grants from the ONR Young Investigator Award (N00014161253), NSF (ECCS-2024776, ECCS-1752241 and ECCS-1734940) and NIH (R21 EY029466 and R21 EB026180 and DP2 EB030992) to D.K., and grants from NIH (R01 NS091010A, R01 EY025349, R01 DC014690, R21 NS109722, and P30 EY022589), NSF (1940202), Pew Charitable Trusts, and David and Lucile Packard Foundation to T.K. Fabrication of the electrodes was performed at the San Diego Nanotechnology Infrastructure (SDNI) of UCSD, a member of the National Nanotechnology Coordinated Infrastructure, which is supported by the National Science Foundation (Grant ECCS-1542148).

Author Contributions

This work was conceived by M.R., J.-H.K., and D.K. Microelectrode array fabrication was performed by J.-H.K and the characterization of arrays was performed by J.-H.K, C.D.-E., and M.W. All animal experiments were performed by C.R., X.L. and M.R. and analyzed by M.R. with contributions from J.-H.K., A.A., V.G., and D K. The manuscript was written by M.R., J.-H.K., and D.K. and edited by all authors.

References

[1] J. A. Frank, M.-J. Antonini, and P. Anikeeva, "Next-generation interfaces for studying neural function," *Nature biotechnology,* vol. 37, no. 9, pp. 1013-1023, 2019.

[2] T. A. Machado, I. V. Kauvar, and K. Deisseroth, "Multiregion neuronal activity: the forest and the trees," *Nature Reviews Neuroscience,* vol. 23, no. 11, pp. 683-704, 2022.

[3] H.-a. Tseng, R. E. Kohman, and X. Han, "Optogenetics and Electrophysiology," in *Basic Electrophysiological Methods*, E. Covey and M. Carter Eds.: Oxford University Press, 2015, sec. Oxford Academic, p. 0.

[4] N. K. Logothetis, O. Eschenko, Y. Murayama, M. Augath, T. Steudel, H. Evrard, M. Besserve, and A. Oeltermann, "Hippocampal–cortical interaction during periods of subcortical silence," *Nature,* vol. 491, no. 7425, pp. 547-553, 2012.

[5] V. Gradinaru, M. Mogri, K. R. Thompson, J. M. Henderson, and K. Deisseroth, "Optical deconstruction of parkinsonian neural circuitry," *science,* vol. 324, no. 5925, pp. 354-359, 2009.

[6] A. Fernández-Ruiz, A. Oliva, M. Soula, F. Rocha-Almeida, G. A. Nagy, G. Martin-Vazquez, and G. Buzsáki, "Gamma rhythm communication between entorhinal cortex and dentate gyrus neuronal assemblies," *Science,* vol. 372, no. 6537, p. eabf3119, 2021.

[7] R. Scheeringa, P. J. Koopmans, T. van Mourik, O. Jensen, and D. G. Norris, "The relationship between oscillatory EEG activity and the laminar-specific BOLD signal," *Proceedings of the National Academy of Sciences,* vol. 113, no. 24, pp. 6761-6766, 2016.

[8] D. Sabatinelli, A. Keil, D. W. Frank, and P. J. Lang, "Emotional perception: correspondence of early and late event-related potentials with cortical and subcortical functional MRI," *Biological psychology,* vol. 92, no. 3, pp. 513-519, 2013.

[9] R. Scheeringa and P. Fries, "Cortical layers, rhythms and BOLD signals," *NeuroImage,* vol. 197, pp. 689-698, 2019.

[10] M. K. Kim, J. C. Leong, Y. Jo, G. Kook, and H. J. Lee, "Multimodal Neural Probes with Small Form Factor Based on Dual-Side Fabrication," *Advanced Materials Technologies,* vol. 8, no. 2, p. 2200692, 2023.

[11] X.-a. Bi, X. Hu, Y. Xie, and H. Wu, "A novel CERNNE approach for predicting Parkinson's Disease-associated genes and brain regions based on multimodal imaging genetics data," *Medical Image Analysis,* vol. 67, p. 101830, 2021.

[12] D. Zhang, Y. Wang, L. Zhou, H. Yuan, D. Shen, and A. s. D. N. Initiative, "Multimodal classification of Alzheimer's disease and mild cognitive impairment," *Neuroimage,* vol. 55, no. 3, pp. 856-867, 2011.

[13] A. Vittala, N. Murphy, A. Maheshwari, and V. Krishnan, "Understanding cortical dysfunction in schizophrenia with TMS/EEG," *Frontiers in Neuroscience,* vol. 14, p. 554, 2020.

[14] X. Li, S. Honda, S. Nakajima, M. Wada, K. Yoshida, Z. J. Daskalakis, M. Mimura, and Y. Noda, "TMS-EEG research to elucidate the pathophysiological neural bases in patients with schizophrenia: a systematic review," *Journal of Personalized Medicine,* vol. 11, no. 5, p. 388, 2021.

[15] R. Zöllner, A.-F. Hübener, U. Dannlowski, T. Kircher, J. Sommer, and M. Zavorotnyy, "Theta-Burst Stimulation for Auditory-Verbal Hallucination in Very-Late-Onset

Schizophrenia-Like Psychosis—A Functional Magnetic Resonance Imaging Case Study," *Frontiers in psychiatry,* vol. 11, p. 294, 2020.

[16] R. D. Webler, C. Hamady, C. Molnar, K. Johnson, L. Bonilha, B. S. Anderson, C. Bruin, D. E. Bohning, M. S. George, and Z. Nahas, "Decreased interhemispheric connectivity and increased cortical excitability in unmedicated schizophrenia: a prefrontal interleaved TMS fMRI study," *Brain Stimulation,* vol. 13, no. 5, pp. 1467-1475, 2020.

[17] M. S. Cetin, J. M. Houck, B. Rashid, O. Agacoglu, J. M. Stephen, J. Sui, J. Canive, A. Mayer, C. Aine, and J. R. Bustillo, "Multimodal classification of schizophrenia patients with MEG and fMRI data using static and dynamic connectivity measures," *Frontiers in neuroscience,* vol. 10, p. 466, 2016.

[18] S. Fazli, J. Mehnert, J. Steinbrink, G. Curio, A. Villringer, K.-R. Müller, and B. Blankertz, "Enhanced performance by a hybrid NIRS–EEG brain computer interface," *Neuroimage,* vol. 59, no. 1, pp. 519-529, 2012.

[19] M. J. Khan and K.-S. Hong, "Hybrid EEG–fNIRS-based eight-command decoding for BCI: application to quadcopter control," *Frontiers in neurorobotics,* vol. 11, p. 6, 2017.

[20] A. M. Chiarelli, P. Croce, A. Merla, and F. Zappasodi, "Deep learning for hybrid EEG-fNIRS brain–computer interface: application to motor imagery classification," *Journal of neural engineering,* vol. 15, no. 3, p. 036028, 2018.

[21] H.-L. Halme and L. Parkkonen, "Across-subject offline decoding of motor imagery from MEG and EEG," *Scientific reports,* vol. 8, no. 1, pp. 1-12, 2018.

[22] X. Liu, C. Ren, Z. Huang, M. Wilson, J.-H. Kim, Y. Lu, M. Ramezani, T. Komiyama, and D. Kuzum, "Decoding of cortex-wide brain activity from local recordings of neural potentials," *Journal of neural engineering,* vol. 18, no. 6, p. 066009, 2021.

[23] S. Q. Lima, T. Hromádka, P. Znamenskiy, and A. M. Zador, "PINP: a new method of tagging neuronal populations for identification during in vivo electrophysiological recording," *PloS one,* vol. 4, no. 7, p. e6099, 2009.

[24] J. H. Siegle, X. Jia, S. Durand, S. Gale, C. Bennett, N. Graddis, G. Heller, T. K. Ramirez, H. Choi, and J. A. Luviano, "Survey of spiking in the mouse visual system reveals functional hierarchy," *Nature,* vol. 592, no. 7852, pp. 86-92, 2021.

[25] D. Kuzum, H. Takano, E. Shim, J. C. Reed, H. Juul, A. G. Richardson, J. De Vries, H. Bink, M. A. Dichter, and T. H. Lucas, "Transparent and flexible low noise graphene electrodes for simultaneous electrophysiology and neuroimaging," *Nature communications,* vol. 5, no. 1, p. 5259, 2014.

[26] M. Thunemann, Y. Lu, X. Liu, K. Kilic, M. Desjardins, M. Vandenberghe, S. Sadegh, P. A. Saisan, Q. Cheng, K. L. Weldy, H. Lyu, S. Djurovic, O. A. Andreassen, A. M. Dale, A.

Devor, and D. Kuzum, "Deep 2-photon imaging and artifact-free optogenetics through transparent graphene microelectrode arrays," *Nat Commun,* vol. 9, no. 1, p. 2035, May 23 2018, doi: 10.1038/s41467-018-04457-5.

[27] N. Driscoll, R. E. Rosch, B. B. Murphy, A. Ashourvan, R. Vishnubhotla, O. O. Dickens, A. T. C. Johnson, K. A. Davis, B. Litt, D. S. Bassett, H. Takano, and F. Vitale, "Multimodal in vivo recording using transparent graphene microelectrodes illuminates spatiotemporal seizure dynamics at the microscale," *Commun Biol,* vol. 4, no. 1, p. 136, Jan 29 2021, doi: 10.1038/s42003-021-01670-9.

[28] D.-W. Park, A. A. Schendel, S. Mikael, S. K. Brodnick, T. J. Richner, J. P. Ness, M. R. Hayat, F. Atry, S. T. Frye, and R. Pashaie, "Graphene-based carbon-layered electrode array technology for neural imaging and optogenetic applications," *Nature communications,* vol. 5, no. 1, p. 5258, 2014.

[29] M. N. Wilson, M. Thunemann, X. Liu, Y. Lu, F. Puppo, J. W. Adams, J.-H. Kim, M. Ramezani, D. P. Pizzo, and S. Djurovic, "Multimodal monitoring of human cortical organoids implanted in mice reveal functional connection with visual cortex," *Nature Communications,* vol. 13, no. 1, p. 7945, 2022.

[30] D. Akinwande, C. J. Brennan, J. S. Bunch, P. Egberts, J. R. Felts, H. Gao, R. Huang, J.-S. Kim, T. Li, and Y. Li, "A review on mechanics and mechanical properties of 2D materials—Graphene and beyond," *Extreme Mechanics Letters,* vol. 13, pp. 42-77, 2017.

[31] D. Kireev, K. Sel, B. Ibrahim, N. Kumar, A. Akbari, R. Jafari, and D. Akinwande, "Continuous cuffless monitoring of arterial blood pressure via graphene bioimpedance tattoos," *Nature Nanotechnology,* vol. 17, no. 8, pp. 864-870, 2022.

[32] K. Kostarelos, M. Vincent, C. Hebert, and J. A. Garrido, "Graphene in the design and engineering of next-generation neural interfaces," *Advanced Materials,* vol. 29, no. 42, p. 1700909, 2017.

[33] D. Sahni, A. Jea, J. A. Mata, D. C. Marcano, A. Sivaganesan, J. M. Berlin, C. E. Tatsui, Z. Sun, T. G. Luerssen, and S. Meng, "Biocompatibility of pristine graphene for neuronal interface," *Journal of Neurosurgery: Pediatrics,* vol. 11, no. 5, pp. 575-583, 2013.

[34] A. Bonaccini Calia, E. Masvidal-Codina, T. M. Smith, N. Schäfer, D. Rathore, E. Rodríguez-Lucas, X. Illa, J. M. De la Cruz, E. Del Corro, and E. Prats-Alfonso, "Full-bandwidth electrophysiology of seizures and epileptiform activity enabled by flexible graphene microtransistor depth neural probes," *Nature Nanotechnology,* vol. 17, no. 3, pp. 301-309, 2022.

[35] X. Liu, S. Terada, M. Ramezani, J.-H. Kim, Y. Lu, A. Grosmark, A. Losonczy, and D. Kuzum, "E-Cannula reveals anatomical diversity in sharp-wave ripples as a driver for the recruitment of distinct hippocampal assemblies," *Cell Reports,* vol. 41, no. 1, p. 111453, 2022.

[36] D. Ding, Y. Lu, R. Zhao, X. Liu, C. De-Eknamkul, C. Ren, A. Mehrsa, T. Komiyama, and D. Kuzum, "Evaluation of durability of transparent graphene electrodes fabricated on different flexible substrates for chronic in vivo experiments," *IEEE Transactions on Biomedical Engineering,* vol. 67, no. 11, pp. 3203-3210, 2020.

[37] N. Kunori and I. Takashima, "A transparent epidural electrode array for use in conjunction with optical imaging," *Journal of neuroscience methods,* vol. 251, pp. 130-137, 2015.

[38] P. Ledochowitsch, A. Yazdan-Shahmorad, K. Bouchard, C. Diaz-Botia, T. Hanson, J.-W. He, B. Seybold, E. Olivero, E. Phillips, and T. Blanche, "Strategies for optical control and simultaneous electrical readout of extended cortical circuits," *Journal of neuroscience methods,* vol. 256, pp. 220-231, 2015.

[39] J. Zhang, X. Liu, W. Xu, W. Luo, M. Li, F. Chu, L. Xu, A. Cao, J. Guan, and S. Tang, "Stretchable transparent electrode arrays for simultaneous electrical and optical interrogation of neural circuits in vivo," *Nano letters,* vol. 18, no. 5, pp. 2903-2911, 2018.

[40] K. J. Seo, Y. Qiang, I. Bilgin, S. Kar, C. Vinegoni, R. Weissleder, and H. Fang, "Transparent electrophysiology microelectrodes and interconnects from metal nanomesh," *ACS nano,* vol. 11, no. 4, pp. 4365-4372, 2017.

[41] Z. Chen, N. Boyajian, Z. Lin, R. T. Yin, S. N. Obaid, J. Tian, J. A. Brennan, S. W. Chen, A. N. Miniovich, and L. Lin, "Flexible and transparent metal nanowire microelectrode arrays and interconnects for electrophysiology, optogenetics, and optical mapping," *Advanced Materials Technologies,* vol. 6, no. 7, p. 2100225, 2021.

[42] S. N. Obaid, R. T. Yin, J. Tian, Z. Chen, S. W. Chen, K. B. Lee, N. Boyajian, A. N. Miniovich, I. R. Efimov, and L. Lu, "Multifunctional Flexible Biointerfaces for Simultaneous Colocalized Optophysiology and Electrophysiology," *Advanced Functional Materials,* vol. 30, no. 24, p. 1910027, 2020.

[43] J. W. Seo, K. Kim, K. W. Seo, M. K. Kim, S. Jeong, H. Kim, J. W. Ghim, J. H. Lee, N. Choi, J. Y. Lee, and H. J. Lee, "Artifact-Free 2D Mapping of Neural Activity In Vivo through Transparent Gold Nanonetwork Array," *Advanced Functional Materials,* vol. 30, no. 34, 2020, doi: 10.1002/adfm.202000896.

[44] Y. Qiang, P. Artoni, K. J. Seo, S. Culaclii, V. Hogan, X. Zhao, Y. Zhong, X. Han, P.-M. Wang, and Y.-K. Lo, "Transparent arrays of bilayer-nanomesh microelectrodes for simultaneous electrophysiology and two-photon imaging in the brain," *Science advances,* vol. 4, no. 9, p. eaat0626, 2018.

[45] Y. U. Cho, J. Y. Lee, U. J. Jeong, S. H. Park, S. L. Lim, K. Y. Kim, J. W. Jang, J. H. Park, H. W. Kim, and H. Shin, "Ultra-low cost, facile fabrication of transparent neural electrode array for electrocorticography with photoelectric artifact-free optogenetics," *Advanced Functional Materials,* vol. 32, no. 10, p. 2105568, 2022.

[46] W. Yang, Y. Gong, C.-Y. Yao, M. Shrestha, Y. Jia, Z. Qiu, Q. H. Fan, A. Weber, and W. Li, "A fully transparent, flexible PEDOT: PSS–ITO–Ag–ITO based microelectrode array for ECoG recording," *Lab on a Chip,* vol. 21, no. 6, pp. 1096-1108, 2021.

[47] K. Lim, S. Jung, J.-K. Kim, J.-W. Kang, J.-H. Kim, S.-H. Choa, and D.-G. Kim, "Flexible PEDOT: PSS/ITO hybrid transparent conducting electrode for organic photovoltaics," *Solar energy materials and solar cells,* vol. 115, pp. 71-78, 2013.

[48] D.-P. Tran, H.-I. Lu, and C.-K. Lin, "Conductive characteristics of indium tin oxide thin film on polymeric substrate under long-term static deformation," *Coatings,* vol. 8, no. 6, p. 212, 2018.

[49] S. F. Hansen and A. Lennquist, "Carbon nanotubes added to the SIN List as a nanomaterial of Very High Concern," *Nature Nanotechnology,* vol. 15, no. 1, pp. 3-4, 2020.

[50] Y. Sakamoto, M. Hojo, Y. Kosugi, K. Watanabe, A. Hirose, A. Inomata, T. Suzuki, and D. Nakae, "Comparative study for carcinogenicity of 7 different multi-wall carbon nanotubes with different physicochemical characteristics by a single intraperitoneal injection in male Fischer 344 rats," *The Journal of toxicological sciences,* vol. 43, no. 10, pp. 587-600, 2018.

[51] J. P. Neto, A. Costa, J. Vaz Pinto, A. Marques-Smith, J. C. Costa, R. Martins, E. Fortunato, A. R. Kampff, and P. Barquinha, "Transparent and flexible electrocorticography electrode arrays based on silver nanowire networks for neural recordings," *ACS Applied Nano Materials,* vol. 4, no. 6, pp. 5737-5747, 2021.

[52] X. T. Cui and D. D. Zhou, "Poly (3, 4-ethylenedioxythiophene) for chronic neural stimulation," *IEEE Transactions on Neural Systems and Rehabilitation Engineering,* vol. 15, no. 4, pp. 502-508, 2007.

[53] E. Masvidal-Codina, X. Illa, M. Dasilva, A. B. Calia, T. Dragojević, E. E. Vidal-Rosas, E. Prats-Alfonso, J. Martínez-Aguilar, J. M. De la Cruz, and R. Garcia-Cortadella, "High-resolution mapping of infraslow cortical brain activity enabled by graphene microtransistors," *Nature materials,* vol. 18, no. 3, pp. 280-288, 2019.

[54] R. Garcia-Cortadella, G. Schwesig, C. Jeschke, X. Illa, A. L. Gray, S. Savage, E. Stamatidou, I. Schiessl, E. Masvidal-Codina, and K. Kostarelos, "Graphene active sensor arrays for long-term and wireless mapping of wide frequency band epicortical brain activity," *Nature communications,* vol. 12, no. 1, p. 211, 2021.

[55] D. Kuzum, H. Takano, E. Shim, J. C. Reed, H. Juul, A. G. Richardson, J. De Vries, H. Bink, M. A. Dichter, and T. H. Lucas, "Transparent and flexible low noise graphene electrodes for simultaneous electrophysiology and neuroimaging," *Nature communications,* vol. 5, no. 1, pp. 1-10, 2014.

[56] D.-W. Park, J. P. Ness, S. K. Brodnick, C. Esquibel, J. Novello, F. Atry, D.-H. Baek, H. Kim, J. Bong, and K. I. Swanson, "Electrical neural stimulation and simultaneous in vivo

monitoring with transparent graphene electrode arrays implanted in GCaMP6f mice," *ACS nano,* vol. 12, no. 1, pp. 148-157, 2018.

[57] Y. Lu, X. Liu, R. Hattori, C. Ren, X. Zhang, T. Komiyama, and D. Kuzum, "Ultralow impedance graphene microelectrodes with high optical transparency for simultaneous deep two-photon imaging in transgenic mice," *Advanced functional materials,* vol. 28, no. 31, p. 1800002, 2018.

[58] M. Thunemann, Y. Lu, X. Liu, K. Kılıç, M. Desjardins, M. Vandenberghe, S. Sadegh, P. A. Saisan, Q. Cheng, and K. L. Weldy, "Deep 2-photon imaging and artifact-free optogenetics through transparent graphene microelectrode arrays," *Nature communications,* vol. 9, no. 1, pp. 1-12, 2018.

[59] X. Liu, C. Ren, Y. Lu, R. Hattori, Y. Shi, R. Zhao, D. Ding, T. Komiyama, and D. Kuzum, "Decoding ECoG High Gamma Power from Cellular Calcium Response using Transparent Graphene Microelectrodes," in *2019 9th International IEEE/EMBS Conference on Neural Engineering (NER)*, 2019: IEEE, pp. 710-713.

[60] N. Driscoll, R. E. Rosch, B. B. Murphy, A. Ashourvan, R. Vishnubhotla, O. O. Dickens, A. Johnson, K. A. Davis, B. Litt, and D. S. Bassett, "Multimodal in vivo recording using transparent graphene microelectrodes illuminates spatiotemporal seizure dynamics at the microscale," *Communications biology,* vol. 4, no. 1, pp. 1-14, 2021.

[61] P. Ledochowitsch, E. Olivero, T. Blanche, and M. M. Maharbiz, "A transparent μECoG array for simultaneous recording and optogenetic stimulation," in *2011 Annual International Conference of the IEEE Engineering in Medicine and Biology Society*, 2011: IEEE, pp. 2937-2940.

[62] K. Y. Kwon, B. Sirowatka, A. Weber, and W. Li, "Opto-μECoG array: A hybrid neural interface with transparent μECoG electrode array and integrated LEDs for optogenetics," *IEEE transactions on biomedical circuits and systems,* vol. 7, no. 5, pp. 593-600, 2013.

[63] H. Toda, T. Suzuki, H. Sawahata, K. Majima, Y. Kamitani, and I. Hasegawa, "Simultaneous recording of ECoG and intracortical neuronal activity using a flexible multichannel electrode-mesh in visual cortex," *Neuroimage,* vol. 54, no. 1, pp. 203-212, 2011.

[64] T. Araki, F. Yoshida, T. Uemura, Y. Noda, S. Yoshimoto, T. Kaiju, T. Suzuki, H. Hamanaka, K. Baba, and H. Hayakawa, "Long-term implantable, flexible, and transparent neural interface based on Ag/Au core–shell nanowires," *Advanced Healthcare Materials,* vol. 8, no. 10, p. 1900130, 2019.

[65] P. Kshirsagar, S. Dickreuter, M. Mierzejewski, C. J. Burkhardt, T. Chassé, M. Fleischer, and P. D. Jones, "Transparent Graphene/PEDOT: PSS microelectrodes for electro-and optophysiology," *Advanced Materials Technologies,* vol. 4, no. 1, p. 1800318, 2019.

[66] X. Liu, Y. Lu, E. Iseri, Y. Shi, and D. Kuzum, "A compact closed-loop optogenetics system based on artifact-free transparent graphene electrodes," *Frontiers in neuroscience,* vol. 12, p. 132, 2018.

[67] Y. Lu, X. Liu, and D. Kuzum, "Graphene-based neurotechnologies for advanced neural interfaces," *Current Opinion in Biomedical Engineering,* vol. 6, pp. 138-147, 2018.

[68] G. H. Kim, N. Y. Kim, Z. Lee, S. D. Jung, and J.-O. Lee, "A high-performance transparent graphene/vertically aligned carbon nanotube (VACNT) hybrid electrode for neural interfacing," *RSC advances,* vol. 7, no. 6, pp. 3273-3281, 2017.

[69] W. Wei and X. Wang, "Graphene-based electrode materials for neural activity detection," *Materials,* vol. 14, no. 20, p. 6170, 2021.

[70] M. N. Wilson, M. Thunemann, F. Puppo, E. Martin, R. Blanch, F. H. Gage, A. R. Muotri, A. Devor, and D. Kuzum, "Investigation of functional integration of cortical organoids transplanted in vivo towards future neural prosthetics applications," in *2023 11th International IEEE/EMBS Conference on Neural Engineering (NER)*, 2023: IEEE, pp. 1-4.

[71] V. Viswam, M. E. J. Obien, F. Franke, U. Frey, and A. Hierlemann, "Optimal Electrode Size for Multi-Scale Extracellular-Potential Recording From Neuronal Assemblies," *Front Neurosci,* vol. 13, p. 385, 2019, doi: 10.3389/fnins.2019.00385.

[72] N. Rogers, J. Hermiz, M. Ganji, E. Kaestner, K. Kilic, L. Hossain, M. Thunemann, D. R. Cleary, B. S. Carter, D. Barba, A. Devor, E. Halgren, S. A. Dayeh, and V. Gilja, "Correlation Structure in Micro-ECoG Recordings is Described by Spatially Coherent Components," *PLoS Comput Biol,* vol. 15, no. 2, p. e1006769, Feb 2019, doi: 10.1371/journal.pcbi.1006769.

[73] K. D. Harris, R. Q. Quiroga, J. Freeman, and S. L. Smith, "Improving data quality in neuronal population recordings," *Nat Neurosci,* vol. 19, no. 9, pp. 1165-74, Aug 26 2016, doi: 10.1038/nn.4365.

[74] J. Xia, F. Chen, J. Li, and N. Tao, "Measurement of the quantum capacitance of graphene," *Nat Nanotechnol,* vol. 4, no. 8, pp. 505-9, Aug 2009, doi: 10.1038/nnano.2009.177.

[75] D. H. Hubel and T. N. Wiesel, "Receptive fields, binocular interaction and functional architecture in the cat's visual cortex," *The Journal of physiology,* vol. 160, no. 1, p. 106, 1962.

[76] D. H. Hubel and T. N. Wiesel, "Receptive fields and functional architecture of monkey striate cortex," *The Journal of physiology,* vol. 195, no. 1, pp. 215-243, 1968.

[77] A. Kohn and M. A. Smith, "Stimulus dependence of neuronal correlation in primary visual cortex of the macaque," *Journal of Neuroscience,* vol. 25, no. 14, pp. 3661-3673, 2005.

[78] K. Ohki, S. Chung, Y. H. Ch'ng, P. Kara, and R. C. Reid, "Functional imaging with cellular resolution reveals precise micro-architecture in visual cortex," *Nature,* vol. 433, no. 7026, pp. 597-603, 2005.

[79] Y. Zhang, M. Rózsa, Y. Liang, D. Bushey, Z. Wei, J. Zheng, D. Reep, G. J. Broussard, A. Tsang, and G. Tsegaye, "Fast and sensitive GCaMP calcium indicators for imaging neural populations," *Nature,* vol. 615, no. 7954, pp. 884-891, 2023.

[80] M. F. Tang, E. Kheradpezhouh, C. C. Lee, J. E. Dickinson, J. B. Mattingley, and E. Arabzadeh, "Expectation violations enhance neuronal encoding of sensory information in mouse primary visual cortex," *Nature Communications,* vol. 14, no. 1, p. 1196, 2023.

[81] S. Das, P. Sudhagar, E. Ito, D.-y. Lee, S. Nagarajan, S. Y. Lee, Y. S. Kang, and W. Choi, "Effect of HNO 3 functionalization on large scale graphene for enhanced tri-iodide reduction in dye-sensitized solar cells," *Journal of Materials Chemistry,* vol. 22, no. 38, pp. 20490-20497, 2012.

[82] X. Liu, C. Ren, Y. Lu, Y. Liu, J. H. Kim, S. Leutgeb, T. Komiyama, and D. Kuzum, "Multimodal neural recordings with Neuro-FITM uncover diverse patterns of cortical-hippocampal interactions," *Nat Neurosci,* vol. 24, no. 6, pp. 886-896, Jun 2021, doi: 10.1038/s41593-021-00841-5.

[83] J. B. Wekselblatt, E. D. Flister, D. M. Piscopo, and C. M. Niell, "Large-scale imaging of cortical dynamics during sensory perception and behavior," *J Neurophysiol,* vol. 115, no. 6, pp. 2852-66, Jun 1 2016, doi: 10.1152/jn.01056.2015.

[84] M. Mayford, M. E. Bach, Y.-Y. Huang, L. Wang, R. D. Hawkins, and E. R. Kandel, "Control of memory formation through regulated expression of a CaMKII transgene," *Science,* vol. 274, no. 5293, pp. 1678-1683, 1996.

[85] S. Leski, H. Linden, T. Tetzlaff, K. H. Pettersen, and G. T. Einevoll, "Frequency dependence of signal power and spatial reach of the local field potential," *PLoS Comput Biol,* vol. 9, no. 7, p. e1003137, 2013, doi: 10.1371/journal.pcbi.1003137.

[86] J. C. Myers, E. H. Smith, M. Leszczynski, J. O'Sullivan, M. J. Yates, G. McKhann, N. Mesgarani, C. Schroeder, C. Schevon, and S. A. Sheth, "The Spatial Reach of Neuronal Coherence and Spike-Field Coupling across the Human Neocortex," *J Neurosci,* vol. 42, no. 32, pp. 6285-6294, Aug 10 2022, doi: 10.1523/JNEUROSCI.0050-22.2022.

[87] S. Kellis, L. Sorensen, F. Darvas, C. Sayres, K. O'Neill, 3rd, R. B. Brown, P. House, J. Ojemann, and B. Greger, "Multi-scale analysis of neural activity in humans: Implications for micro-scale electrocorticography," *Clin Neurophysiol,* vol. 127, no. 1, pp. 591-601, Jan 2016, doi: 10.1016/j.clinph.2015.06.002.

[88] J. A. Gallego, M. G. Perich, L. E. Miller, and S. A. Solla, "Neural manifolds for the control of movement," *Neuron,* vol. 94, no. 5, pp. 978-984, 2017.

[89] G. F. Elsayed, A. H. Lara, M. T. Kaufman, M. M. Churchland, and J. P. Cunningham, "Reorganization between preparatory and movement population responses in motor cortex," *Nature communications,* vol. 7, no. 1, p. 13239, 2016.

[90] B. M. Yu, J. P. Cunningham, G. Santhanam, S. Ryu, K. V. Shenoy, and M. Sahani, "Gaussian-process factor analysis for low-dimensional single-trial analysis of neural population activity," *Advances in neural information processing systems,* vol. 21, 2008.

[91] C. Stringer, M. Pachitariu, N. Steinmetz, C. B. Reddy, M. Carandini, and K. D. Harris, "Spontaneous behaviors drive multidimensional, brainwide activity," *Science,* vol. 364, no. 6437, p. eaav7893, 2019.

[92] M. Okun, N. A. Steinmetz, L. Cossell, M. F. Iacaruso, H. Ko, P. Barthó, T. Moore, S. B. Hofer, T. D. Mrsic-Flogel, and M. Carandini, "Diverse coupling of neurons to populations in sensory cortex," *Nature,* vol. 521, no. 7553, pp. 511-515, 2015.

[93] C. Stringer, M. Pachitariu, N. Steinmetz, M. Carandini, and K. D. Harris, "High-dimensional geometry of population responses in visual cortex," *Nature,* vol. 571, no. 7765, pp. 361-365, 2019.

[94] Y. U. Cho, S. L. Lim, J.-H. Hong, and K. J. Yu, "Transparent neural implantable devices: A comprehensive review of challenges and progress," *npj Flexible Electronics,* vol. 6, no. 1, p. 53, 2022.

[95] F.-B. Vialatte, M. Maurice, J. Dauwels, and A. Cichocki, "Steady-state visually evoked potentials: focus on essential paradigms and future perspectives," *Progress in neurobiology,* vol. 90, no. 4, pp. 418-438, 2010.

[96] B. H. Jansen and V. G. Rit, "Electroencephalogram and visual evoked potential generation in a mathematical model of coupled cortical columns," *Biological cybernetics,* vol. 73, no. 4, pp. 357-366, 1995.

[97] V. Porciatti, T. Pizzorusso, and L. Maffei, "The visual physiology of the wild type mouse determined with pattern VEPs," *Vision research,* vol. 39, no. 18, pp. 3071-3081, 1999.

[98] H. Dana, Y. Sun, B. Mohar, B. K. Hulse, A. M. Kerlin, J. P. Hasseman, G. Tsegaye, A. Tsang, A. Wong, and R. Patel, "High-performance calcium sensors for imaging activity in neuronal populations and microcompartments," *Nature methods,* vol. 16, no. 7, pp. 649-657, 2019.

[99] Y. You, A. Klistorner, and S. L. Graham, "Visual evoked potential recording in rodents," *Stimulation and Inhibition of Neurons,* pp. 275-285, 2013.

[100] W. Ridder Iii and S. Nusinowitz, "The visual evoked potential in the mouse—origins and response characteristics," *Vision research,* vol. 46, no. 6-7, pp. 902-913, 2006.

[101] S. Marenna, V. Castoldi, R. d'Isa, C. Marco, G. Comi, and L. Leocani, "Semi-invasive and non-invasive recording of visual evoked potentials in mice," *Documenta Ophthalmologica,* vol. 138, pp. 169-179, 2019.

[102] G. Buzsáki, C. A. Anastassiou, and C. Koch, "The origin of extracellular fields and currents—EEG, ECoG, LFP and spikes," *Nature reviews neuroscience,* vol. 13, no. 6, pp. 407-420, 2012.

[103] H. Bink, M. Sedigh-Sarvestani, I. Fernandez-Lamo, L. Kini, H. Ung, D. Kuzum, F. Vitale, B. Litt, and D. Contreras, "Spatiotemporal evolution of focal epileptiform activity from surface and laminar field recordings in cat neocortex," *Journal of Neurophysiology,* vol. 119, no. 6, pp. 2068-2081, 2018.

[104] Y. Wang, Y. Zheng, X. Xu, E. Dubuisson, Q. Bao, J. Lu, and K. P. Loh, "Electrochemical delamination of CVD-grown graphene film: toward the recyclable use of copper catalyst," *ACS nano,* vol. 5, no. 12, pp. 9927-9933, 2011.

[105] G. Brug, A. L. van den Eeden, M. Sluyters-Rehbach, and J. H. Sluyters, "The analysis of electrode impedances complicated by the presence of a constant phase element," *Journal of electroanalytical chemistry and interfacial electrochemistry,* vol. 176, no. 1-2, pp. 275-295, 1984.

[106] A. Mitani and T. Komiyama, "Real-Time Processing of Two-Photon Calcium Imaging Data Including Lateral Motion Artifact Correction," *Front Neuroinform,* vol. 12, p. 98, 2018, doi: 10.3389/fninf.2018.00098.

[107] M. Pachitariu, C. Stringer, M. Dipoppa, S. Schröder, L. F. Rossi, H. Dalgleish, M. Carandini, and K. D. Harris, 2017, doi: 10.1101/061507.

[108] Y. Sweeney and C. Clopath, "Population coupling predicts the plasticity of stimulus responses in cortical circuits," *Elife,* vol. 9, p. e56053, 2020.

Supplementary Figures

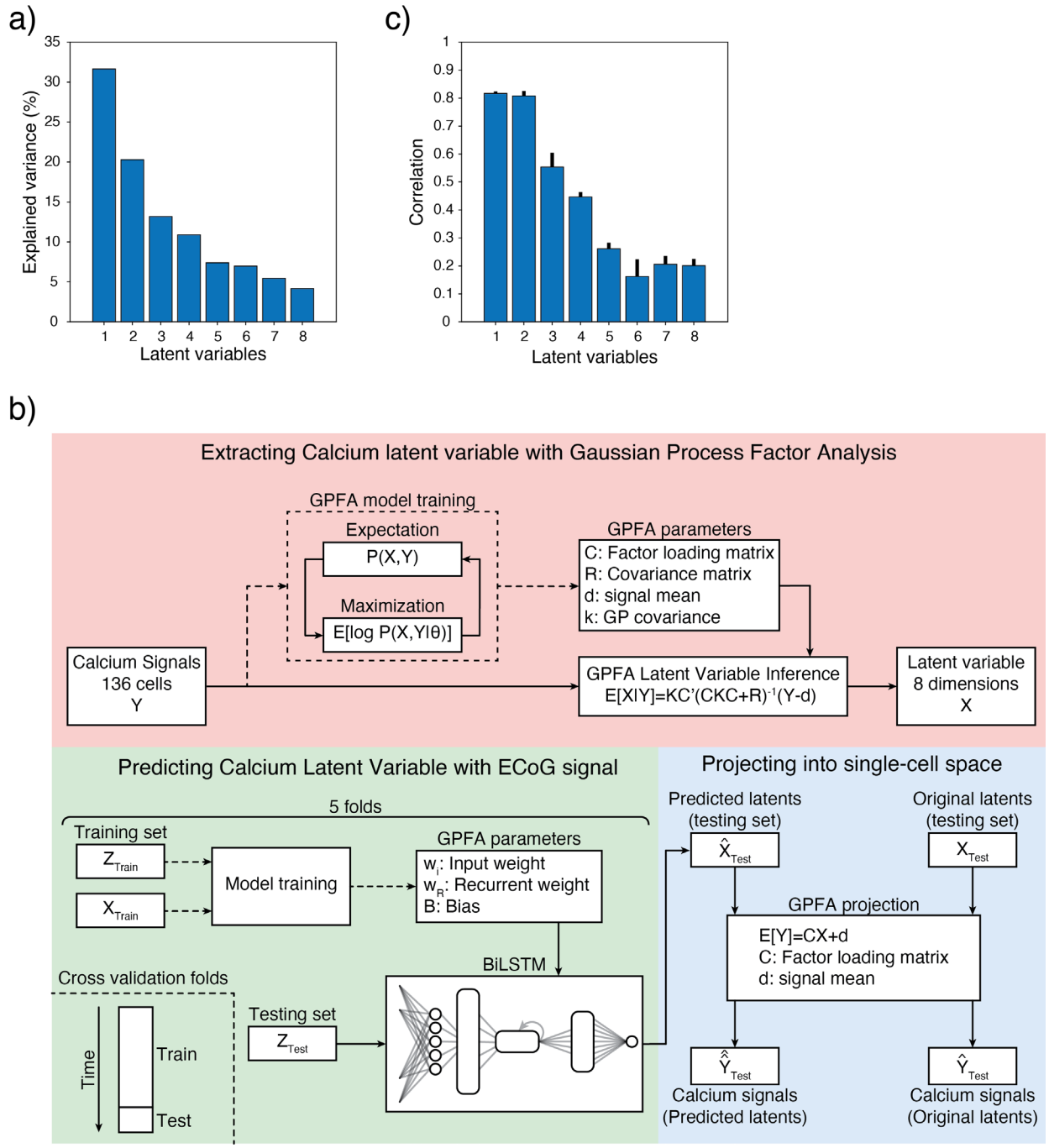

Figure 3.6 **Extracting low dimensional latent space.**

(**a**) Explained variance of the high dimensional calcium signal by each latent variable. (**b**) Decoding results of the eight latent variables average over five folds. Black lines indicate the s.e.m. (**c**) Detailed description of the model used for single-cell decoding of calcium signals.

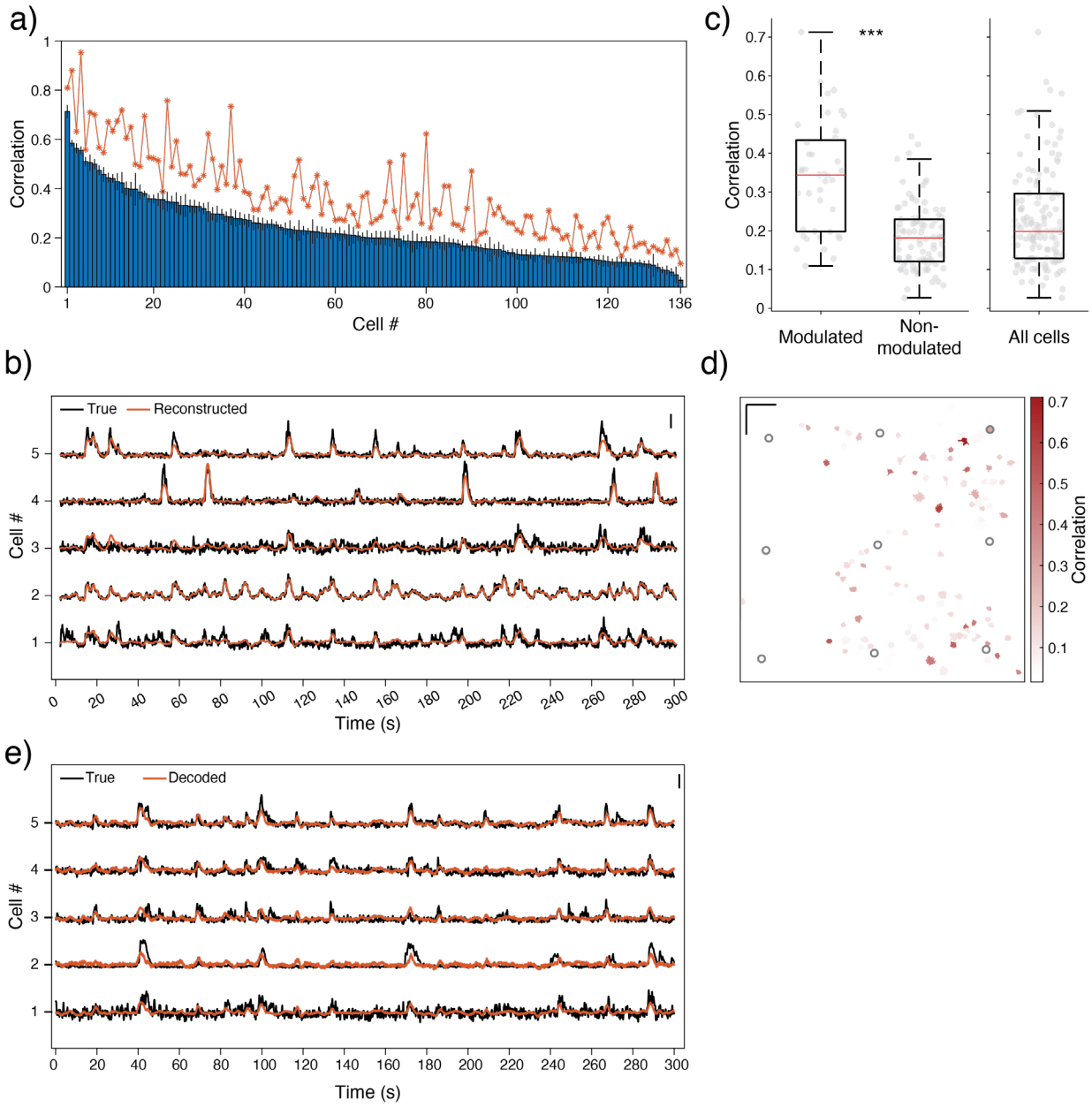

Figure 3.7 **Decoding calcium signals at single-cell resolution.**

(a) The correlation between reconstructed and original ΔF/F signals of all 136 single cells is shown using BiLSTM decoded latents (blue bars) and true latents that we inferred from GPFA (orange). (b) Examples for reconstructed single-cell activities using true latent variables (orange) vs ground truth ΔF/F (black). (c) Decoding results for the modulated (n=40) vs non-modulated cells (n=96). (d) Decoding performance for all 114 cells in the spontaneous session presented with their locations outlined in the FoV. The 9 channels inside the FoV are marked with black circles. The scale bars show 100μm. (e) Representative examples for decoded (orange) vs ground truth (black) ΔF/F of five best-decoded cells from part (d).

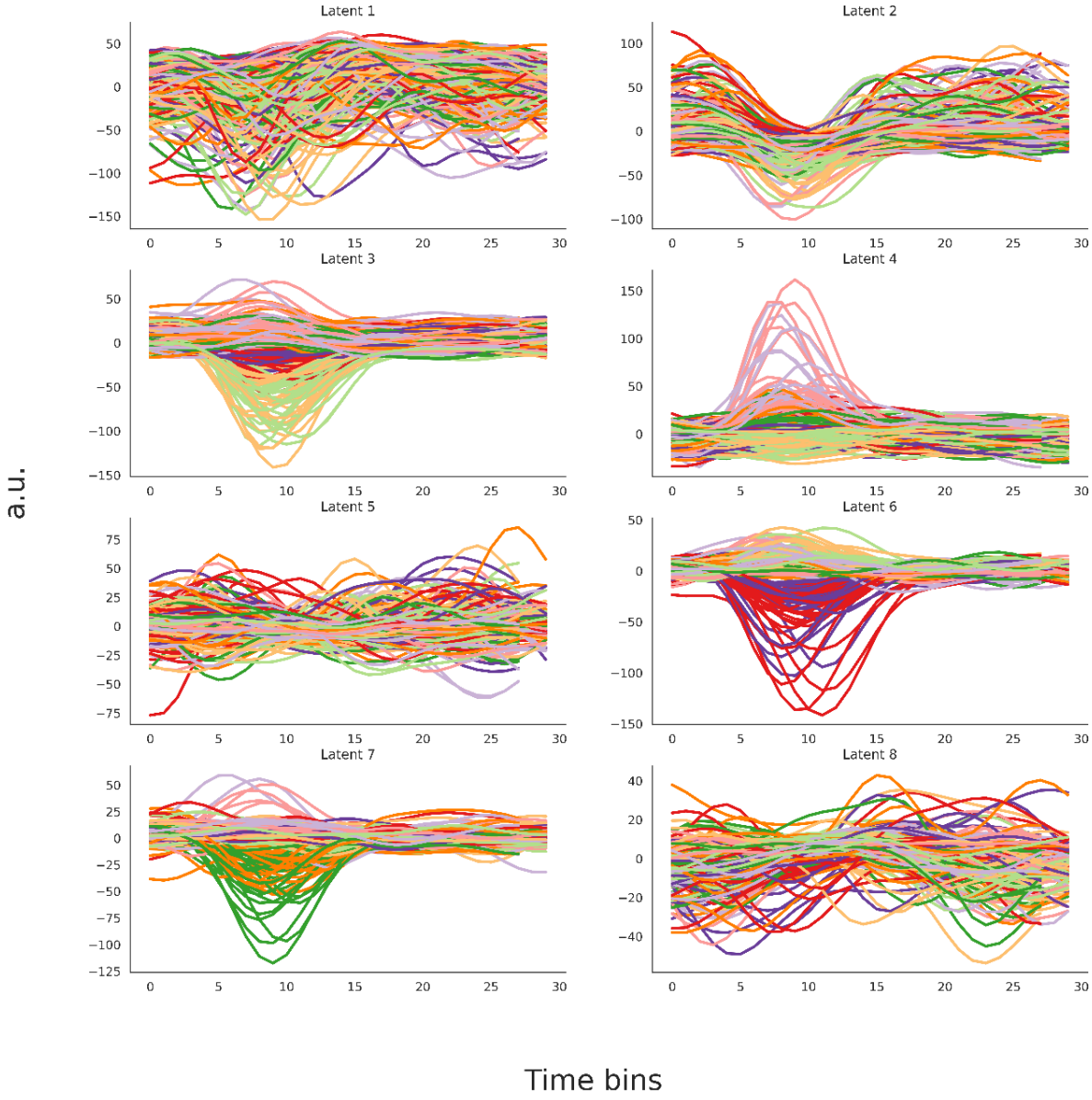

Figure 3.8 **Calcium latents as extracted by GPFA.**

The eight latent variables that we extracted from GPFA are shown with all trials plotted. The trial traces are color coded by condition, purple and red = 45 and 225 degrees, orange and green = 135 and 315 degrees, pink and magenta = 0 and 180 degrees, yellow and lime = 90 and 270 degrees.

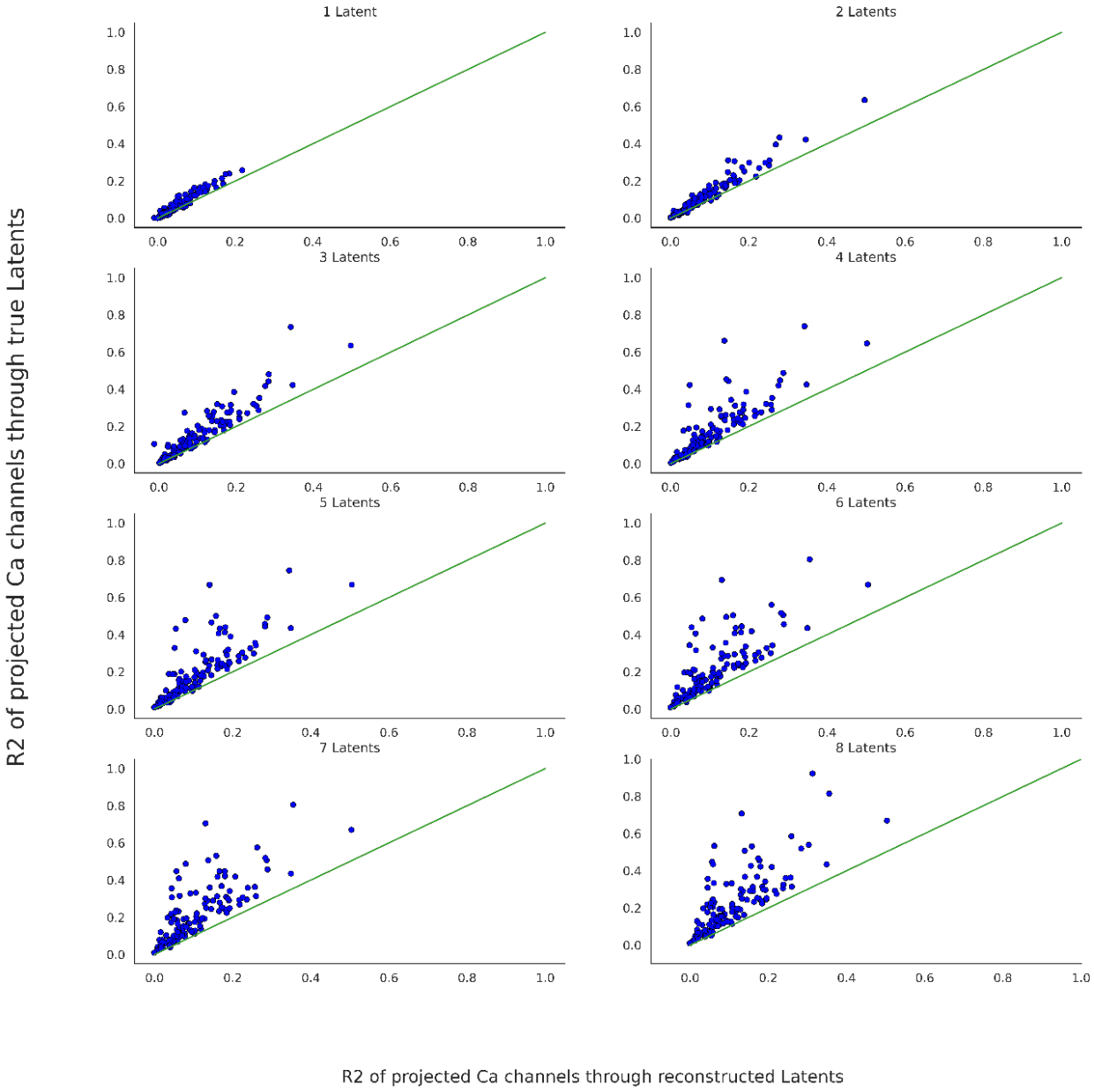

Figure 3.9 **Reconstruction of Calcium response using true latents vs decoded latents.**

We compare the reconstruction accuracy of true latents (extracted from GPFA) and decoded (reconstructed) latents from BiLSTM. The plots are based on how many latent variables have been used in the reconstruction.

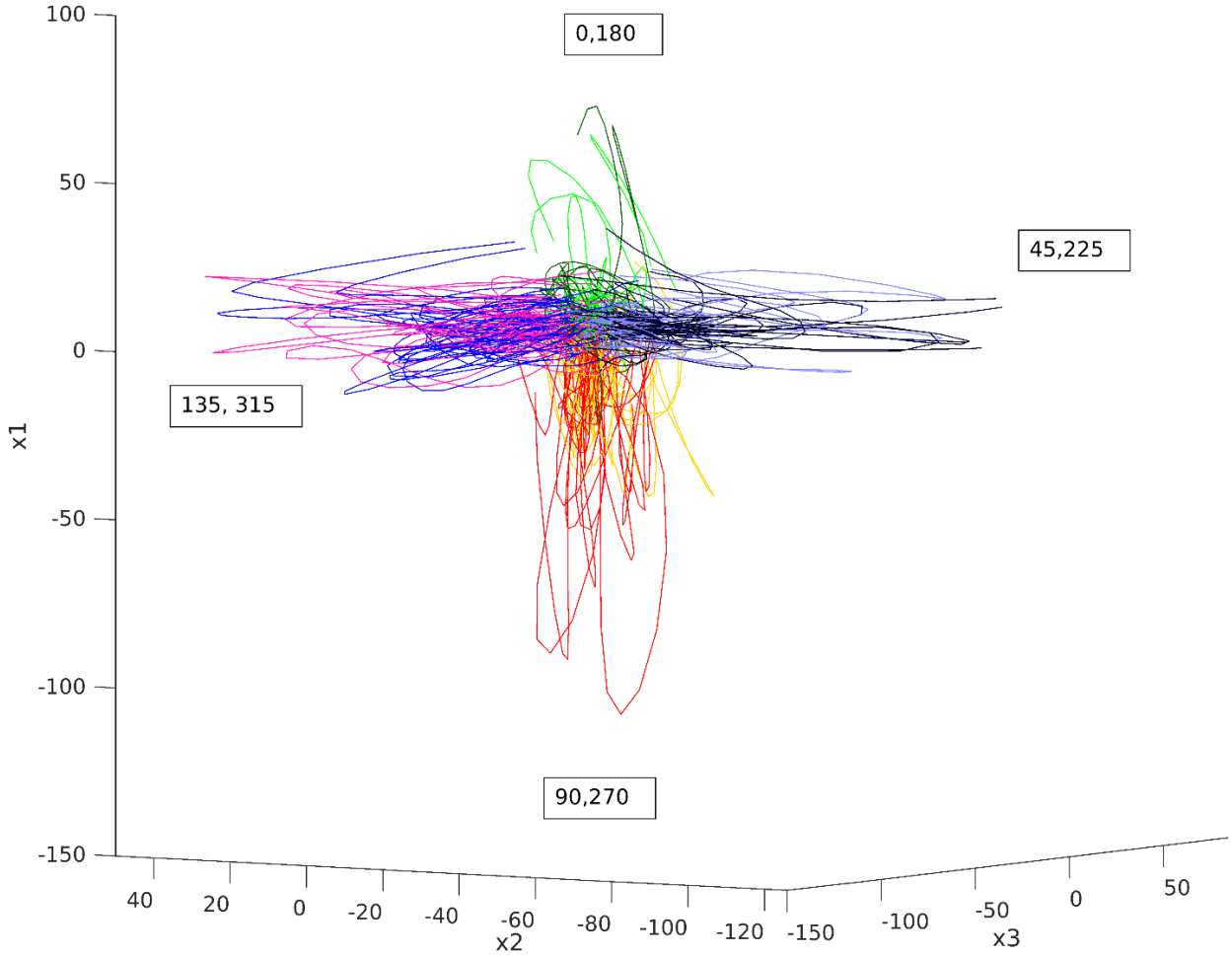

Figure 3.10 **3D plot of three Calcium latents show separability of conditions.**

When 3D plotting the eight latent variables that we inferred from GPFA, we can see separability in the conditions, being the angle direction of the drifting grating stimulus.

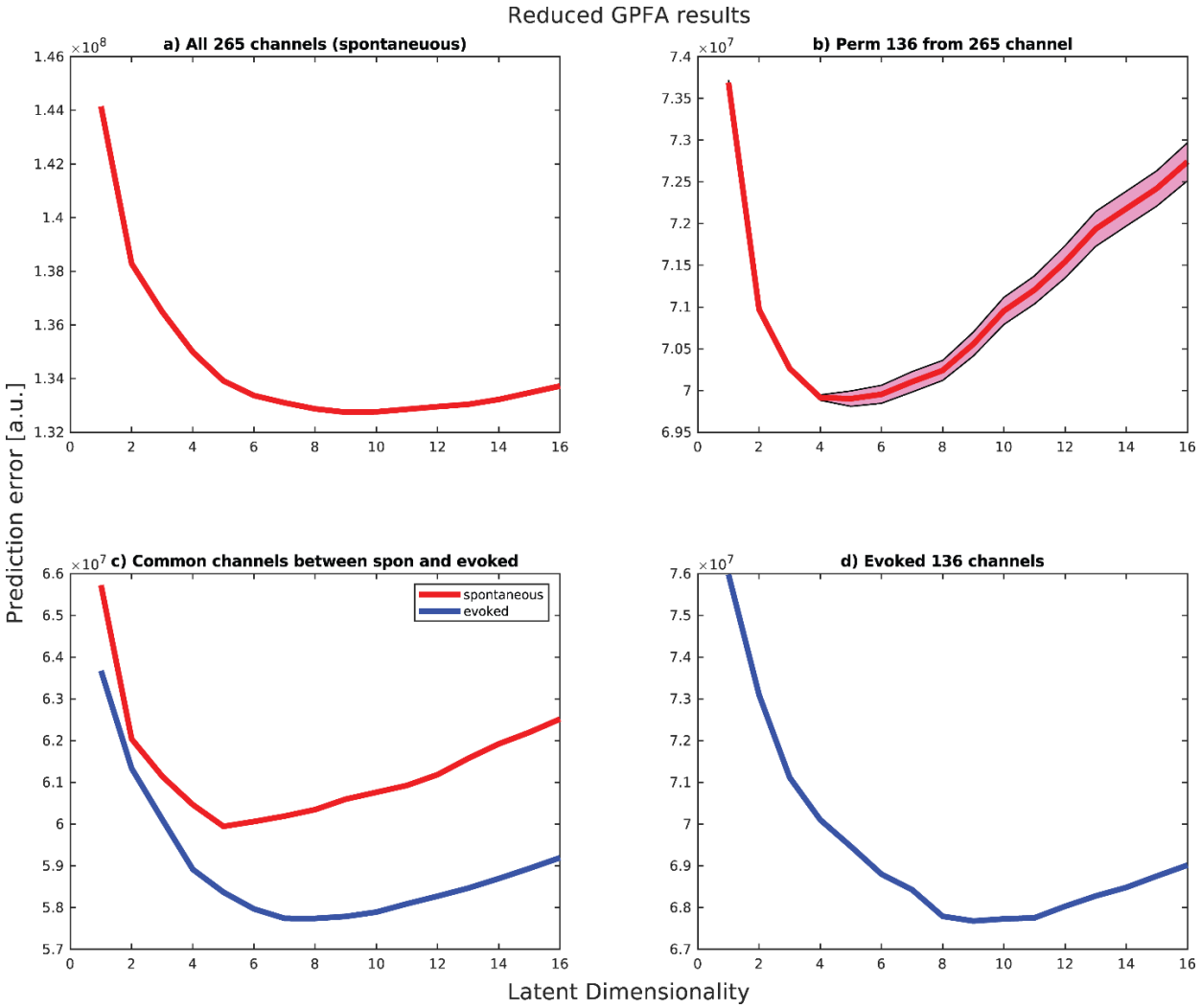

Figure 3.11 **Testing the prediction error for spontaneous and evoked data as a function of number of latents used.**

GPFA trains a dimensionality reduction model that can estimate latent trajectories on a single trial basis, then tests this model through predicting the activity of left-out neurons in the testing set. Therefore, this is a comparison of prediction error in spontaneous activity and evoked activity in v1 in mice. Evoked dataset has 136 regions of interest (ROIs) while the spontaneous set has 265 ROIs since it was recorded in a different experimental session. We expect the prediction error to plateau at a latent dimensionality comparable or larger than evoked since having more channels means more decoupling. Additionally, to have a fair comparison between the two datasets, we have run the following tests: a) We ran the original 265 ROIs of the spontaneous activity. b) To make it comparable to evoked, we have selected 136 ROIs out of the 265 in spontaneous activity and ran prediction error evaluation. This was repeated 50 times with random permutations each time. c) We compared locations of ROIs between evoked and spontaneous and it resulted in 114 ROIs that are common between the two datasets to make sure we are testing the same set of neurons. We compared prediction errors of those common ROIs in both datasets. d) Lastly, we show the prediction error evaluation in all 136 ROIs in evoked session (original dataset).

Chapter 4

Leveraging latent modeling in multimodal neural recording for accurate brain state estimation

Abstract

Advances in neural interfaces technologies have given rise to multimodal recordings in neurophysiological studies. Due to the complexity of the brain in how it encodes behavior and responds to stimuli, we require access to information that span diverse time and spatial scales which can be only captured by those multimodal recording techniques. However, the potential of these techniques is yet to be fully realized as analysis methods are still underdeveloped. We present in this work a generalized framework that aims to unify multiple modalities in a common subspace and combine their advantages. We leverage modeling of the latent modes of each modality in order to harness their advantages in low-dimensional subspace which can be used to enhance brain state estimation. Additionally, we show that we can recover latent modes of one modality using the other when aligning in that common subspace.

Introduction

Studying the complex dynamics of the brain is critical to understanding its function and how to develop targeted brain-computer interfaces (BCI) to people with neurological diseases. Estimating brain state, or how the brain responds to stimuli, requires access to information that spans diverse spatial and temporal scales [1]. For example, advances in microelectrode array recordings have opened a window into complex dynamics on the microscale using surface electrocorticography (ECoG) electrodes. ECoG signals can record fast dynamics and quick changes in brain response to its high sampling rate. Previously, it has been used to identify epileptic seizure foci [2], and a number of BCI studies [3-7]. However, they cannot offer a full picture of brain state due to their limited spatial sampling. On the other hand, intracortical electrode arrays can be utilized to record brain signals at rates high enough to process action potential (spikes) at the single neuron level and deliver high fidelity estimation of brain state [8-10]. Yet estimated states through these recordings are limited by cell-response heterogeneity [11], although emerging high-density large-scale electrode arrays promise to improve detection of cell-type specificity [12]. In parallel with microelectrode technologies, optical tools have given rise to the ability to investigate neural activity at cellular level [13-14]. Calcium imaging in particular provides more insight into a large spatial scale and explores cell response heterogeneity [15-16]. However, these techniques still suffer from low temporal resolution due to slow imaging systems. In summary, current single tools, or technologies available to monitor brain response and its neural dynamics only offer rich reading on one resolution but not the other. This limitation provided motivation to the rise of multimodal technologies which allows simultaneous recording of two different modalities.

Previous multimodal studies sought to study the dynamics of neural populations in applications such as neural circuits [17-23], brain disorders and diseases [24-28], and enhancing performance of brain-machine interfaces (BCI) [28-32]. To date, the most promising multimodal studies are the ones that combine electrophysiological and optical recording modalities as they provide several advantages such as the temporal resolution of electrophysiology and the spatial resolution and cell-type specificity detection of optical imaging. This was made possible through the development of transparent graphene microelectrode arrays [33, 34].

In this work, we develop a generalized framework that aims to unify multiple modalities of different spatial and temporal resolution in a common subspace in which their advantages can be combined for enhanced understanding of neural response. This framework is predicated on the assumption that two modalities recorded simultaneously from the same region are governed by the same underlying process. Previous work, particularly in motor physiology studies, has demonstrated that this underlying process can be described by latent modes in low-dimensional space that capture a significant fraction of the population covariance [35-41]. One can drive an online BCI and control a neural prosthetic using those modeled latent variables [42-43]. Therefore, by modeling the latent variables of both modalities in one low-dimensional subspace, we can combine their advantages which can be used to accurately estimate brain state in response to stimuli (Figure 4.1). Additionally, this was motivated by a previous multimodal study where we were able to predict calcium response at single level from spectral features of surface electrophysiological recordings (previous chapter). We apply this framework to a study of combined two-photon imaging and surface high-density electrodes recorded from the visual cortex in an awake mice subject to visual stimulation. We first demonstrate the advantages of each

modality separately then unify them in a common subspace. Additionally, we show how we can recover one modality from the other within that unified subspace.

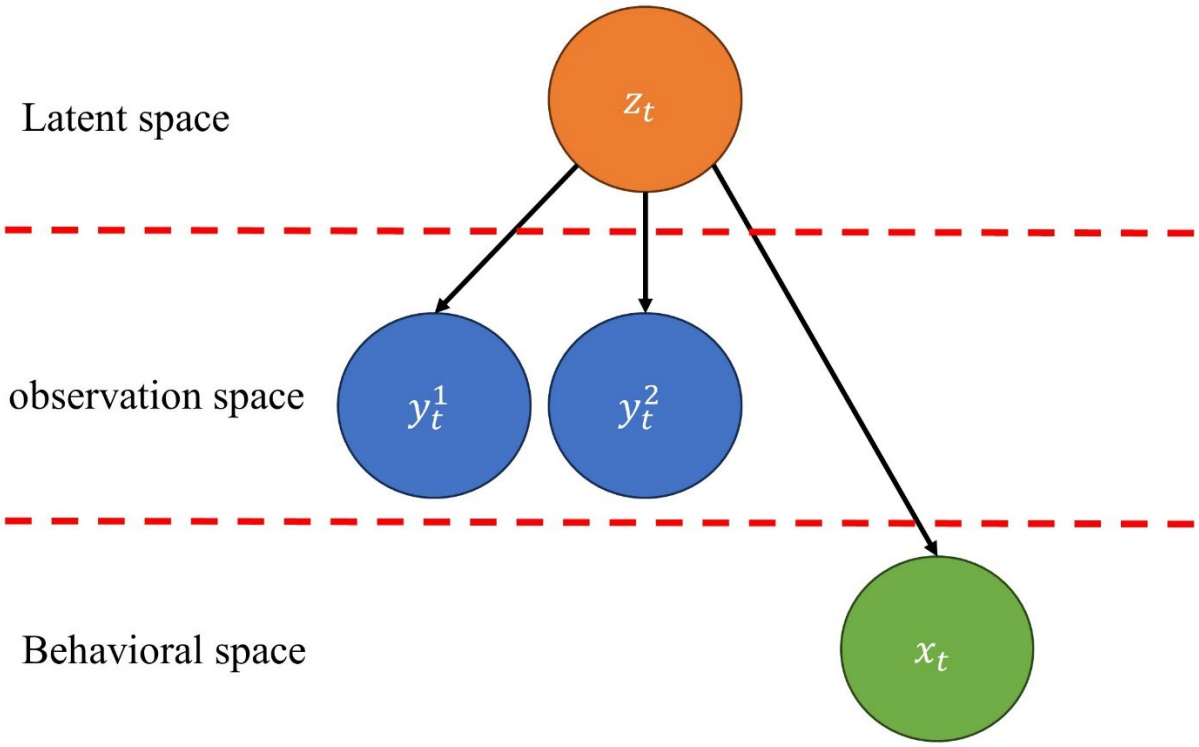

Figure 4.1 **Graphical representation of the relationship between brain state, latent state, and behavior.**

One of the more popular theories states that the intended behavior and neural measurements are not directly connected but through intermediate latent neural state, z_t. This latent state represents the underlying process that generates both the neural activity that we measure and the intended behavior/response to stimuli.

Results

Single channel response reveals temporal differences in modalities.

To reveal the difference in temporal response between the two modalities in this study, ECoG and calcium response, we plot the trial-averaged response per conditions for one ECoG channel and Calcium region of interest (ROI) (Figure 4.2). Both responses were selected from the same approximate location relative to the observed field of view (FoV) in order to maximize the similarity in the response specificity. It should be noted that a single channel is not indicative of the population response, but it was done for demonstration purposes.

In Figure 4.2, we can observe that for all conditions, the average electrophysiological response is much faster than the calcium response, raising to max value almost instantly after stimulus onset ($t = 0$). Additionally, the error margin in the ECoG response shows that this rise is observed across all trials with little variation, while in the calcium signal, the reported error margin indicates the degree to which it can respond to stimulus onset can vary. To further demonstrate the point, Figure 4.3 shows the histogram of the time required to reach maximum response value in both modalities relative to stimulus onset. This was measured in the same two channels as the previous result.

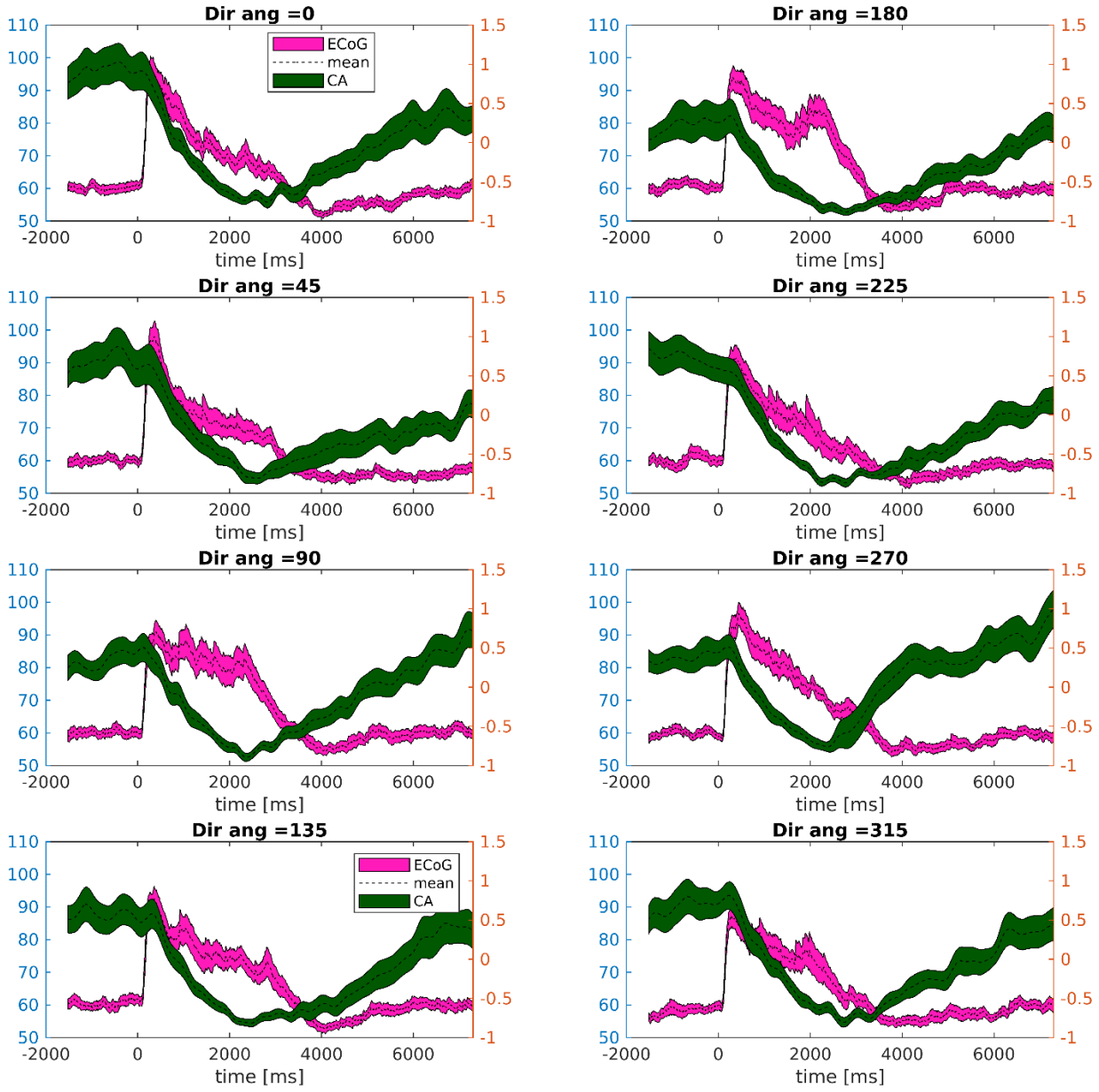

Figure 4.2 **Single channel of both ECoG and Calcium response to Stimulus onset.**

The direction angle of the drifting grating (methods) is indicated in the title of each subplot. Each plot is the average of a single Calcium and the average of high gamma features from a single ECoG channel. The dotted line is the mean of each signal and the error bar represents the 95% confidence. At time $t = 0$, the stimulus is presented to the animal and at time $t = 2$ seconds, the stimulus is turned off.

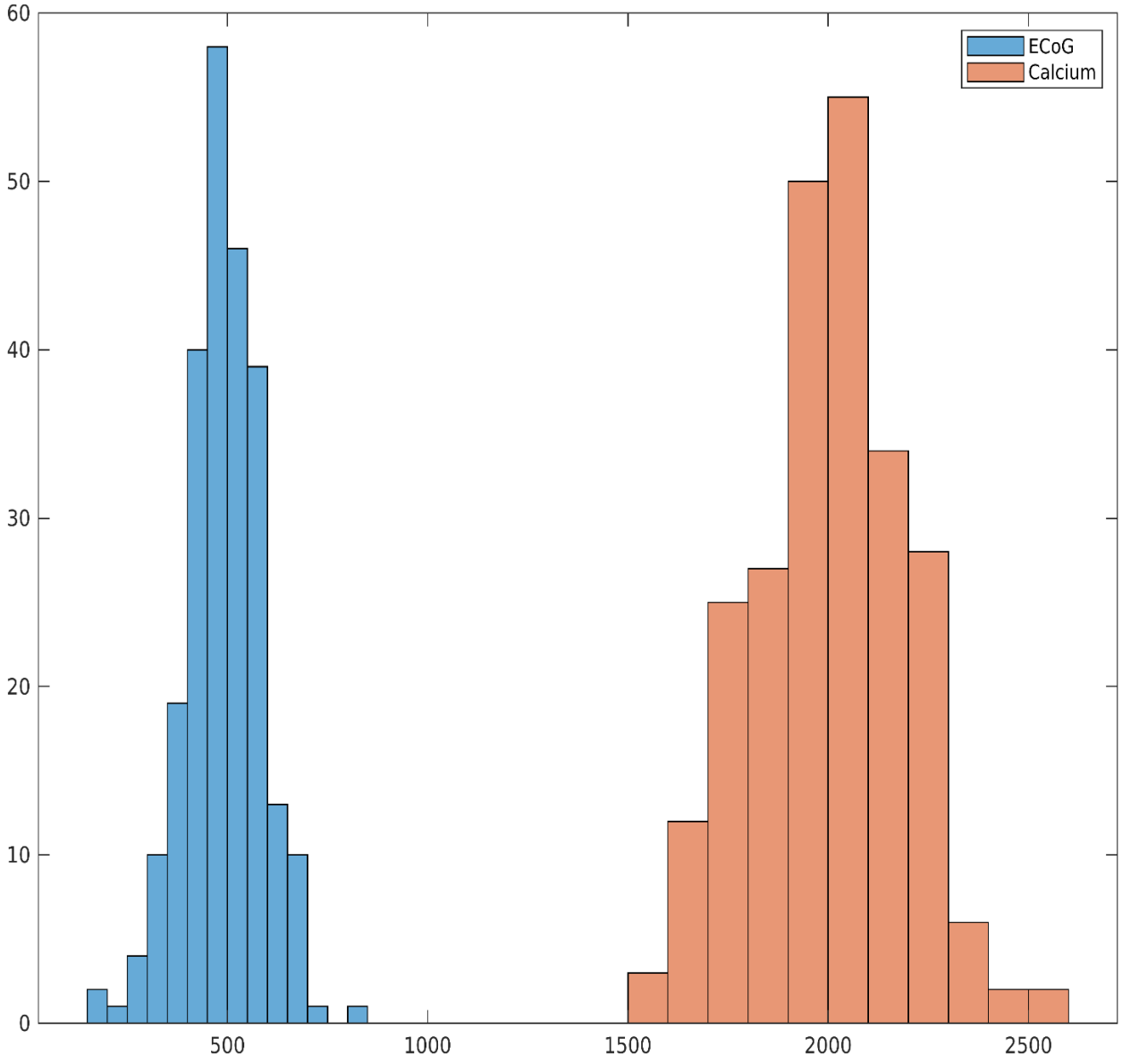

Figure 4.3 **Histogram of maximum value response.**

For all single trials, we measured the response time in both ECoG and Calcium relative to stimulus onset for the two single channels to illustrate the difference in the temporal resolutions. We limited the duration to 5 seconds after stimulus onset to eliminate any outlier response times that were mostly present in the Calcium signals.

Demixed principal component analysis reveals the population dynamics in both modalities.

Because Calcium imaging often provides better information on cell-type specificity, we expect it to have a more distinct response to different conditions of stimuli when compared to ECoG. We can see hints of this in Figure 4.2; the transient response in the Calcium signal is different between conditions. Additionally, we expect the responses to drifting grating stimuli at angles 180 degrees apart to be similar as the orientation is still the same.

To study the response at the population level in both modalities, we resort to demixed principal component analysis (dPCA) to uncover the time dependency and stimulus dependency in the principal components (PC; see methods). We trained dPCA with 4 conditions only as the other 4 conditions have the same orientation on the drifting grating direction (e.g., direction zero degree and 180 degrees). We extract both time components and stimulus components to understand their effect in both modalities. Figure 4.4 shows Calcium signals at the population level have very distinct responses to different stimuli, with drifting grating at 90 degrees being strongest. While its temporal response on the population level is very robust, it is very slow and confirms with Figure 4.3. On the ECoG side of recordings, the fast temporal response is evident in the entire population recorded with a very narrow error margin in the transient response. Yet its limited spatial sampling makes the stimuli components indistinct compared to Calcium. Figure 4.9 shows the top 3 stimulus components in Calcium response which demonstrates clear separation of conditions in the latent space.

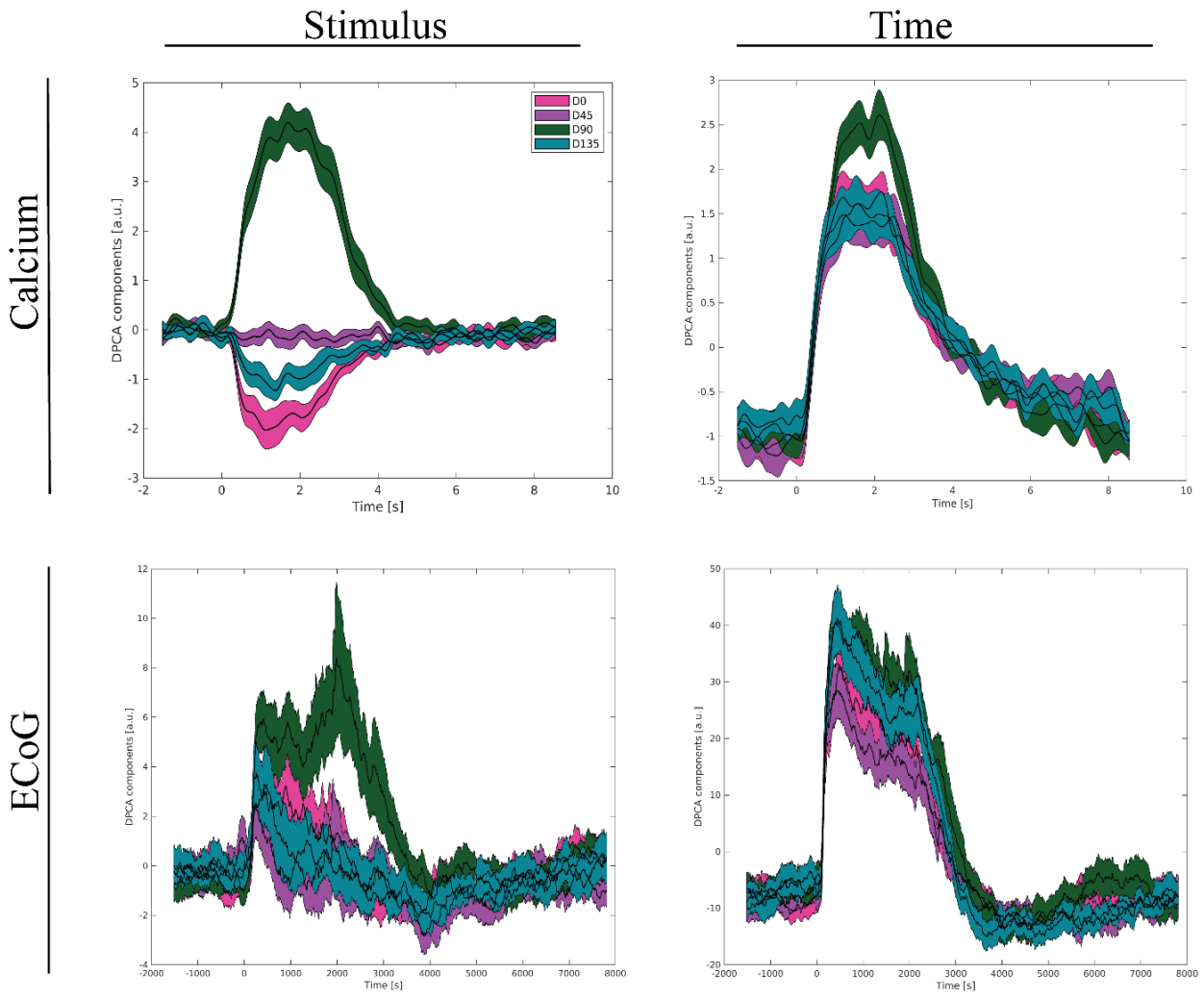

Figure 4.4 **Demixed principal component analysis of the two modalities.**

Breakdown of the stimulus and time components in both modalities. We applied dPCA to the high gamma features of surface electrophysiological recording and Calcium response at depth. We separate stimulus-dependent components and condition-independent components (time components) for each modality to demonstrate the specific information that we can obtain.

Latent inference using PCA and evaluation BMI application-specific metrics.

To infer latent trajectories in the two modalities, we need to extract the relevant features first. Our previous work showed that the Calcium response is highly correlated to the high frequency bands of the surface electrophysiological recordings; namely the high gamma frequency

bands ($high\,\gamma = 70 - 150\,Hz$) [mehr, previous chapter]. Therefore, we extract high gamma spectral features from ECoG as part of the preprocessing step. After that, we apply PCA to extract the single trial trajectory with latent dimension = 12. Now even though the two modalities are recorded simultaneously from the same region, they do have their own latent subspaces. For the purpose of accurately estimating brain state, we can benefit from the advantages of both modalities in their own latent subspaces.

To demonstrate the modality-specific information that we can learn, we evaluate metrics that are practical to BMI design. First, we performed condition classification using the PCs of both modalities which detect the angle of the drifting grating stimuli. We don't use all 8 conditions because conditions 180 degrees apart have the same drifting grating orientation which have similar neural response (Figure 4.9) and therefore it can influence the classification accuracy. Figure 4.5 shows the result of classification, the difference in performance between the two modalities. Conforming the dPCA result, Calcium PCs show better classification accuracy compared to ECoG due to its dense spatial resolution and ability to detect cell-specificity. Additionally, the accuracy of Calcium PCs rises above binomial chance fast relative to stimulus onset (methods). The second evaluation metric is to investigate how fast each modality can detect the onset of visual stimuli. We used epochs of the PCs of each modality to detect whether there is a response to stimulus through comparing it to baseline (Methods). Figure 4.6 shows that due to their fast temporal resolution, ECoG PCs have faster detection of stimulus onset compared to Calcium PCs. The results show high detection accuracy as fast as 100 ms after stimulus onset. This is an important step towards real-time detection of visual stimuli in order to build functional BMIs.

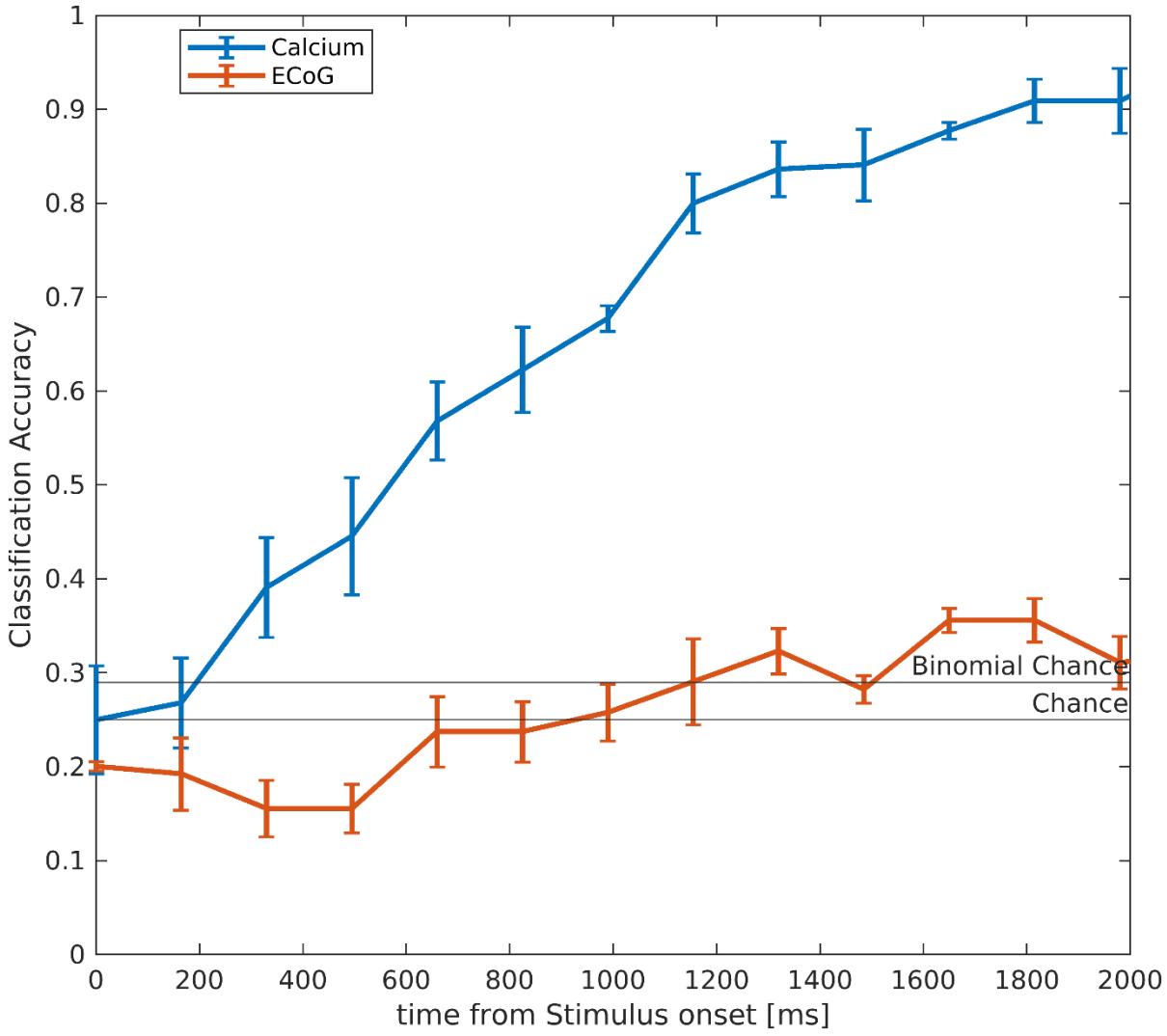

Figure 4.5 **Classification accuracy of drifting grating angles.**

We used the PCs of both modalities to classify the drifting grating angles using the mean of the signals measured from stimulus onset as feature input to the classifier. The traces displayed are the means of five-fold cross validation and the error bars represent the 95% confidence interval.

Alignment in the latent space

We postulated before that the two simultaneously recorded modalities have the same underlying neural process. Therefore, when we extract latent modes, we look at the subspace of that underlying process from a different window that corresponds to a different modality. In order to align those two windows, we apply a method canonical correlation analysis (CCA) to unify the

two sets of latent modes in a subspace where correlation is the highest. The goal of this alignment is to be able to recover the PCs of one of the modalities using the other through that unified subspace (Figure 4.7).

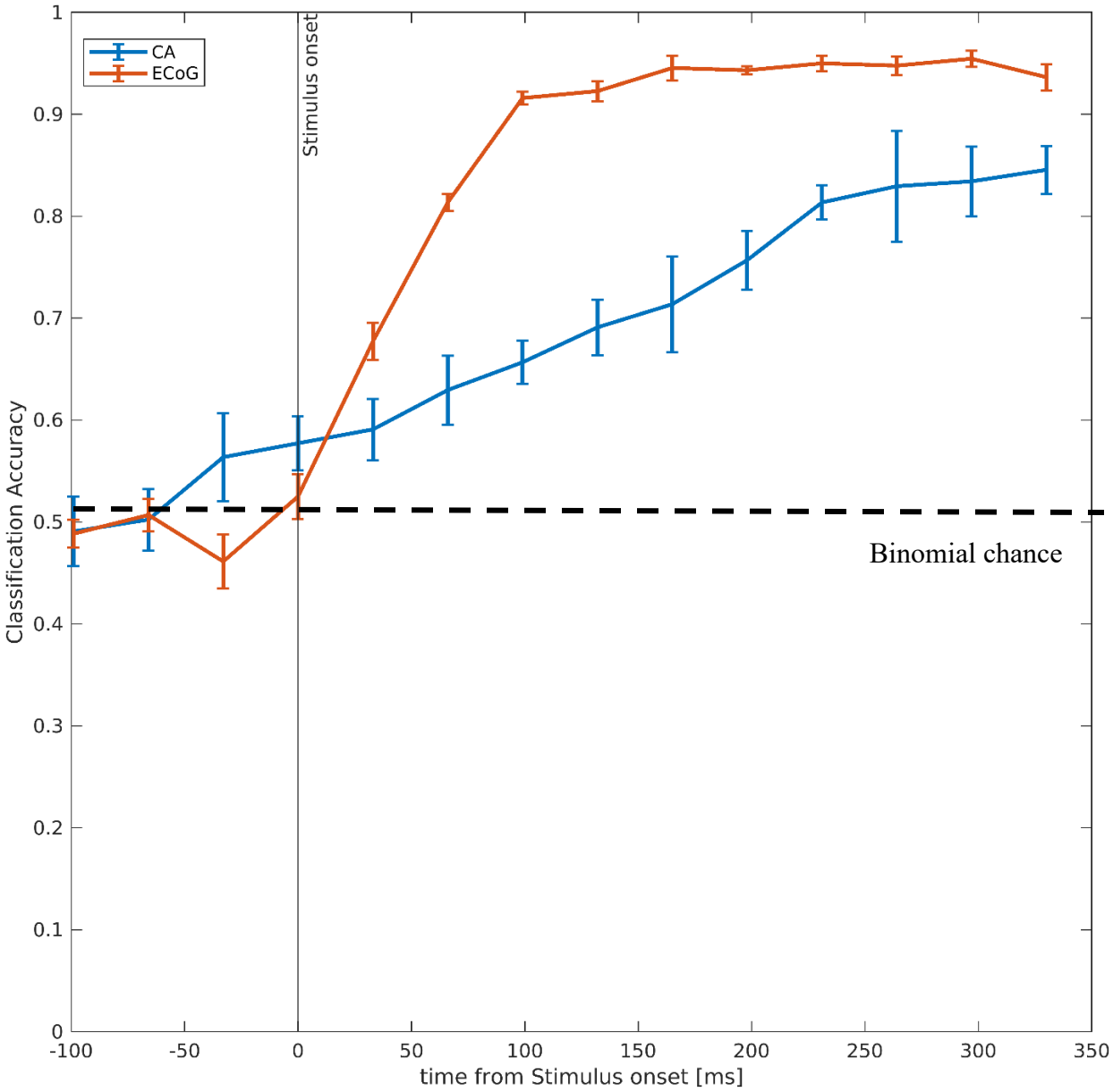

Figure 4.6 **Detection of stimulus onset.**

We used the PCs of both modalities to detect the onset of visual stimulus by comparing epochs of PCs against pre-stimulus onset baseline. The traces displayed are the means of five-fold cross validation and the error bars represent the 95% confidence interval.

Next, we asked whether we could benefit from the advantages of one modality using recovered PCs from another modality. Therefore, after aligning the PCs of both modalities using CCA, we recovered Calcium PCs using aligned ECoG PCs (Figure 4.7). Next, we performed stimulus classification using Calcium PCs, ECoG PCs and Calcium PCs recovered from aligned ECoG PCs. Interestingly, the Calcium PCs that we recovered from aligned ECoG PCs performed better than ECoG PCs but much worse than the original Calcium PCs (Figure 4.8).

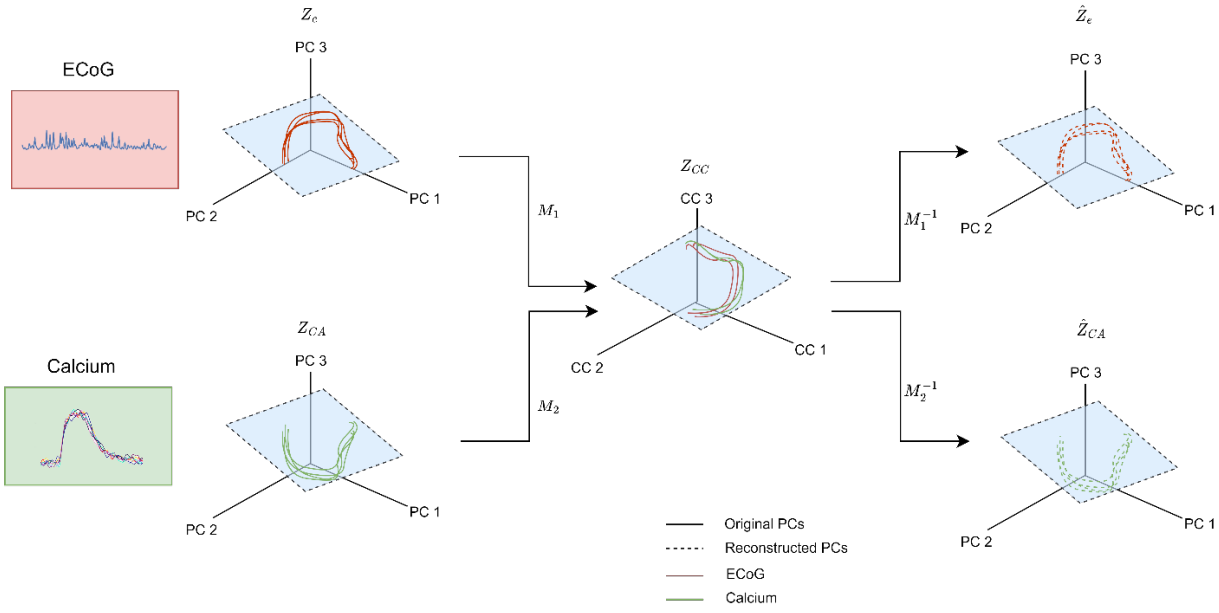

Figure 4.7 **Alignment of the PCs using canonical correlation analysis.**

After extracting the PCs of both ECoG and Calcium, we apply canonical correlation analysis to unify them in an aligned subspace where the correlations between their PCs is maximized. We postulate that we can recover the PCs one of modality using the PCs of the other modality through this aligned subspace.

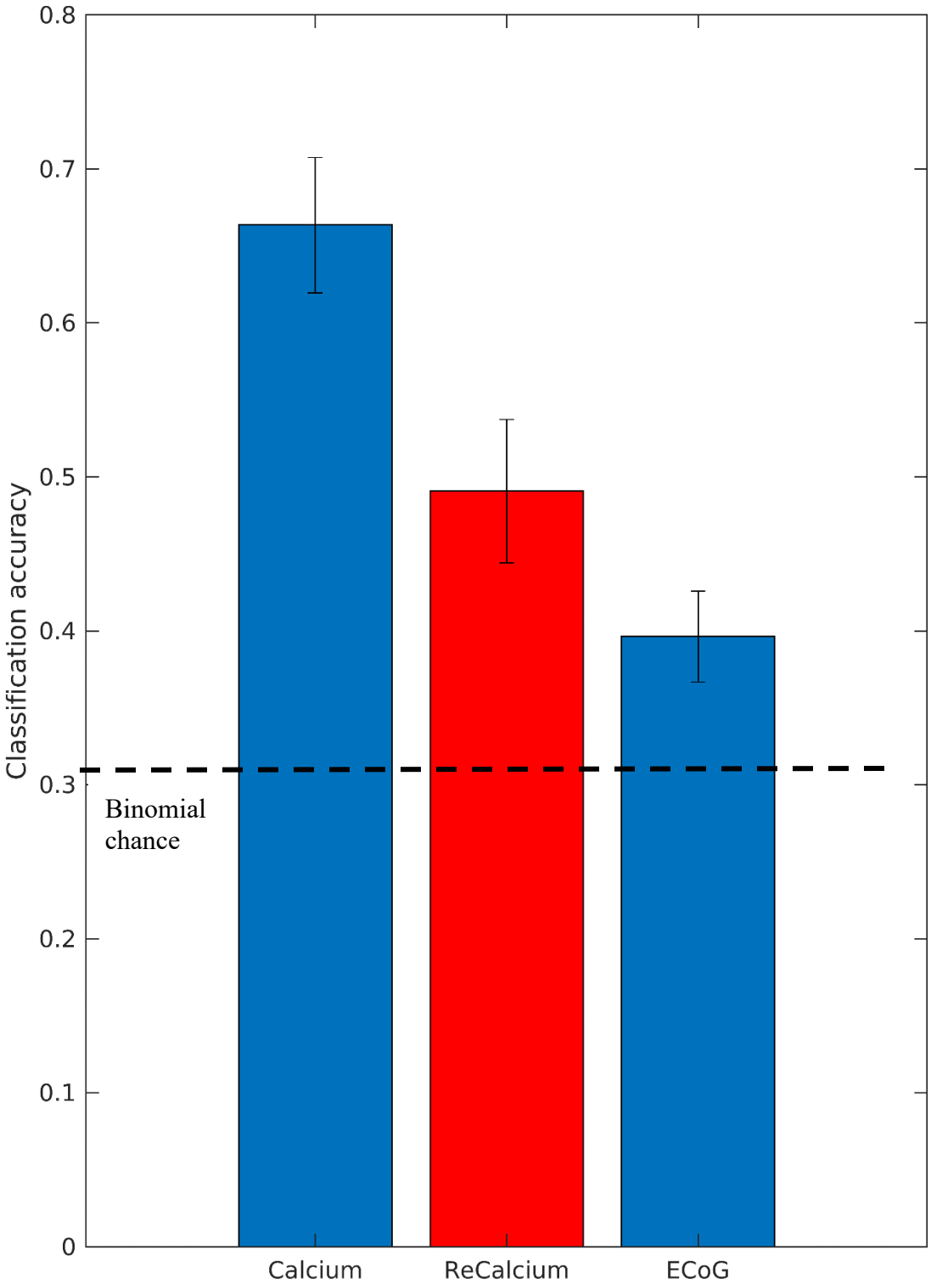

Figure 4.8 **Classification accuracy using PCs of different modalities.**

We measure the classification accuracy of drifting grating direction using PCs of different modalities as a function of the feature duration after stimulus onset. We compare Calcium PCs, ECoG PCs and finally Calcium PCs reconstructed from aligned ECoG PCs in a unified subspace using CCA (labeled ReClacium).

Discussion

In this chapter, we showed that we can combine the benefit of two modalities, surface electrophysiology and depth Calcium imaging, which have recorded simultaneously in the same region by extracting and modeling their dominant neural modes in the low-dimensional space. Additionally, we show that we can align these two sets of neural modes in a unified subspace using CCA and be able to recover the modes of one modality from the other. First, in Figure 4.2, we show the advantages of each modality by plotting per-condition trial-averaged signals of a single channel from each neural recording. Surface electrophysiological recordings offer observations at fast temporal dynamics and therefore we can observe the rapid rise in the surface potential immediately after stimulus onset, making it a good modality for stimulus onset detection. On the other hand, Calcium signals offer a much diverse varied transient response to different stimuli conditions making it ideal for condition classification, although it comes at a cost of unreliable stimulus onset detection due to slow imaging techniques. To further demonstrate the two modalities' various advantages in their respective scales at the population level as compared to single channel, we apply dPCA (methods) to the dataset to demonstrate the stimulus-dependent and time-dependent components in both modalities. Figure 4.4 shows that in the Calcium signals of the population activity have diverse response to stimuli as demonstrated by the distinct stimulus component for each condition. Additionally, surface recording of the population activity also demonstrates the marginally-narrow immediate response to stimulus onset. In Figure 4.8Figure 4.5 shows the classification accuracy of the PCs of both modalities in addition to Calcium PCs recovered from aligned ECoG PCs. The results suggest Calcium imaging, due to its capability of detecting cell-type, is suitable for classifying stimulus condition. On the other hand, ECoG PCs classification performance is expectedly very poor due to its limited spatial sampling. Finally,

when recovering Calcium PCs, we observe a rise in the classification performance even though it doesn't reach the level of the original Calcium PCs. This provides an opportunity to suggest techniques to recover BCI performance in multimodal experiments when we lose the ability to record from one modality due to various technical reasons. Lastly, we measure the time difference between the two modalities due to the nonlinearities between them through canonical correlation. We slide the time difference between them and measure the correlation. Figure 4.10 shows that the correlation is maximized when Calcium leads ECoG by 100 ms.

One important thing to note is the choice of latent modeling technique utilized in this study. As we want to present a proof of concept to the ability of unifying multimodalities in one subspace, we went with the simplest modeling technique, principal component analysis. Additionally, there are studies that previously demonstrated the capability of aligning single modalities across multiple days and subjects using PCA and CCA for alignment [36]. We postulate that better modeling techniques will yield better inference of the latent variables in different modalities. This is mainly due to the choice of model choice being on the observation dataset and how some choices can be an ill fit for certain data types. Secondly, there are other latent modeling techniques that consider the wide range of temporal scales that modeled latent modes can exhibit. We expect that within and across modalities there will be fast and slow latent modes that are better represented by considering the temporal scale of each modality.

Lastly, we show in this study the importance of leveraging latent modeling in multimodal recordings. While primarily in the motor cortex, more studies are emerging in which the latent variables are used to drive an online BMI. Therefore, we emphasize the ability to harness the advantages of both modalities in the latent subspace to allow for more accurate estimation of brain state.

Methods

Visual Stimulation

The visual stimulus is a square wave drifting grating (100% contrast, 0.04 cycles/degree, 3 cycles/sec) was presented on an LCD monitor (30 × 38 cm) positioned 15 cm away from the right eye covering entire contralateral receptive field. The stimuli were presented for 2 or 2.5 sec on each trial in pseudorandom order in a random direction in one of 8 orientations (45° apart). Inter-stimulus-interval was 8 seconds. There are at least 30 trials per condition.

Electrophysiology Data Analysis

We started by rejecting channels that were showing noisy input. In particular, there were channels that had saturated amplifier output signal, so we removed those entirely. Next, we examined the remaining viable channels and investigated each separately to see whether they had the amplifier output saturation and rejected those trials. Next, we calculated the common average reference and subtracted it from all remaining channels. The signals are lowpass filtered below 250 Hz using a 6^{th} order Butterworth filter to achieve the local field potential (LFP). Next, we extract the high gramma activity ($high\ \gamma$: $70-150\ Hz$) using 6^{th} order Butterworth bandpass are applied with corresponding frequency range.

The power signal of the high gamma was calculated by taking the square of the bandpass filtered signals and applying a 50ms exponential filter to reduce the noise. We used a one-sided exponential filter to preserve the causality of the signal.

Demixed Principal Component Analysis

In order to decompose population activity into a few components that dependent on task parameters, we utilize demixed principal component analysis, a supervised decomposition technique that exposes that dependance [44]. With this technique, we can describe how much variance can be explained by the visual stimulation in both surface electrophysiology and depth Calcium imaging. It applies marginalization procedure to the whole data set Y to break into components across which the variability is maximized:

$$Y = Y_t + Y_{ts} + Y_{noise} = \sum_{\phi} Y_\phi + Y_{noise}$$

where t, and ts are labels that represent time and stimulus task variables. Once the data is decomposed in this manner, dPCA finds a separate decoder D_ϕ and an encoder F_ϕ by minimizing the loss function:

$$L_{dPCA} = \sum_{\phi} ||Y_\phi - F_\phi \, D_\phi Y \, ||^2$$

Condition classification

We assess how well the latent variables we learn from modality can relate to the behavior by classifying the drifting grating angle in the visual stimuli presented to the animal. We decode the orientation by using a feature set extracted from those variables into a five-fold linear naïve Bayes classifier with Gaussian distribution [45]:

$$P\left(\bar{z}\middle|C_j\right) = \frac{1}{(2\pi)^{\frac{D}{2}}|\Sigma|^{\frac{1}{2}}} e^{\frac{1}{2}(\bar{z}-\mu_j)' \Sigma^{-1} (\bar{z}-\mu_j)}$$

where $\bar{z} \in \mathbb{R}^{D\ x\ 1}$ is the average of the latent variables obtained. The x-axis in Figure 4.5 represents the length of the latent variable signal used to obtain this mean relative to stimulus onset. In the classification equation, μ_j is the mean of the feature set per stimulus condition while Σ is the covariance matrix, constrained to be diagonal and the same across all conditions.

Stimulus onset detection

To detect stimulus onset using the PCs of both modalities, we created two sets of trials. One set consists of 450 ms trials around stimulus onset (-100, 350), and the other is a baseline set of the same duration. We split trials of each set into 30 ms epochs and use them as features in a support vector machine (SVM) classifier with linear kernel to classify the source of each epoch (either stimulus or baseline set). When both sets are at baseline epochs (pre-stimulus in the first set), we expect the classification accuracy of SVM to be at chance. However, when the stimulus is introduced, we expect the classification of stimulus set to increase due to change in activity. We use this technique to simulate real-time detection of stimulus onset.

Canonical Correlation Analysis

We utilize CCA to find a new subspace between the latent variables of two modalities that maximizes the correlation between them. This results in two matrices that can be used to project these latent variables into the new subspace, hence we call them aligned latents (PCs). In order to recover the latents of one modality from another, we decode them by inversing the alignment matrix that we obtained from training CCA.

Acknowledgments

Chapter 4, in part is currently being prepared for submission for publication of the material. Abdullah Alothman**,** Mehrdad Ramezani, Jeong-Hoon Kim, Xin Liu, Chi Ren, Chawina De-Eknamkul, Madison N. Wilson, Ertugrul Cubukcu, Takaki Komiyama, Duygu Kuzum, and Vikash Gilja, *" Leveraging latent modeling in multimodal neural recording for accurate brain state estimation".*

We thank members of the Kuzum lab for the helpful discussion and the collaboration we did that helped us shape the idea of this work.

Author Contributions

This work was conceived by A.A. and V.G. Microelectrode array fabrication was performed by J.-H.K and the characterization of arrays was performed by J.-H.K, C.D.-E., and M.W. All animal experiments were performed by C.R., X.L. and M.R. The data analysis was performed by A.A with contributions from M.R., D.K and V.G. The manuscript was written by A.A. and V.G. and edited by all authors.

References

[1] J. A. Frank, M.-J. Antonini, and P. Anikeeva, "Next-generation interfaces for studying neural function," *Nature biotechnology,* vol. 37, no. 9, pp. 1013-1023, 2019.

[2] Ivan Osorio, Mark G Frei, Jon Giftakis, Tom Peters, Jeff Ingram, Mary Turnbull, Michele Herzog, Mark T Rise, Scott Schaffner, Richard A Wennberg, et al. Performance reassessment of a real-time seizure-detection algorithm on long ecog series. Epilepsia, 43(12):1522–1535, 2002.

[3] Metzger, S. L., Liu, J. R., Moses, D. A., Dougherty, M. E., Seaton, M. P., Littlejohn, K. T., Chartier, J., Anumanchipalli, G. K., Tu-Chan, A., Ganguly, K., & Chang, E. F. (2022). Generalizable spelling using a speech neuroprosthesis in an individual with severe limb and vocal paralysis. *Nature communications*, *13*(1), 6510. https://doi.org/10.1038/s41467-022-33611-3

[4] Silversmith, D. B., Abiri, R., Hardy, N. F., Natraj, N., Tu-Chan, A., Chang, E. F., & Ganguly, K. (2021). Plug-and-play control of a brain-computer interface through neural map stabilization. *Nature biotechnology*, *39*(3), 326–335. https://doi.org/10.1038/s41587-020-0662-5

[5] Rabbani, Q., Milsap, G., & Crone, N. E. (2019). The Potential for a Speech Brain-Computer Interface Using Chronic Electrocorticography. *Neurotherapeutics: the journal of the American Society for Experimental NeuroTherapeutics*, *16*(1), 144–165. https://doi.org/10.1007/s13311-018-00692-2

[6] Lorach, H., Galvez, A., Spagnolo, V., Martel, F., Karakas, S., Intering, N., Vat, M., Faivre, O., Harte, C., Komi, S., Ravier, J., Collin, T., Coquoz, L., Sakr, I., Baaklini, E., Hernandez-Charpak, S. D., Dumont, G., Buschman, R., Buse, N., Denison, T., … Courtine, G. (2023). Walking naturally after spinal cord injury using a brain-spine interface. *Nature*, *618*(7963), 126–133. https://doi.org/10.1038/s41586-023-06094-5

[7] Shirvalkar P, Prosky J, Chin G, Ahmadipour P, Sani OG, Desai M, Schmitgen A, Dawes H, Shanechi MM, Starr PA, Chang EF. First-in-human prediction of chronic pain state using intracranial neural biomarkers. Nat Neurosci. 2023 Jun;26(6):1090-1099. doi: 10.1038/s41593-023-01338-z. Epub 2023 May 22. PMID: 37217725; PMCID: PMC10330878.

[8] Jonathan C. Kao, Paul Nuyujukian, Stephen I. Ryu, Mark M. Churchland, John P. Cunningham, and Krishna V. Shenoy. Single-trial dynamics of motor cortex and their applications to brainmachine interfaces. *Nature Communications*, 6(1):7759, November 2015.

[9] Vikash Gilja, Chethan Pandarinath, Christine H. Blabe, Paul Nuyujukian, John D. Simeral, Anish A. Sarma, Brittany L. Sorice, J´anos A. Perge, Beata Jarosiewicz, Leigh R.

Hochberg, Krishna V. Shenoy, and Jaimie M. Henderson. Clinical translation of a high-performance neural prosthesis. *Nature Medicine*, 21(10):1142–1145, October 2015. Number: 10 Publisher: Nature Publishing Group.

[10] Chethan Pandarinath, Paul Nuyujukian, Christine H Blabe, Brittany L Sorice, Jad Saab, Francis R Willett, Leigh R Hochberg, Krishna V Shenoy, and Jaimie M Henderson. High performance communication by people with paralysis using an intracortical brain-computer interface. *eLife*, 6:e18554, February 2017. Publisher: eLife Sciences Publications, Ltd.

[11] Xiao, Dongsheng, Matthieu P. Vanni, Catalin C. Mitelut, Allen W. Chan, Jeffrey M. LeDue, Yicheng Xie, Andrew CN Chen, Nicholas V. Swindale, and Timothy H. Murphy. "Mapping cortical mesoscopic networks of single spiking cortical or sub-cortical neurons." *Elife* 6 (2017): e19976.

[12] Zhiwen Ye, Andrew M Shelton, Jordan R Shaker, Julien M Boussard, Jennifer Colonell, Sahar Minavi, Susu Chen, Charlie Windolf, Cole Hurwitz, Tomoyuki Namima, Frederico Pedraja, Shahaf Weiss, Bogdan Raducanu, Torbjørn Ness, Gaute T Einevoll, Gilles Laurent, Nathaniel B Sawtell, Wyeth Bair, Anitha Pasupathy, … Nicholas A Steinmetz. (2023). Ultra-high density electrodes improve detection, yield, and cell type specificity of brain recordings. *BioRxiv*, 2023.08.23.554527.https://doi.org/10.1101/2023.08.23.554527

[13] Kim, T. H., Zhang, Y., Lecoq, J., Jung, J. C., Li, J., Zeng, H., Niell, C. M., & Schnitzer, M. J. (2016). Long-Term Optical Access to an Estimated One Million Neurons in the Live Mouse Cortex. *Cell reports*, *17*(12), 3385–3394. https://doi.org/10.1016/j.celrep.2016.12.004

[14] Stringer, C., Pachitariu, M., Steinmetz, N., Reddy, C. B., Carandini, M., & Harris, K. D. (2019). Spontaneous behaviors drive multidimensional, brainwide activity. *Science (New York, N.Y.)*, *364*(6437), 255. https://doi.org/10.1126/science.aav7893

[15] Sofroniew, Nicholas James, Daniel Flickinger, Jonathan King, and Karel Svoboda. "A large field of view two-photon mesoscope with subcellular resolution for in vivo imaging." *elife* 5 (2016): e14472.

[16] Stirman, Jeffrey N., Ikuko T. Smith, Michael W. Kudenov, and Spencer L. Smith. "Wide field-of-view, multi-region, two-photon imaging of neuronal activity in the mammalian brain." *Nature biotechnology* 34, no. 8 (2016): 857-862.

[17] N. K. Logothetis, O. Eschenko, Y. Murayama, M. Augath, T. Steudel, H. Evrard, M. Besserve, and A. Oeltermann, "Hippocampal–cortical interaction during periods of subcortical silence," *Nature,* vol. 491, no. 7425, pp. 547-553, 2012.

[18] V. Gradinaru, M. Mogri, K. R. Thompson, J. M. Henderson, and K. Deisseroth, "Optical deconstruction of parkinsonian neural circuitry," *science,* vol. 324, no. 5925, pp. 354-359, 2009.

[19] A. Fernández-Ruiz, A. Oliva, M. Soula, F. Rocha-Almeida, G. A. Nagy, G. Martin-Vazquez, and G. Buzsáki, "Gamma rhythm communication between entorhinal cortex and dentate gyrus neuronal assemblies," *Science,* vol. 372, no. 6537, p. eabf3119, 2021.

[20] R. Scheeringa, P. J. Koopmans, T. van Mourik, O. Jensen, and D. G. Norris, "The relationship between oscillatory EEG activity and the laminar-specific BOLD signal," *Proceedings of the National Academy of Sciences,* vol. 113, no. 24, pp. 6761-6766, 2016.

[21] D. Sabatinelli, A. Keil, D. W. Frank, and P. J. Lang, "Emotional perception: correspondence of early and late event-related potentials with cortical and subcortical functional MRI," *Biological psychology,* vol. 92, no. 3, pp. 513-519, 2013.

[22] R. Scheeringa and P. Fries, "Cortical layers, rhythms and BOLD signals," *NeuroImage,* vol. 197, pp. 689-698, 2019.

[23] M. K. Kim, J. C. Leong, Y. Jo, G. Kook, and H. J. Lee, "Multimodal Neural Probes with Small Form Factor Based on Dual-Side Fabrication," *Advanced Materials Technologies,* vol. 8, no. 2, p. 2200692, 2023.

[24] X.-a. Bi, X. Hu, Y. Xie, and H. Wu, "A novel CERNNE approach for predicting Parkinson's Disease-associated genes and brain regions based on multimodal imaging genetics data," *Medical Image Analysis,* vol. 67, p. 101830, 2021.

[25] D. Zhang, Y. Wang, L. Zhou, H. Yuan, D. Shen, and A. s. D. N. Initiative, "Multimodal classification of Alzheimer's disease and mild cognitive impairment," *Neuroimage,* vol. 55, no. 3, pp. 856-867, 2011.

[26] A. Vittala, N. Murphy, A. Maheshwari, and V. Krishnan, "Understanding cortical dysfunction in schizophrenia with TMS/EEG," *Frontiers in Neuroscience,* vol. 14, p. 554, 2020.

[27] X. Li, S. Honda, S. Nakajima, M. Wada, K. Yoshida, Z. J. Daskalakis, M. Mimura, and Y. Noda, "TMS-EEG research to elucidate the pathophysiological neural bases in patients with schizophrenia: a systematic review," *Journal of Personalized Medicine,* vol. 11, no. 5, p. 388, 2021.

[28] M. S. Cetin, J. M. Houck, B. Rashid, O. Agacoglu, J. M. Stephen, J. Sui, J. Canive, A. Mayer, C. Aine, and J. R. Bustillo, "Multimodal classification of schizophrenia patients with MEG and fMRI data using static and dynamic connectivity measures," *Frontiers in neuroscience,* vol. 10, p. 466, 2016.

[29] S. Fazli, J. Mehnert, J. Steinbrink, G. Curio, A. Villringer, K.-R. Müller, and B. Blankertz, "Enhanced performance by a hybrid NIRS–EEG brain computer interface," *Neuroimage,* vol. 59, no. 1, pp. 519-529, 2012.

[30] M. J. Khan and K.-S. Hong, "Hybrid EEG–fNIRS-based eight-command decoding for BCI: application to quadcopter control," *Frontiers in neurorobotics,* vol. 11, p. 6, 2017.

[31] A. M. Chiarelli, P. Croce, A. Merla, and F. Zappasodi, "Deep learning for hybrid EEG-fNIRS brain–computer interface: application to motor imagery classification," *Journal of neural engineering,* vol. 15, no. 3, p. 036028, 2018.

[32] H.-L. Halme and L. Parkkonen, "Across-subject offline decoding of motor imagery from MEG and EEG," *Scientific reports,* vol. 8, no. 1, pp. 1-12, 2018.

[33] N. Driscoll, R. E. Rosch, B. B. Murphy, A. Ashourvan, R. Vishnubhotla, O. O. Dickens, A. T. C. Johnson, K. A. Davis, B. Litt, D. S. Bassett, H. Takano, and F. Vitale, "Multimodal in vivo recording using transparent graphene microelectrodes illuminates spatiotemporal seizure dynamics at the microscale," *Commun Biol,* vol. 4, no. 1, p. 136, Jan 29 2021, doi: 10.1038/s42003-021-01670-9.

[34] Kuzum, D., Takano, H., Shim, E., Reed, J. C., Juul, H., Richardson, A. G., de Vries, J., Bink, H., Dichter, M. A., Lucas, T. H., Coulter, D. A., Cubukcu, E., & Litt, B. (2014). Transparent and flexible low noise graphene electrodes for simultaneous electrophysiology and neuroimaging. *Nature communications*, *5*, 5259. https://doi.org/10.1038/ncomms6259

[35] Saurabh Vyas, Matthew D. Golub, David Sussillo, and Krishna V. Shenoy. Computation Through Neural Population Dynamics. *Annual Review of Neuroscience*, 43(1):249–275, July 2020.

[36] Juan A. Gallego, Matthew G. Perich, Stephanie N. Naufel, Christian Ethier, Sara A. Solla, and Lee E. Miller. Cortical population activity within a preserved neural manifold underlies multiple motor behaviors. *Nature Communications*, 9(1):4233, October 2018. Number: 1 Publisher: Nature Publishing Group.

[37] Barbara Feulner and Claudia Clopath. Neural manifold under plasticity in a goal driven learning behaviour. *PLOS Computational Biology*, 17(2):e1008621, February 2021. Publisher: Public Library of Science.

[38] MM Churchland, JP Cunningham, MT Kaufman, JD Foster, P Nuyujukian, SI Ryu, and KV Shenoy. Neural population dynamics during reaching. *Nature*, 487(7405):51–56, July 2012.

[39] Patrick T. Sadtler, Kristin M. Quick, Matthew D. Golub, Steven M. Chase, Stephen I. Ryu, Elizabeth C. Tyler-Kabara, Byron M. Yu, and Aaron P. Batista. Neural constraints on learning. *Nature*, 512(7515):423–426, August 2014.

[40] Juan A. Gallego, Matthew G. Perich, Lee E. Miller, and Sara A. Solla. Neural Manifolds for the Control of Movement. *Neuron*, 94(5):978–984, June 2017.

[41] Krishna V. Shenoy, Maneesh Sahani, and Mark M. Churchland. Cortical Control of Arm Movements: A Dynamical Systems Perspective. *Annual Review of Neuroscience*, 36(1):337– 359, 2013. eprint: https://doi.org/10.1146/annurev-neuro-062111-150509.

[42] Andres Agudelo-Toro, Jonathan A. Michaels, Wei-An Sheng, and Hansj¨org Scherberger. Accurate neuroprosthetic control through latent state transition training, June 2023. Pages: 2023.06.02.543242 Section: New Results.

[43] Jonathan C. Kao, Paul Nuyujukian, Stephen I. Ryu, Mark M. Churchland, John P. Cunningham, and Krishna V. Shenoy. Single-trial dynamics of motor cortex and their applications to brainmachine interfaces. *Nature Communications*, 6(1):7759, November 2015.

[44] Dmitry Kobak, Wieland Brendel, Christos Constantinidis, Claudia E Feierstein, Adam Kepecs, Zachary F Mainen, Xue-Lian Qi, Ranulfo Romo, Naoshige Uchida, Christian K Machens (2016) Demixed principal component analysis of neural population data eLife 5:e10989

[45] Santhanam G, Yu BM, Gilja V, Ryu SI, Afshar A, Sahani M, Shenoy KV. Factor-analysis methods for higher-performance neural prostheses. J Neurophysiol. 2009 Aug;102(2):1315-30. doi: 10.1152/jn.00097.2009. Epub 2009 Mar 18. PMID: 19297518; PMCID: PMC2724333.

Supplementary Figures

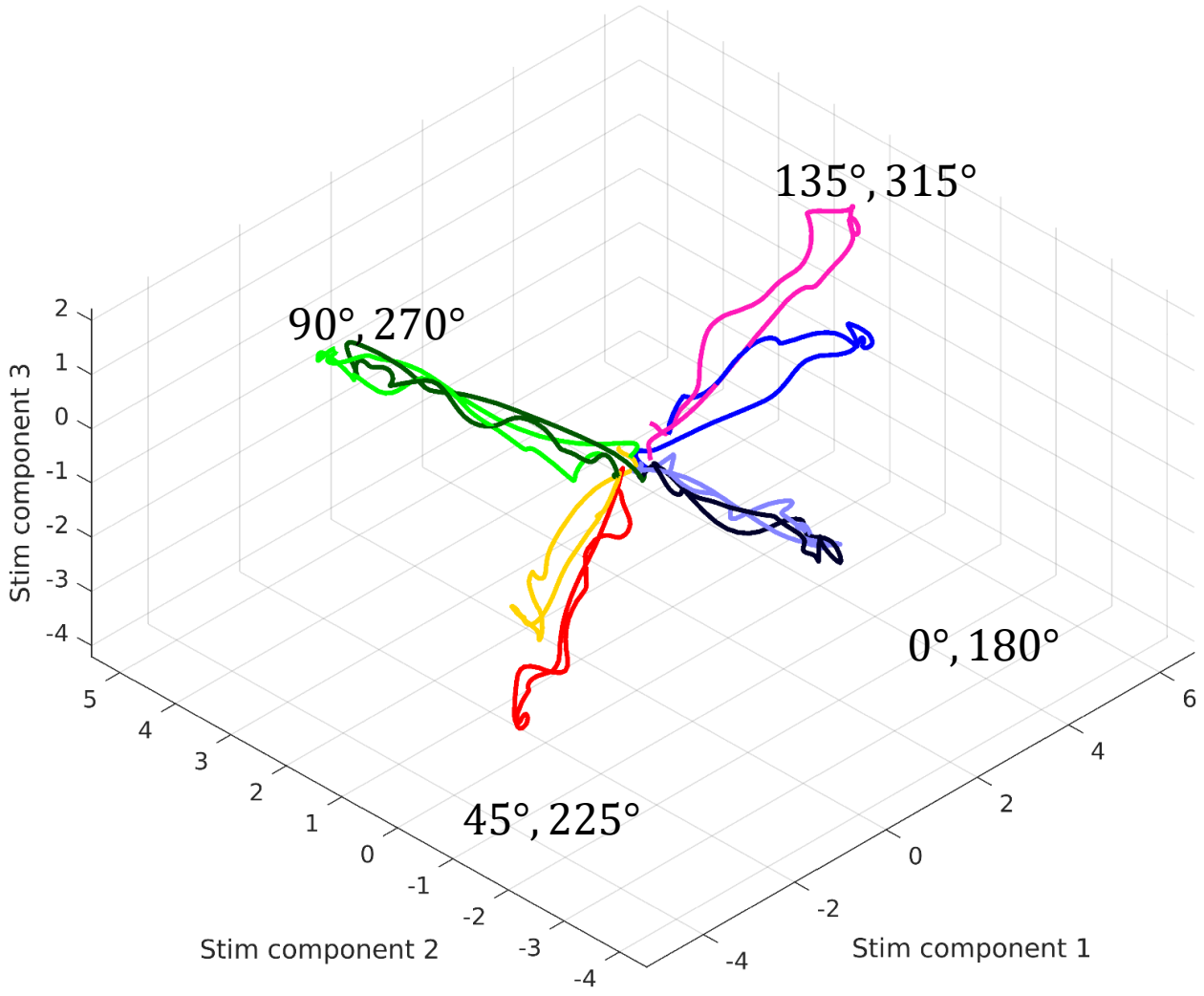

Figure 4.9 **3D plot of stimulus components of Calcium response.**

We used dPCA to extract three stimulus-dependant components from the average of each condition and plotted in a 3D space. This result emphasizes the great condition separability the Calcium response can provide.

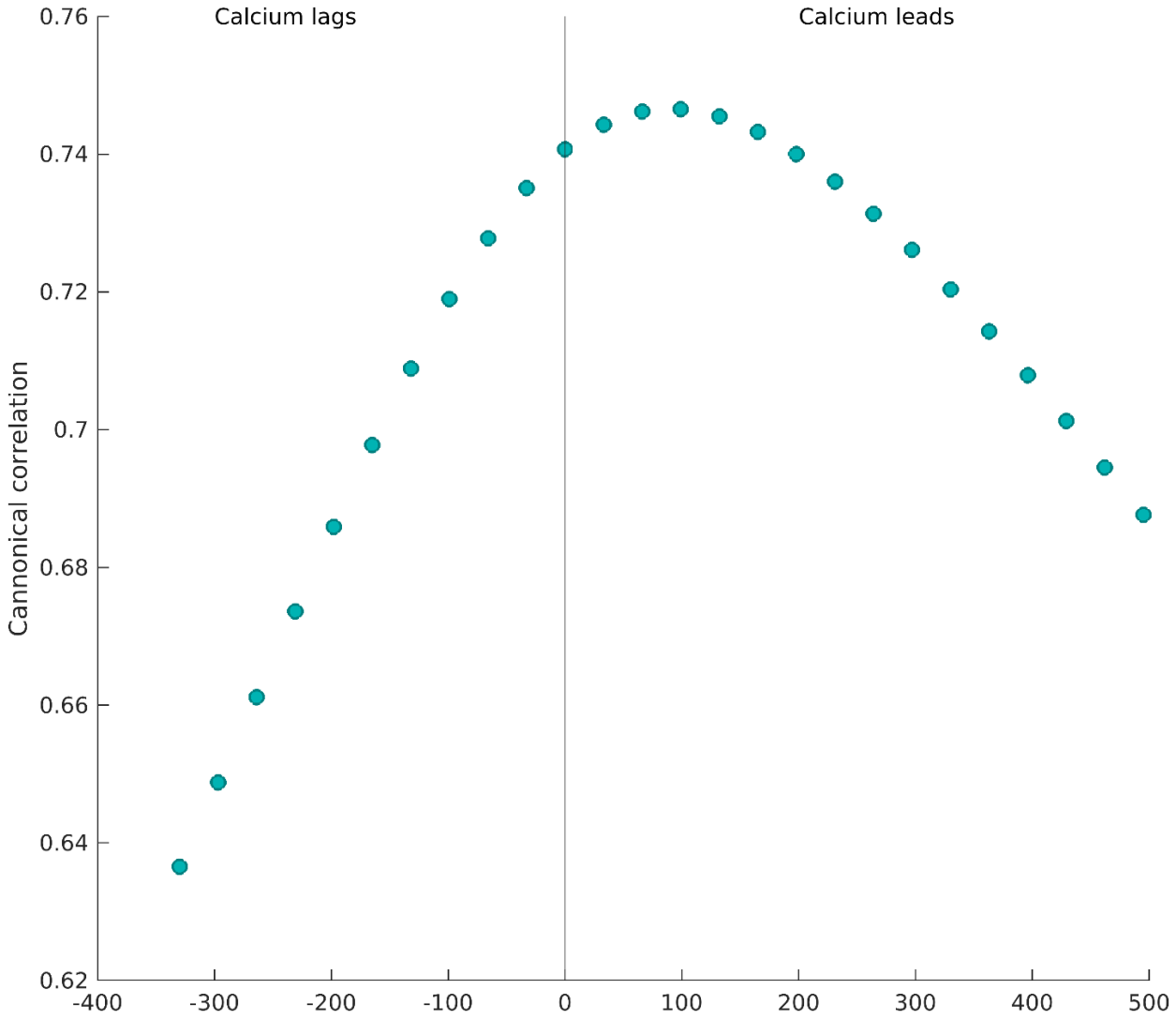

Figure 4.10 **Canonical correlation measure as a function of time difference between the two modalities.**

By measuring the correlation while sliding the time difference between the two modalities, we can, in a preliminary way, measure the delay between them due to the inherent nonlinearities.

Chapter 5

Conclusion

We hope that in this thesis we have sufficiently demonstrated some of the advantages of modeling the latent modes in the activity of neural population and how it can enhance our estimation of brain state in brain-machine interfaces. In chapter 2, we demonstrated that by preserving the latent variables that we modeled from input features in neural interfaces, we can compress those features while controlling the impact on application specific evaluation metrics. We applied this compression method to various datasets spanning different species and behavior and demonstrated its efficacy. In chapter 3, we investigated a multimodal study of surface electrophysiological recording and depth Calcium imaging and sought to study their correlation. We demonstrated that we could reconstruct single-cell activity of Calcium response at depth from spectral features of surface recording through decoding latent variables of Calcium signals. In chapter 4, we extended this study by trying to postulate a generalized framework to unify modalities in multimodal studies in one common subspace. By modeling the latent modes of each modality, we can combine their advantages to accurately estimate brain state. Additionally, we demonstrated that by aligning the sets of latent variables, we can reconstruct the original latent variables of each modality from the other. As more studies are emerging in which latent variables are used to drive online BCI [1,2,3], we postulate that those techniques and frameworks will be of high importance in the future.

Challenges

One Common challenge to inferring the latent modes is our lack of the knowing what the ground truth is. Given that these modes are unobservable, we can only estimate them through modeling them through observed brain states. That by itself leads to another problem which is our modeling choice of the observed neural activity and latent variables. Choosing the correct model for the neural activity is an important design choice as certain models can be an ill fit for certain data types. Lastly, latent variable modeling is most useful when the neural population activity is low-dimensional. Recent work shows that when the neural recording is very large in scale (>10,000 neurons), the representative latent variable is not low-dimensional anymore [4]. Lastly, some of the latent models are assumed to be autonomous and don't account for unmeasured inputs (i.e., input from different regions). These challenges are not meant to be blocks in the use of latent models but problems that can be addressed in order to strengthen their applications.

Future work

There are several directions that can be taken from the presented work in this thesis:

- One important direction that stims from the one of the challenges is the model choice. In the chapter of this thesis, most of the models we selected can be limited in their ability to model certain neural types [5] (e.g., GPFA with low firing spiking activity), but we selected those to work up and demonstrate the proof of concept we postulate in each chapter.
- In chapter 2, we presented a compression technique that can enhance the performance of neural interfaces. The next step would be a physical implantation of this algorithm to investigate the efficacy of this compression technique.

- In chapter 3 and 4, we demonstrated a multitude of concepts regarding the correlation between two modalities, surface ECoG recording and depth Calcium imaging, in one dataset. The next step is to test generalizability using another dataset with more complex behavior.

References

[1] Andres Agudelo-Toro, Jonathan A. Michaels, Wei-An Sheng, and Hansj¨org Scherberger. Accurate neuroprosthetic control through latent state transition training, June 2023. Pages: 2023.06.02.543242 Section: New Results.

[2] Jonathan C. Kao, Paul Nuyujukian, Stephen I. Ryu, Mark M. Churchland, John P. Cunningham, and Krishna V. Shenoy. Single-trial dynamics of motor cortex and their applications to brainmachine interfaces. *Nature Communications*, 6(1):7759, November 2015.

[3] Jonathan C. Kao, Stephen I. Ryu, and Krishna V. Shenoy. Leveraging neural dynamics to extend functional lifetime of brain-machine interfaces. Scientific Reports, 7(1):7395, August 2017. Number: 1 Publisher: Nature Publishing Group.

[4] Carsen Stringer, Marius Pachitariu, Nicholas Steinmetz, Matteo Carandini, and Kenneth D. Harris. High-dimensional geometry of population responses in visual cortex. Nature, 571(7765):361–365, July 2019. Number: 7765 Publisher: Nature Publishing Group.

[5] Cole Hurwitz, Nina Kudryashova, Arno Onken, and Matthias H Hennig. Building population models for large-scale neural recordings: Opportunities and pitfalls. Current opinion in neurobiology, 70:64–73, 2021.